Computational approaches to localized deformation within the lithosphere and for crust-mantle interactions

Thesis by

Eun-seo Choi

In Partial Fulfillment of the Requirements

for the Degree of

Doctor of Philosophy

California Institute of Technology

Pasadena, California

2009

(Defended August 19, 2008)

Acknowledgements

There are no proper words to convey my deep gratitude and respect for my thesis and research advisor, Professor Mike Gurnis. He has inspired me to become an independent researcher and helped me realize the power of critical reasoning. He also demonstrated what a brilliant and hard-working scientist can accomplish.

My sincere thanks must also go to the members of my thesis advisory and exam committee: Professors Jean-Philippe Avouac, Mark Simons, and Joann Stock, Jeroen Tromp, and Brian Wernicke. They generously gave their time to offer me valuable comments toward improving my work. In particular, Prof. Mark Simons showed me the great power and potential of applying the Interferometric SAR technique to geophysical problems. Also, Prof. Joann Stock provided me constructive criticism which helped me develop a broader perspective to my thesis.

I am most grateful to the collaborators for lending me their expertise and intuition to my scientific and technical problems: Dr. Luc Lavier; Dr. Pururav Thoutireddy and other computational scientists at Center for Advanced Computational Research at Caltech; Steve Quenette, Pat Sunter, Luke Hodkinson, Bill Applebe and other software engineers at Victorian Partnership for Advanced Computing in Australia.

There is no way to express how much it meant to me to have been a member of Seismological Laboratory. These brilliant friends and colleagues inspired me over the many years: Eh Tan, Lijun Liu, Chad Hall, Laetitia LePhouriet, Vlad Manea, Ravi Kanda, Yoshi Kaneko, Nathan Downey, Frederic Herman, Eric Hetland, Yaru Hsu, Laura Alisic, Lydia DiCaprio, Michelle Stempel, Dan Bower, and all the other current and former Seismolab grad students and visitors that I know.

The administrative staffs in the GPS division and Seismolab are memorable not

only for their prompt support but also for kind care: Marcia Hudson, Viola Carter, Sarah Gordon, Donna Mireles, and others. I have especially benefited from the truly professional support from the technical staffs: Ken Ou, Mike Black, David Kewley, and Naveed Ansari.

Special thanks must go to Professor Moonsup Cho at Seoul National University. Professor Cho taught me the delight of studying geology and encouraged me to pursue my interests in geodynamics. Also, it was a great delight to have been a member of the petrotectonics laboratory at Seoul National University. Memories of hard work I shared with the alumni helped me endure the frequent frustration. So, I thank Prof. Kyungwon Kyle Min, Dr. Seung-ryul Lee, Dr. Jungmin Kim, Dr. Keewook Li, Dr. Jinho Ahn, Hyejun Park, Dr. Yoonsup Kim, Jangha Kim.

I cannot forget friends who went through hard times together, cheered me on, and celebrated each accomplishment: Daegun Gavin Kim, Dr. Seokgoo Song and his family, and Dr. Kideok Kwon.

I would like to express my gratitude to my parents-in-law Kim Sungyong and Park Sunjoo for their unfailing emotional support. I also thank for heart-warming kindness from the family of my brother-in-law: Kyung-pil Kim, Suehee Lim, Aaram and Dara Kim.

I deeply thank my parents, Kwang-woo Choi and Sohye Park for their unconditional trust, timely encouragement, and endless patience. It was their love that raised me up again when I got weary. The family of my sister, Dr. Kyunghee Choi, Jinwoo Pyun, and my nephew Justin Pyun, have also been generous with their love and encouragement despite the long distance between us.

Finally, I thank with love to Bokyung and Junwon, my wife and son. Understanding me best as a Ph.D. herself, Bokyung has been my best friend and great companion, loved, supported, encouraged, entertained, and helped me get through this agonizing period in the most positive way.

Abstract

The thesis addresses selected problems related to localized deformation of the solid Earths lithosphere that stem from non-uniform strengths or emerge from non-linear rheologies. A new code has been developed to model the spontaneous localization through strain-weakening plasticity. A code coupling technique is introduced as an attempt to efficiently solve multi-material and multi-physics problems like crust-mantle interactions.

We first address a problem of localized deformation that is caused by pre-existing heterogeneities. Specifically, the effects of laterally varying viscous strength on the Cenozoic extension of the northern Basin and Range are investigated using numerical models. Three-dimensional viscous flow models with imposed plate motions and localized zones of low viscosity show that strain rates are concentrated in weak zones with adjacent blocks experiencing little deformation. This result can explain the geodetically discovered concentrated strain in the eastern part of the northern Basin and Range as the high strains are a response to far field plate motions within a locally less viscous mantle. The low viscosity of mantle is consistent with the low seismic velocities in the region.

As an instance of spontaneously emergent localized deformations, brittle deformations in oceanic lithosphere are investigated next. We developed a Lagrangian finite difference code, SNAC, to investigate this class of problems. Brittle deformations are modeled as localized plastic strain. The detailed algorithm of SNAC is presented in Appendix A.

The spacing of fracture zones in oceanic lithosphere is numerically explored. Numerical models represent a ridge-parallel cross-section of young oceanic lithosphere.

An elasto-visco-plastic rheology can induce brittle deformation or creep according to the local temperature. The spacing of localized plastic zones, corresponding to fracture zones, decreases as crustal thickness increases. The stronger creep strength raises the threshold value of crustal thickness: If the crust is thinner than the threshold, the brittle deformation can evolve into primary cracks. Plastic flow rules are parametrized by the dilation angle. If the dilatational deformation is allowed in the plastic flow rules (dilation angle$>0^\circ$), the primary cracks tend to be vertical; otherwise, a pair of primary cracks form a graben. The modeling results are compatible with the correlation between crustal thickness and the spacing of fracture zones found in different regions such as the Reykjanes ridge and the Australian Antarctic Discordance.

Three-dimensional (3D) numerical models are used to find the mechanics responsible for the various patterns made by the segments of the mid-ocean ridges and the structures connecting them. The models are initially loaded with thermal stresses due to the cooling of oceanic lithosphere and prescribed plate motions. The two driving forces are comparable in magnitude and the thermal stresses can exert ridge-parallel forces when selectively released by ridges and ridge-parallel structure. Represented by localized plastic strain, ridge segments interact in two different modes as they propagate towards each other: An overlapping mode where ridge segments overlap and bend toward each other and a connecting mode where two ridge segments are connected by a transform-like fault. As the ratio of thermal stress to spreading-induced stress (γ) increases, the patterns of localized plastic strain change from the overlapping to connecting mode. Rate effects are taken into account by the spreading rate normalized by a reference-cooling rate (Pe') and the ratio of thermal stress to the reference spreading-induced stresses (γ'). The stability fields of the two modes are unambiguously defined by Pe' paired with γ'.

Crust and mantle are distinct in terms of composition and rheology. To study the combined response of crust and mantle, it is necessary to solve multi-material and multi-physics problems that are numerically challenging. As an efficient way of solving such a problem, we introduce a code coupling technique. We adapt Pyre, a framework allowing distinct codes to exchange variables through shared interfaces, to

the coupling of SNAC, a Lagrangian code for lithospheric dynamics, and CitcomS, an Eulerian code for mantle convection. The continuity of velocities and tractions and no-slip conditions are imposed on the interfaces. The benchmarks against analytic solutions to the bending of a thin plate verifies that SNAC gives an accurate solution for the given traction boundary condition. It is also shown that Pyre can correctly handle the data exchanges at the interfaces. In a preliminary high-resolution model, an elasto-visco-plastic lithosphere is coupled to a Newtonian viscous mantle. This coupled model shows a steady growth of dome in the lithosphere directly above a hot sphere placed in the mantle. However, the two coupled codes incur unnecessarily high numerical costs because they use different methods for time integration.

Contents

Acknowledgements **iii**

Abstract **v**

List of Figures **xii**

List of Tables **xiv**

1 Introduction **1**

References 6

2 Deformation in transcurrent and extensional environments with widely spaced weak zones **7**

2.1 Abstract 7

2.2 Introduction 8

2.3 Model setup 10

2.4 Results 12

2.5 Discussion 16

References 18

3 Thermally induced brittle deformation in oceanic lithosphere and the spacing of fracture zones **20**

3.1 Abstract 20

3.2 Introduction 21

3.3 Numerical method 25

3.3.1 Constitutive model for brittle and plastic deformation 26
3.3.2 Thermo-mechanical coupling 27
3.4 Model setup 29
3.5 Results 32
3.5.1 Models with weak crust 32
3.5.2 Models with strong crust 36
3.5.3 Non-associated plasticity 38
3.6 Discussion 40
3.6.1 Effects of crustal thickness and creep strength 40
3.6.2 Implications of the sensitivity to crustal thickness and creep strength 42
3.6.3 Flexure of the segments 45
3.6.4 Implications for ridge axial processes 45
3.7 Conclusion 47
References 48

4 Thermomechanics of mid-ocean ridge segmentation 55
4.1 Abstract 55
4.2 Introduction 56
4.3 Numerical method 59
4.4 Model setup 60
4.4.1 Base model and its variations 62
4.5 Results 69
4.5.1 Variation of γ 70
4.5.2 Variation in rate of weakening 76
4.6 Discussion and conclusion 77
References 83

5 Coupling models of crustal deformation and mantle convection with a computational framework 88
5.1 Abstract 88

5.2 Introduction . . . 89
5.3 Numerical method . . . 91
5.3.1 SNAC: Overview . . . 91
5.3.2 StGermain framework . . . 92
5.4 Coupling through Pyre . . . 92
5.4.1 Overview of Pyre . . . 93
5.4.2 *Coupler* . . . 93
5.4.3 Coupling RegionalCitcomS and SNAC . . . 98
5.5 Benchmarks . . . 101
5.5.1 Traction boundary conditions applied on SNAC . . . 101
5.5.2 The RegionalCitcomS-to-SNAC transfer of traction . . . 101
5.6 Application . . . 103
5.6.1 Model Setup . . . 103
5.6.1.1 A qualitative 3-D test . . . 107
5.6.2 Results . . . 108
5.6.3 Discussion . . . 109
References . . . 113

A Algorithm of SNAC **117**
A.1 Governing equations . . . 117
A.2 Spatial discretization . . . 117
A.3 Nodal assemblage . . . 119
A.4 Damping and explicit time marching . . . 120
A.5 Mass scaling for numerical stability . . . 121
A.6 Constitutive update . . . 122
References . . . 124

B Verification of plastic solutions **125**
B.1 Oedometer test . . . 125
B.1.1 Problem Setup . . . 125
B.1.2 Analytic Solutions . . . 126

B.1.2.1 Elastic solution 126
B.1.2.2 Plastic solution 126
B.1.3 Results 129
B.2 Thick cylinder with a pressurized inner wall 129
B.2.1 Problem Setup 129
B.2.2 Analytic Solutions 131
B.2.2.1 Elastic solution 132
B.2.2.2 Plastic solution 133
B.2.3 Results 135
References 137

List of Figures

2.1 Shaded relief map of the northern Basin and Range 9
2.2 Model domain and initial and boundary conditions 13
2.3 Velocity profiles for transform and normal velocity boundary conditions 15

3.1 Gravity anomaly maps of the Reykjanes ridge and the Australian-Antarctic Discordance 23
3.2 Model geometry and boundary conditions 30
3.3 Evolution of topography, temperature, viscosity, and brittle deformation 34
3.4 The magnified upper left part of the model shown in Fig.3.3 35
3.5 Topography (in m) and accumulated plastic strain for the models with associated plasticity at 10 My 35
3.6 Same as Fig.3.3 37
3.7 Same as Fig.3.5, but for the models with zero dilation angle 39
3.8 Plots of the primary crack spacing 40
3.9 Same as Fig.3.5 43

4.1 Ridge segments and other ridge-parallel structures can release thermal stress in the ridge-normal direction 58
4.2 Geometry of the model domain 61
4.3 F_x as a function of time, depth profiles of temperature and viscosity, and 3-D rendering of the second invariant of plastic strain 64
4.4 A 3-D representation of the surface topography 65
4.5 Modes of interaction between two mutually approaching ridge segments 66
4.6 The piecewise linear variation of cohesion 69

4.7 Patterns of localized plastic strain 71
4.8 F_x as a function of amount of extension 72
4.9 Work done by the external extension versus γ 73
4.10 Plot of Pe' versus γ' 74
4.11 Models with a twice higher horizontal resolution 75
4.12 F_x for models with different weakening rate 76
4.13 Patterns of localized plastic strain in the increasing order of ω 77

5.1 The architecture of a coupled *Application* 94
5.2 Drawings showing the domains of the coupled solvers as a whole 96
5.3 An example of a 2-D mesh and a portion of the other mesh 97
5.4 Synchronizing time steps of two *Solvers* 99
5.5 Results from the thin-plate benchmark problems 102
5.6 The initial distribution of temperature and viscosity 106
5.7 Topography along the equator for various coupled models. 108
5.8 Results form the large coupled problem 110
5.9 Along-equator profiles of topography and the radial component of traction and velocity. 111

A.1 Configurations of tetrahedra and conventions for the notation 118

B.1 Schematic diagram depicting the oedometer test 126
B.2 Plots of stress vs. strain 130
B.3 Schematic diagram for the problem of the thick cylinder 131
B.4 The second invariant of stress from SNAC 136
B.5 Radial profiles of the second invariant of stress 137

List of Tables

2.1 Model parameters 11

3.1 List of numerical experiments 27
3.2 Rheological model parameters 28
3.3 Summary of average spacing of primary cracks at 10 My 40

4.1 Parameter values 63

5.1 List of parameters 104

Chapter 1

Introduction

The strength of lithosphere varies both in space and in time and the heterogeneities in strength reveal themselves at a variety of scales and in a variety of styles. For instance, the clear contrasts between continental and oceanic lithosphere and the presence of different types of plate boundaries render it far from reality to view the whole Earth's lithosphere as a uniform layer even on the largest scale. Prominent on smaller scales, intra-plate heterogeneities (often related to pre-existing geological structures) can be reactivated by external agents like thermal anomalies in the deeper mantle. Importantly, continued deformation under non-linear constitutive laws can create rheologically distinct structures in otherwise homogeneous lithosphere. These newly created structures in turn control the geological evolution of the affected region. In studies of lithospheric dynamics with an emphasis on such non-uniform strengths and non-linear rheologies, numerical simulations have demonstrated their unique capabilities: They can find models that are physically consistent with the observations, incorporate experimental data into the models, and even draw verifiable predictions from those models (e.g., Oganov and Ono, 2004; Kapp et al., 2008). The rapid increase in computing power has made the numerical approach to complex geodynamic problems even more tractable. Benefiting from modern numerical techniques and high performance computing, this thesis addresses some problems related to the consequences of non-uniform strengths and spontaneously emergent localization of deformation using numerical models. In addition to enhancing our understanding of geophysical processes, the thesis aims to return a contribution for

advancing computational techniques for lithospheric dynamics.

Chapter 2 addresses the effect of laterally varying viscous strength on the extension of the Basin and Range Province. The Cenozoic extension of this part of the western U.S. has been attributed to gravitational forces. Gravity tends to extend a thickened crust due to a period of earlier subduction and the region's extension is often attributed to it. We show that forces acting on plate boundaries are also sufficiently strong to drive the region's distributed extension. One of the particularly diagnostic observations is that GPS measurements in the northern Basin and Range Province indicate that the eastern part of the Province is, although farthest from the plate boundary, undergoing concentrated extension. Seismological observations suggest a locally weak mantle beneath this region. Results from numerical models involving such a heterogeneity are shown to be compatible with the geodetic observations.

The next two chapters shift focus to heterogeneities that develop spontaneously and in a highly localized fashion. Brittle deformations like faulting and localized ductile failure (shear bands) are among the examples. Fracture zones of oceanic lithosphere and mid-ocean ridges are addressed in detail. To model such geological structures numerically, it is required to introduce plasticity or equivalent non-linearities into constitutive models. For this purpose, we developed a code called SNAC. It is a 3-D finite difference code for modeling elasto-visco-plastic material. Details of the code's algorithm are presented in Appendix A.

Brittle deformation of oceanic lithosphere due to thermal stress is explored with a numerical model, with an emphasis on the spacing of fracture zones, in Chapter 3. Fracture zones are represented as localized plastic strain. The yield and plastic potential functions are defined such that material goes through brittle failure: i.e., the material loses coherence quickly after yielding occurs. The brittle failures are induced by stress due to thermal contraction, which is a direct result of the cooling of oceanic lithosphere. Using SNAC, we set up 2-D models representing ridge-parallel cross-sections that are initially placed near the spreading center. We investigate the sensitivity of the spacing of fracture zones to various parameters such as creep strength, crustal thickness, and the rule of plastic flow. Crustal thickness is crucial

in determining whether brittle deformation propagates through the whole crust and makes topographic features. There is a threshold in crustal thickness such that brittle deformation can make surface topography only when the crustal thickness is smaller than the threshold. The stronger creep strength is found to raise the threshold. The sensitivities found among the model parameters are compatible with the correlation between anomalously thick crust and the lack of fracture zones in the Reykjanes ridge. The enhanced fracturing found in the anomalously thin crust of the Australian-Antarctic Discordance is also consistent with the model results.

It should be noted that the observations indicate that fracture zones are formed at spreading centers with their spacing determined by the ridge segmentation. On the contrary, it takes about 4 Myr for primary cracks to appear in our weak crust models, which can be translated as meaning that fracture zones are initiated at 4 My-old lithosphere. This inconsistency between our models and observations might suggest that our models represent a different physics than the actual one behind the formation of fracture zones in oceanic lithosphere. On the other hand, the magnitude of thermal stresses is evidently large enough to fracture at least shallow portions of oceanic lithosphere. Thus, the discrepancy might be suggesting the existence of a new class of thermally-induced structures oriented in the ridge-normal direction, which have yet to be discovered. Interestingly, in the strong crust models, the primary cracks appear before 1 Myr, alleviating the temporal discrepancy significantly. However, the implication is still that fracture zones are initiated at some distance from the spreading center. Furthermore, the influences from the existing ridge segmentation are not included in any of our models. The fact that the models are set up in 2-D imposes another difficulty in extending our results to the actual mid-ocean ridge systems. In these 2-D models, it is not possible to observe what processes occur at the spreading center when off-axis lithosphere is being fractured by thermal stresses. A fully 3-D model would also be a prerequisite for investigating the effects of ridge segmentation on the formation of ridge-normal fractures.

We investigate in Chapter 4 a thermally strained system again, but strong kinematic driving forces are applied on top of the thermal stresses in this case. Brittle

deformation due to thermal stress is still the key phenomenon, but the mechanics responsible for the patterns made by mid-ocean ridges and transform faults is of our main interests. The geometry of the divergent plate boundaries is often described as orthogonally intersecting ridges and transform faults, which is definitely a simplified description. It has been observed that the geometry made by two mutually approaching ridge segments is correlated with spreading rates. It has also been suggested that orthogonality of transform faults and ridge segments requires forces acting in the ridge-parallel direction. There were several hypotheses about the origin of such ridge-parallel forces, but we consider thermal stresses as a plausible source. We set up 3-D numerical models for mutually approaching ridge segments with two types of loads: spreading and thermal stresses due to cooling. Unlike the two-layer models in the previous chapter, models in Chapter 4 represent a single layer of mantle. The lack of crust enables a direct observation of localized plastic deformations without potential complications due to weak lower crust as in Chapter 3. Patterns made by localized plastic strain, representing ridge segments and transform faults, are analyzed in terms of the relative strength of two driving forces. We note that thermal stress can exert ridge-parallel tension comparable to spreading-induced stress when selectively released by ridges and ridge-parallel structure. Two modes of ridge segment growth have been identified in plan view. An *overlapping* mode refers to the patterns of ridge segments that overlap and bend toward each other. Patterns are in a *connecting* mode when two ridge segments are connected by a transform-like fault. The ratio of thermal stress to spreading-induced stress is denoted as γ. As γ increases, the patterns change from the overlapping to connecting mode. The familiar orthogonal pattern falls between these two end members. The rate of stress accumulation is as important as the ratio between two types of loads. This rate-dependence is characterized by the spreading rate normalized by a reference-cooling rate (Pe') and the ratio of thermal stress to spreading-induced stresses (γ'). These two non-dimensional numbers unambiguously define stability fields of the two modes. The obliquely connecting, the orthogonally connecting, and the overlapping mode are similar to ridge-transform fault intersections observed in ultra-slow, slow to interme-

diate, and fast spreading centers, respectively. The patterns are also sensitive to the strain weakening rate.

Finally, Chapter 5 explores a technique for code coupling, one way of solving multi-material and multi-physics problems efficiently. The code coupling is managed by Pyre. Pyre is a collection of software enabling two distinct codes to interact by exchanging variables through shared interfaces. Motivated by computationally challenging problems like crust-mantle interaction, we coupled SNAC with Regional-Citcoms using this framework. We present the principles governing the physics for the coupled problems as well as technical issues. It is demonstrated that Pyre can handle the data exchange correctly by solving benchmark problems. Bending of a thin plate is solved both analytically and by SNAC. The transverse pressure loading on the plate is either uniform or sinusoidal. The case of the uniform pressure loading verifies that the stand-alone SNAC returns accurate solutions. The sinusoidal loading is transferred from CitcomS, in which a cosine perturbation is added to a steady-state temperature field. The perturbation drives convection in CitcomS and the cosine form is conserved in the resultant velocity and stress fields. SNAC receives the stress fields from CitcomS and convert them to traction boundary conditions. Then, the elastic response computed by SNAC is compared with an analytic solution to the cosine pressure loading. Preliminary results from a high-resolution coupled model are also presented. An elasto-visco-plastic lithosphere is coupled to a Newtonian viscous mantle. Flows in the mantle are driven by a hot spherical anomaly placed at the center of the CitcomS's domain. The coupled model shows a steady growth of a dome in the lithosphere above the hot blob, consistent with physical intuition. The unresolved issues are also discussed.

References

Kapp, P., Taylor, M., Stockli, D., Ding, L., 2008. Development of active low-angle normal fault systems during orogenic collapse: Insight from Tibet. Geology 26 (1), 7–10.

Oganov, A. R., Ono, S., Jul. 2004. Theoretical and experimental evidence for a post-perovskite phase of MgSiO3 in Earth's D″ layer. Nature 430 (6998), 445–448.

Chapter 2

Deformation in transcurrent and extensional environments with widely spaced weak zones[1]

2.1 Abstract

Previous mechanical models of the western U.S. have concluded that plate boundary forces cannot generate far-field deformation. Such models have ignored preexisting large-scale lithospheric strength variations, an assumption that appears to be inconsistent with seismically determined variations in lithospheric structure. We have formulated a three-dimensional viscous flow model with imposed plate motions, but include lateral zones of low viscosity. These models show that strain rates are concentrated in weak zones with adjacent blocks experiencing little deformation. Deformation can extend far inboard of plate boundaries, contrary to the result of previous studies with rheologically homogeneous plates, and apparently compatible with the variation in seismic velocity and GPS determined deformations in the western U.S. These results suggest that plate boundary forces cannot be neglected in the deformation of the western U.S., including the Cenozoic extension of the Basin and Range Province.

[1]Published by Eunseo Choi and Michael Gurnis in *Geophysical Researh Letter*, 2003, 30(2), 1076, doi: 10.1029/2002GL016129.

2.2 Introduction

Plate boundary and buoyancy forces could be significant in the extensional deformation of the western U.S., but since the deformation of this region is probably the result of a dynamic balance among multiple forces, attempts to determine which force dominates have been inconclusive. Since continental crust is pervasively faulted, England and Jackson (1989) and subsequent workers have assumed that at sufficiently large scales, the crust can be approximated as a non-linear viscous fluid. Making this assumption, with a single power law rheology approximating the vertically averaged lithosphere, Sonder et al. (1986) showed that boundary velocity decayed rapidly with distance away from the margin and that only a narrow region near either a transform or divergent boundary could be deformed. Sonder and Jones (1999) reached the conclusion that buoyancy forces dominate the western U.S. force balance by first showing that buoyancy forces are sufficiently large to cause the deformation and then by arguing that the influence of plate boundary forces is negligible within the continental interior. Using a thin viscous sheet model with velocity boundary conditions representing Pacific-North American transform motion, they rejected plate boundary forces as a viable mechanism for Basin and Range Province extension and concluded that plate boundary forces could not have generated the inferred strain rates throughout the western U.S.

However, these models ignored lateral heterogeneities in lithospheric strength. Since the mantle lid is the strongest part of the lithosphere, its thickness is closely related to the strength of the lithosphere. Seismic studies within the Basin and Range Province have shown marked differences in the thickness of the mantle lid (Fig.2.1) that should presumably be reflected in the strength of the lithosphere. For example, by compiling seismic refraction profiles, Braile et al. (1989) showed that there are lower seismic velocities within the upper mantle beneath the northern Basin and Range Province while seismic velocities under the Sierra Nevada and Colorado plateau are higher than average. York and Helmberger (1973) detected a band of low seismic velocities across the northern Basin and Range Province from the middle of

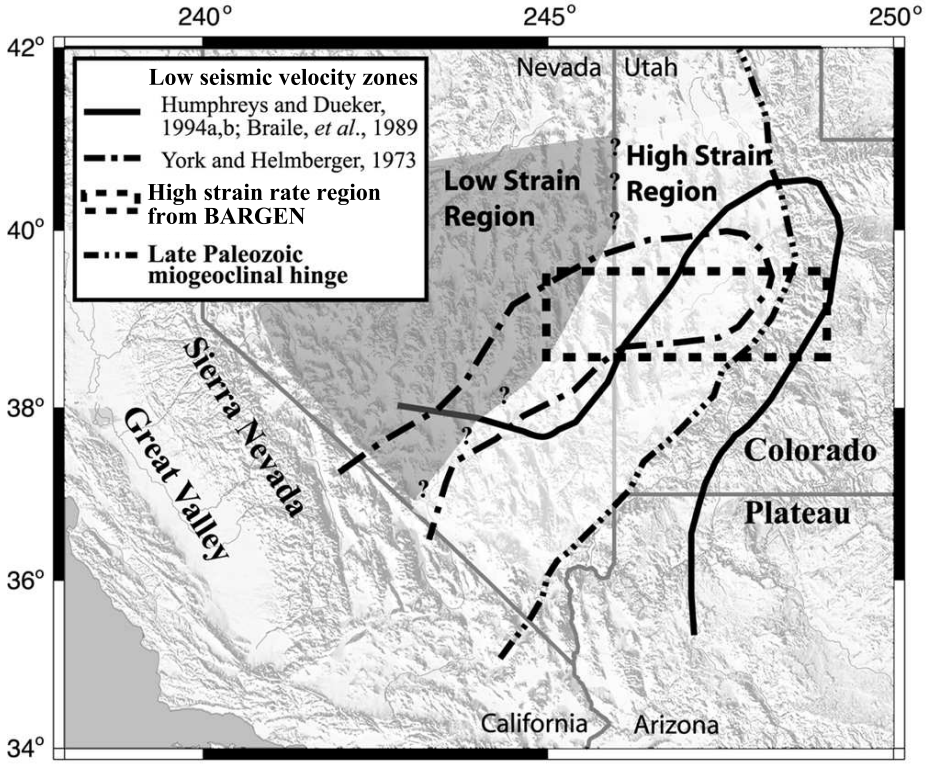

Figure 2.1: Shaded relief map of the northern Basin and Range Province, roughly showing the locations of low seismic velocity zones (York and Helmberger, 1973; Braile et al., 1989; Humphreys and Dueker, 1994b) and of the high strain rate region found with the BARGEN data (Niemi et al., 2004). It also shows a probable division of the northern Basin and Range Province into regions of relatively high strain rate (with brighter shades) and low strain rate (with darker shades).

Utah and traversing southern Nevada and southern California. This upper mantle structure is consistent in a more recent tomographic study by Humphreys and Dueker (1994a). This low velocity band may be more aptly described as a thin upper mantle lid beneath the Basin and Range-Colorado Plateau boundary, which was revealed by teleseismic P wave travel times (Zandt et al., 1995). Melbourne and Helmberger (2001) showed that lithospheric lid thickness varies significantly from 55 km along the coast of California to near zero thickness along eastern California.

We reappraise the argument against plate boundary forces and show that previous studies may not have adequately considered an important aspect of regional structure. New models presented here include lateral variations in viscosity to reflect the observed seismic velocity variations as a proxy for lithospheric strength. With the new formulation, we argue that plate boundary forces could generate substantial deformation within continental interiors in both strike-slip and extensional environments and that plate boundary forces should still be considered as a viable component in the force balance of the western U.S. during Cenozoic time.

2.3 Model setup

A three-dimensional (3D) spherical finite element method (Zhong et al., 2000) is used to model the influence of a discontinuous viscosity distribution on lithospheric deformation. Using the Boussinesq approximation, the equations of mass and momentum conservation are:

$$\nabla \cdot \boldsymbol{u} = 0 \tag{2.1}$$

$$-\nabla P + \eta \nabla^2 \boldsymbol{u} + \alpha \rho_0 g (T - T_0) \boldsymbol{e}_3 = 0, \tag{2.2}$$

where $\boldsymbol{e}_3$ is a unit vector in the radial direction; $\boldsymbol{u}$ is the velocity; T and T_0 are the temperature and the reference temperature, respectively; P is the pressure; η is the viscosity; α is the coefficient of thermal expansion; ρ_0 is the mantle density; and g is

Table 2.1: Model parameters

Symbol	Name	Value
α	Coefficient of thermal expansion	2×10^{-5} K^{-1}
ρ_0	Reference density	3300 kg/m^3
κ	Thermal diffusivity	10^{-6} m^2/s
η_0	Reference viscosity	10^{21} Pa·s
c_1	Constant for viscosity	9.50614
c_2	Constant for viscosity	1.02126
T_0	Reference mantle temperature	1300 °C
T_1	Surface temperature	0 °C

the acceleration of gravity. Viscosity is both temperature- and position-dependent:

$$\eta(T,\varphi,\boldsymbol{r}) = C(\varphi,\boldsymbol{r})\,\eta_0 \exp\left(\frac{c_1}{c_2+T/T_0} - \frac{c_1}{c_2+1.0}\right), \tag{2.3}$$

where η_0 is the viscosity when T=T_0 (viscosity within the asthenosphere); φ and $\boldsymbol{r}$ are the polar and the radial coordinates, respectively; c_1 and c_2 are constants chosen so that the viscosity at T=0 °C is higher than η_0 by two orders of magnitude. The role of $C(\varphi,\boldsymbol{r})$ is the spatially varying part of the viscosity. Model parameters are given in Table 2.1.

The spatial extent of the model domain is 60° in longitude, 40° in latitude, and 637 km in depth (Fig.2.2a). Only the inner region, 30° × 20° × 637 km, is of interest; the outer region used to reduce the influence of the vertical walls. Velocity boundary conditions enforce plate motion on the top within the inner region (within region A, Fig.2.2a). By creating a "transform boundary" along the equator with the length of the boundary being L, we can directly compare our result to earlier thin viscous sheet models with homogeneous rheologies through parameter conversion (Sonder et al., 1986). The temperature distribution is from a half-space cooling model defining a 100 km-thick thermal lithosphere (Fig.2.2b) and is horizontally uniform. The coefficient, $C(\varphi,\boldsymbol{r})$, is dependent on the polar angle, φ (0-180°), allowing weak zones through the lithosphere at different distances from the plate boundary (Fig.2.2c).

The weak zone in spherical shell models is defined as a narrow region of lower

viscosity compared to adjacent regions. The ratio of viscosity of the weak zone to that of the adjacent normal region at a certain depth is denoted as $\eta_{weak}/\eta_{normal}$. The zone of reduced viscosity extends to the base of the lithosphere, is 210 km in width, and is of the same length as the longitudinal dimension of the outer region ($\tilde{6}672$ km, Fig.2.2a). There are two controlling parameters for the weak zone: the viscosity ratio and its distance from the plate margin. $\eta_{weak}/\eta_{normal}$ varies from 10^{-1} to 10^{-4}. Three locations for the weak zone are considered as in the channel flow models: on the transform boundary (Fig.2.3a,b), far inboard of the margins (about $0.6L$), meant to represent the miogeoclinal hinge of the North American Plate (Fig.2.3c,d). Noting that a natural weak zone is developed at the plate boundary in thin viscous sheet models, we also consider models with two weak zones: one at the plate boundary and the other at $0.6L$ (Fig.2.3e,f).

2.4 Results

The results from the spherical shell models show a consistent dependence of deformation on viscosity reduction and weak zone position. We first consider the influence of the weak zones in spherical shell models in which plate motion along the boundary is strike-slip. We show the component (v) of velocity parallel to the strike-slip margin (see Fig.2.2a for a coordinate layout), normalized by the boundary velocity (v_0), versus normalized distance (x/L) from the plate boundary along the 30° meridian. The gradient of velocity is particularly steep within the weak zones while it is mild outside of the weak zones, especially for models with the weak zone on the boundary between the two plates. In other words, there are mildly deforming blocks separated by shear zones, a conclusion which is not particularly sensitive to the magnitude of the viscosity reduction once the velocity has been reduced by one order of magnitude (Fig.2.3a,c).

There has also been a normal component to the motion of the Pacific plate outboard of the northern Basin and Range Province (e.g., Atwater and Stock, 1998) and so a second boundary condition is considered, which can also be compared with earlier

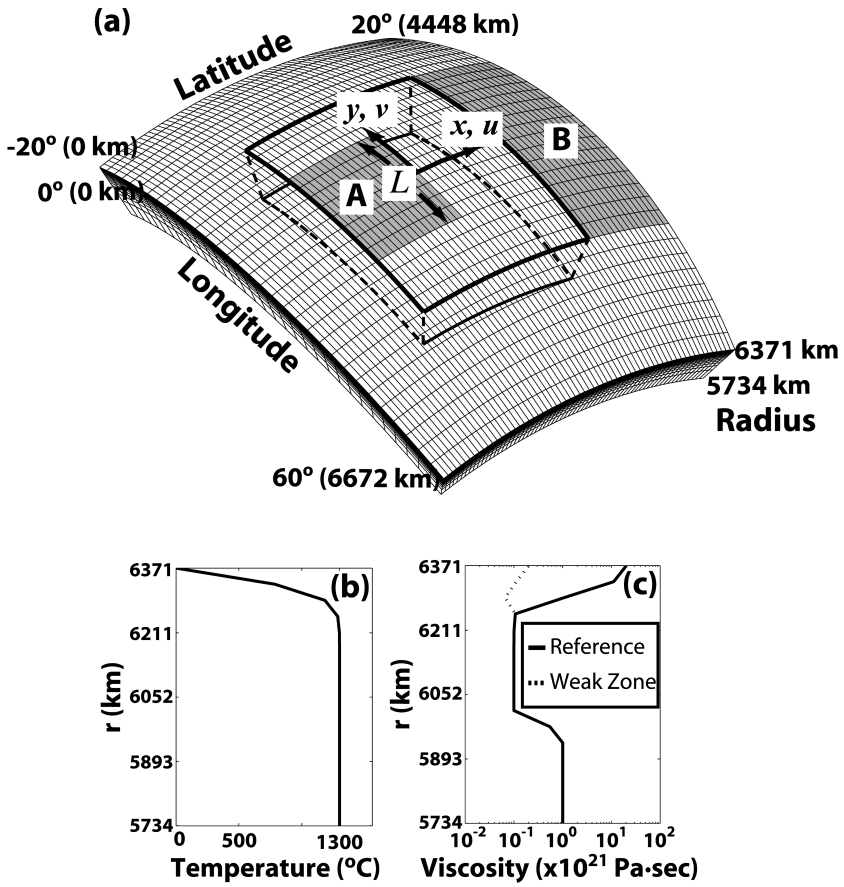

Figure 2.2: (a) Coordinates of the finite element mesh and configuration for boundary conditions. The inner region is the volume outlined by thick solid and dashed lines. x-axis is along the 30° meridian and y-axis along the equator. u and v are velocity tangential to x- and y-axis, respectively. Velocity boundary conditions are applied on the surface in the regions shaded with dark gray: u=0.0, v=v_0=5.0 cm/yr in region A, while $u = v = 0$ in region B. v=0.0 and $\partial u/\partial x$=0.0 on the vertical boundaries. The mesh has 32 elements in longitude and 64 in latitude (with regular spacing) and 16 in depth (with higher spatial resolution through the upper 100 km) (b) Variations of temperature with depth. Temperature is horizontally uniform. (c) Viscosity variation with depth. Viscosity for the blocks is drawn in a solid line. Viscosity for a weak zone with viscosity ratio η_{weak}/η_{block} of 10^{-2} is drawn in a dashed line.

models (Figure 3b,d). With purely normal velocity boundary conditions ($\boldsymbol{u}_0 = -5$ cm/yr and $v = 0.0$) applied on the region A (Fig.2.2a), the normal component of velocities for each configuration of weak zone shows a similar pattern compared with the transform boundary condition: strain rate concentration in a weak zone between mildly deforming blocks.

It is noteworthy that the behavior of these numerical models is in sharp contrast to the analytical solutions for a semi-infinite, thin viscous sheet model for a lithosphere with a non-linear rheology. For example, in the weak-zone model with the weak zone placed far inboard of the margin (at x/L=$\sim$0.6 Fig.2.3c), the velocity decreases to 50 % of the boundary value at x/L=$\sim$0.3, while in the thin sheet model with n $>$ 1 the corresponding velocity is essentially zero. The characteristic length scale of velocity decay is thus larger in these numerical models then in the thin viscous sheet models. It is even larger for the normal velocity boundary condition. The decrease of velocity is only about 10 % at x/L =$\sim$0.3 for the model with the weak zone far inboard of the boundary (Fig.2.3d). In thin viscous sheet models, as the non-linearity of the viscosity increases (i.e. as the exponent, n, increases), the characteristic length scale of the decay of velocity decreases (England et al., 1985; Sonder et al., 1986). However, lowering the viscosity within the weak zone leads to an increase in characteristic length scale over which the deformation is distributed.

Models with two weak zones (Fig.2.3e,f) show the importance of incorporating pre-existing strength variations in the lithosphere even though a non-Newtonian rheology may result in a weak plate boundary. A weak plate boundary zone, simulating the effect of a power-law rheology, does take up a large amount of deformation, but the interior weak zone still deforms faster than the strong interior region. This deformation pattern becomes obvious in models with a relatively strong strike-slip boundary (Fig.2.3e), or with imposed normal velocity boundary conditions (Fig.2.3f). Thus, our results are relevant to the deformation of the western U.S., because this region has a significant component of extension.

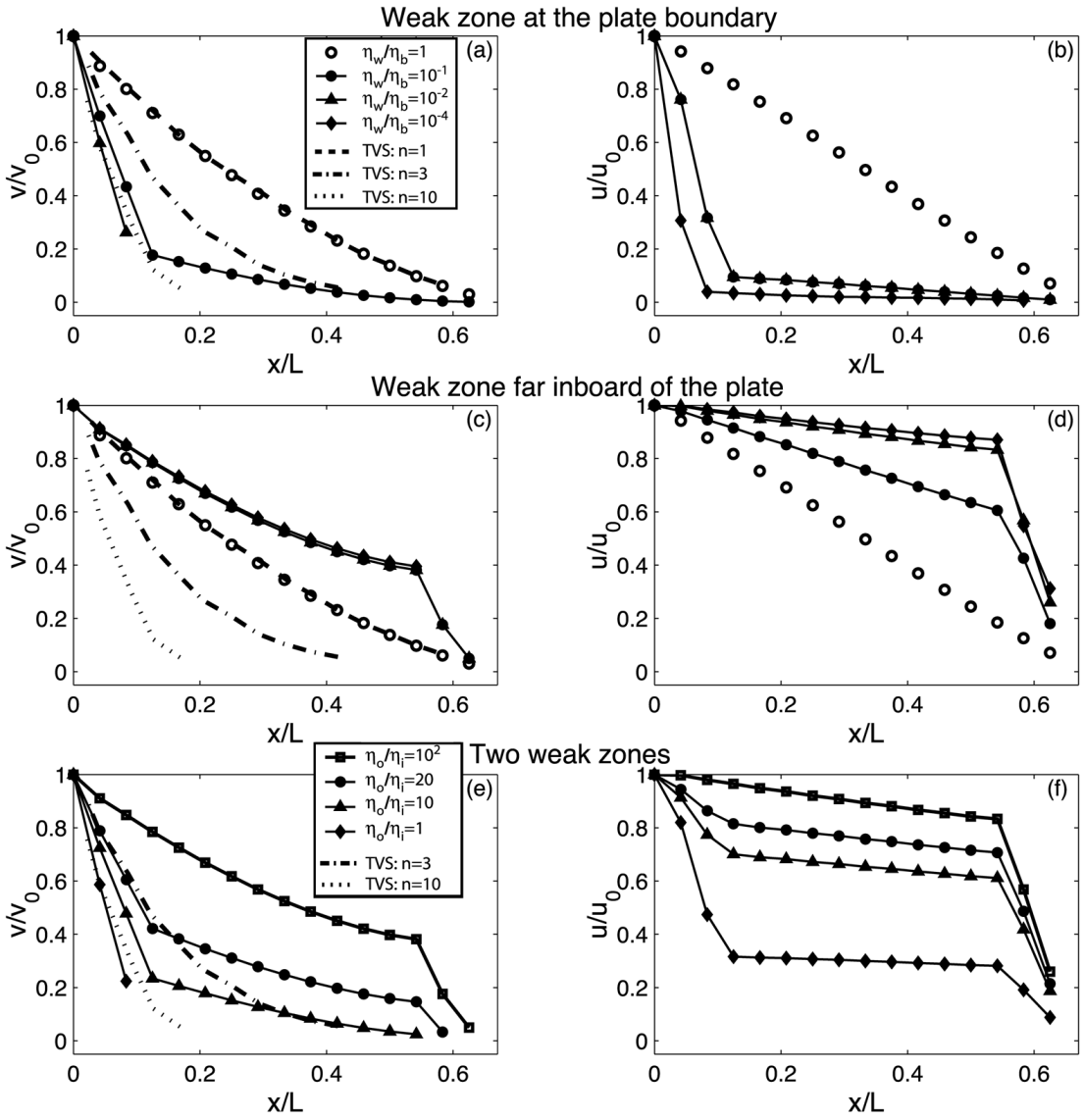

Figure 2.3: Velocity profiles for transform boundary conditions and for normal velocity boundary conditions. (left) y-velocity, v, plotted as a function of distance from the transform boundary, x. v is normalized with respect to v_0=5 cm/yr, the boundary velocity, and x with respect to L. (right) Normalized x velocity, u/u_0, versus normalized distance from the plate boundary, x/L, for the normal velocity boundary conditions: $u = u_0$=-5 cm/yr and v=0.0. Different symbols are used for numerical solutions with different viscosity ratio of the weak zone to the normal value (η_w/η_b). For comparison, analytical solutions for thin viscous sheet model (TVS) with the corresponding velocity boundary condition (England et al., 1985) are plotted with different types of lines. (a,b) The weak zone is on the boundary between the two plates, (c,d) at x/L =$\sim$0.6, far inboard of the plate. (e,f) Models with two weak zones: the outer one at the plate boundary and the interior one at x/a =$\sim$0.6, of which viscosities are η_o and η_i, respectively. While η_i/η_b fixed at 10^{-2}, η_o/η_i changed from 1 to 10^2.

2.5 Discussion

In order to verify the importance of either plate boundary forces or buoyancy forces, heterogeneities in the lithospheric strength need to be properly incorporated into deformation models. Variations in lithospheric strength are generally critical for understanding the dynamics of lithospheric deformation, but studies such as Neil and Houseman (1997) and Ellis et al. (1998) have only applied such complications to compressional settings. As for the Basin and Range Province, Sonder and Jones (1999) treated the Sierra-Nevada and Great Valley block as a relatively rigid area in a thin-sheet model, showed that deformation remained concentrated near the transform boundary, and argued that the inclusion of strong regions did not alter the decay of the plate boundary forces into continental interiors. However, their specific lithospheric strength structures did not incorporated all of the crustal and upper mantle features suggested by seismic studies.

The eastern part of the northern Basin and Range Province appears to be different in terms of its seismically determined crust and upper mantle compared to adjacent regions. The eastern Basin and Range Province (at 39°-40° N) with a width of 300-km and located west of the Colorado Plateau coincides with the northern end of a low velocity zone (York and Helmberger, 1973; Humphreys and Dueker, 1994b) (Fig.2.1). The association of this seismic low velocity region with high heat flow ($\sim$120 mW/m^2) and recent active volcanism (along the St. George volcanic trend) led Humphreys and Dueker (1994a) to suggest the existence of partial melts in the upper mantle. They thought about 1-3 % of partial melt would be necessary to explain the $\sim$4 % of P wave velocity reduction. Since partial melts generally reduce viscosity, the heat flow and seismic studies support the presence of a weak zone beneath the eastern part of the northern Basin and Range Province. This putative weak zone is geometrically similar to our models with the weak zone far inboard of plate boundary. Consequently, based on our models (Fig.2.3) we would expect that this region to be straining much faster compared to the Basin and Range Province further to the west or the Colorado Plateau further to the east.

This interpretation is consistent with recent geodetically determined strain rate distributions. With the Basin and Range Geodetic Network (BARGEN) (Wernicke et al., 2000), Niemi et al. (2004) found a faster velocities in the eastern one-third of the northern Basin and Range and negligible velocities in the western part of the northern Basin and Range Province (except near to the plate boundary) (Fig.2.1). Specifically, they found that rates varied linearly with distance from the western boundary of the Colorado Plateau along 39°N in the area that had previously been mapped as a seismically low velocity region. These GPS data show that the central part of the northern Basin and Range Province behaves as a relatively rigid block, while strain rate is distributed mostly over the possibly weaker eastern part.

These results imply that plate boundary forces could be important even in the far-field deformation of a continent, when large-scale lateral variations in lithospheric strength are present within a continent. Since the rapid exponential decay of deformation away from the boundary has been used as an argument against plate boundary forces in continental deformations, we need to further investigate the combined influence of plate boundary forces and heterogeneous rheology.

References

Atwater, T., Stock, J., 1998. Pacific-North America plate tectonics of the Neogene southwestern United States: An update. International Geology Review 40, 375–402.

Braile, L. W., Hinze, W. J., von Frese, R. R. B., Keller, G. R., 1989. Seismic properties of the crust and uppermost mantle of the conterminous United States and adjacent Canada. In: Pakiser, L. C., Mooney, W. D. (Eds.), Geophysical framework of the continental United States. Vol. 172 of Geol. Soc. Am. Mem. Geological Society of America, Boulder, Colo., pp. 655–680.

Ellis, S., Beaumont, C., Jamieson, R. A., Quinian, G., 1998. Continental collision including a weak zone: The vise model and its application to the Newfoundland Appalachians. Can. J. Earth Sci. 35, 1323–1346.

England, P., Houseman, G., Sonder, L., 1985. Length scales for continental deformation in convergent, divergent, and strike-slip environments: Analytical and approximate solutions for a thin viscous sheet model. J. Geophys. Res. 90, 3551–3557.

England, P., Jackson, J., 1989. Active deformation of the continents. Ann. Rev. Earth Planet. Sci. 17, 197–226.

Humphreys, E. D., Dueker, K. G., 1994a. Physical state of the western U.S. upper mantle. J. Geophys. Res. 99, 9635–9650.

Humphreys, E. D., Dueker, K. G., 1994b. Western U.S. upper mantle structure. J. Geophys. Res. 99, 9615–9634.

Melbourne, T., Helmberger, D., 2001. Mantle control of plate boundary deformation. Geophys. Res. Lett. 28, 4003–4006.

Neil, E. A., Houseman, G. A., 1997. Geodynamics of the Tarim Basin and the Tian Shan in central Asia. Tectonics 16, 571–583.

Niemi, N. A., Wernicke, B. P., Friedrich, A. M., Simons, M., Bennett, R. A., Davis, J. L., 2004. BARGEN continuous GPS data across the eastern Basin and Range province, and implications for fault system dynamics. Geophys. J. Int. 159 (3), 842–862.

Sonder, L. J., England, P. C., Houseman, G. A., 1986. Continuum calculations of continental deformation in transcurrent environment. J. Geophys. Res. 91, 4797–4810.

Sonder, L. J., Jones, C. H., 1999. Western United States extension; how the west was widened. Annu. Rev. Earth Planet. Sci. 27, 417–462.

Wernicke, B., Fredrich, A. M., Niemi, N. A., Bennett, R. A., Davis, J. L., 2000. Dynamics of plate boundary fault systems from Basin and Range Geodetic Network (BARGEN) and geologic data. GSA Today 10, 1–7.

York, J. E., Helmberger, D. V., 1973. Low-velocity zone variations in the southwestern United States. J. Geophys. Res. 78, 1883–1886.

Zandt, G., Myers, S. C., Wallace, T. C., 1995. Crust and mantle structure across the Basin and Range-Colorado plateau boundary at 37° latitude and implications for Cenozoic extensional mechanism. J. Geophys. Res. 100 (B6), 10,529–10,548.

Zhong, S., Zuber, M. T., Moresi, L., Gurnis, M., 2000. The role of temperature-dependent viscosity and surface plates in spherical shell models of mantle convection. J. Geophys. Res. 105 (B5), 11,063–11,082.

Chapter 3

Thermally induced brittle deformation in oceanic lithosphere and the spacing of fracture zones[1]

3.1 Abstract

Brittle deformation of oceanic lithosphere due to thermal stress is explored with a numerical model, with an emphasis on the spacing of fracture zones. Brittle deformation is represented by localized plastic strain within a material having an elasto-visco-plastic rheology with strain softening. We show that crustal thickness, creep strength, and the rule governing plastic flow control the formation of cracks. The spacing of primary cracks decreases with crustal thickness as long as it is smaller than a threshold value. Creep strength shifts the threshold such that crust with high creep strength develops primary cracks regardless of crustal thicknesses, while only a thin crust can have primary cracks if its creep strength is low. For a thin crust, the spacing of primary cracks is inversely proportional to the creep strength, suggesting that creep strength might independently contribute to the degree of brittle deformation. Through finite versus zero dilatation in plastic strain, associated and non-associated flow rule results in nearly vertical and V-shaped cracks, respectively. Changes in the tectonic environment of a ridge system can be reflected in variation in crustal thickness, and thus related to brittle deformation. The fracture zone-free

[1]Published by Eun-seo Choi, Luc Lavier and Michael Gurnis in *Earth and Planetary Science Letters*, 2008, 269(1-2), pp. 259-270, doi: 10.1016/j.epsl.2008.02.025269.

Reykjanes ridge is known to have a uniformly thick crust. The Australian-Antarctic Discordance has multiple fracture zones and thin crust. These syntheses are consistent with enhanced brittle deformation of oceanic lithosphere when the crust is thin and vice versa.

3.2 Introduction

The length of the mid-ocean ridge segments varies substantially among spreading centers and is correlated with several tectonic factors, including a positive correlation with spreading rate. The first order segments, bounded by transform faults (first order discontinuities), have an average length of 600±300 km along fast (>6 cm/yr) spreading ridges and 400±200 km for slow (<6 cm/yr) spreading ridges (Macdonald et al., 1991). Sandwell (1986) suggested that the length of the first order segments varies linearly with spreading rates. Although valid at the first order scale, such linear correlations are not supported at every level of the hierarchy. For example, the magmatic segments of slow to intermediate spreading ridges were shown to be 52.5 km long on average, independent of spreading rates (Brais and Rabinowicz, 2002).

Segment lengths are also apparently associated with regional variations in crustal thickness, creep strength, and mantle temperature. For instance, the Reykjanes ridge above the Iceland hot spot is known to have a uniform and much thicker crust for its spreading rate (Bunch and Kennett, 1980; Murton and Parson, 1993; Smallwood and White, 1998). This hot spot-affected ridge has been shown to exhibit signatures of wet mantle source for basaltic melt (Nichols et al., 2002). The water in crustal and mantle minerals has a strong weakening effect on creep strength although the preferential partitioning of water into melt phases complicates this straightforward relation (e.g., Karato, 1986; Hirth and Kohlstedt, 1996). In contrast, the Australian-Antarctic Discordance (AAD) has a highly rugged seafloor indicating increased fracturing (Hayes and Conolly, 1972; Weissel and Hayes, 1974) as well as anomalously thinner crust in comparison with other parts of the Southeast Indian Ridge (SEIR) (Tolstoy et al., 1995; Okino et al., 2004). Such regional features were attributed to colder mantle

beneath the AAD (Weissel and Hayes, 1974), a hypothesis that was later supported by the systematics of major elements of basalt along the SEIR (Klein et al., 1991). These two regions, the Reykjanes ridge and the AAD, respectively exhibit reduced and enhanced segmentations at both the 1st and 2nd order compared with the other parts of the respective ridge systems. The degree of fracturing in those regions is substantially different in the profiles of free-air gravity anomaly (Fig.3.1). The profile for the Reykjanes ridge (A-A′) is smooth over the segment closer to Iceland and becomes rugged towards the southern end. The profile B-B′ along the SEIR shows strong high frequency changes in depth and free-air gravity associated with the fracture zones over the AAD and with an abrupt transition to a smooth segment east of the AAD.

A magma supply model has been proposed to explain the fundamentally different characteristics between slow- and fast-spreading centers, as well as axial morphology of a single ridge segment. According to this model, the variable amount of available magma at spreading centers and its along-ridge transport are responsible for along-ridge variations in axial bathymetry and associated geophysical and geochemical observations (Macdonald et al., 1991; Macdonald, 1998). Relating mantle dynamics to the conceptual magma supply model, calculations of mantle flow beneath slow spreading centers exhibit 3-D patterns that are segmented along the axis (Parmentier and Phipps Morgan, 1990; Lin and Phipps Morgan, 1992; Barnouin-Jha et al., 1997; Magde and Sparks, 1997). A problem with such flow models is that the wavelengths of the segmented mantle upwelling are larger (150 km) than the observed average second order segment length (∼50 km) (Barnouin-Jha et al., 1997). However, when the effect of melt extraction on the viscosity of the magma residue was taken into account, a much shorter wavelength of segmented flow (as short as 70 km) was achieved (Choblet and Parmentier, 2001). Related to the magma supply model, ridge migration with respect to a hot spot reference frame was suggested to cause asymmetric mantle upwelling and melt production (Carbotte et al., 2004). This model provides an explanation for the observation that the majority of “leading” segments (that is, those that step in the same direction as ridge migration direction) are magmatically more robust.

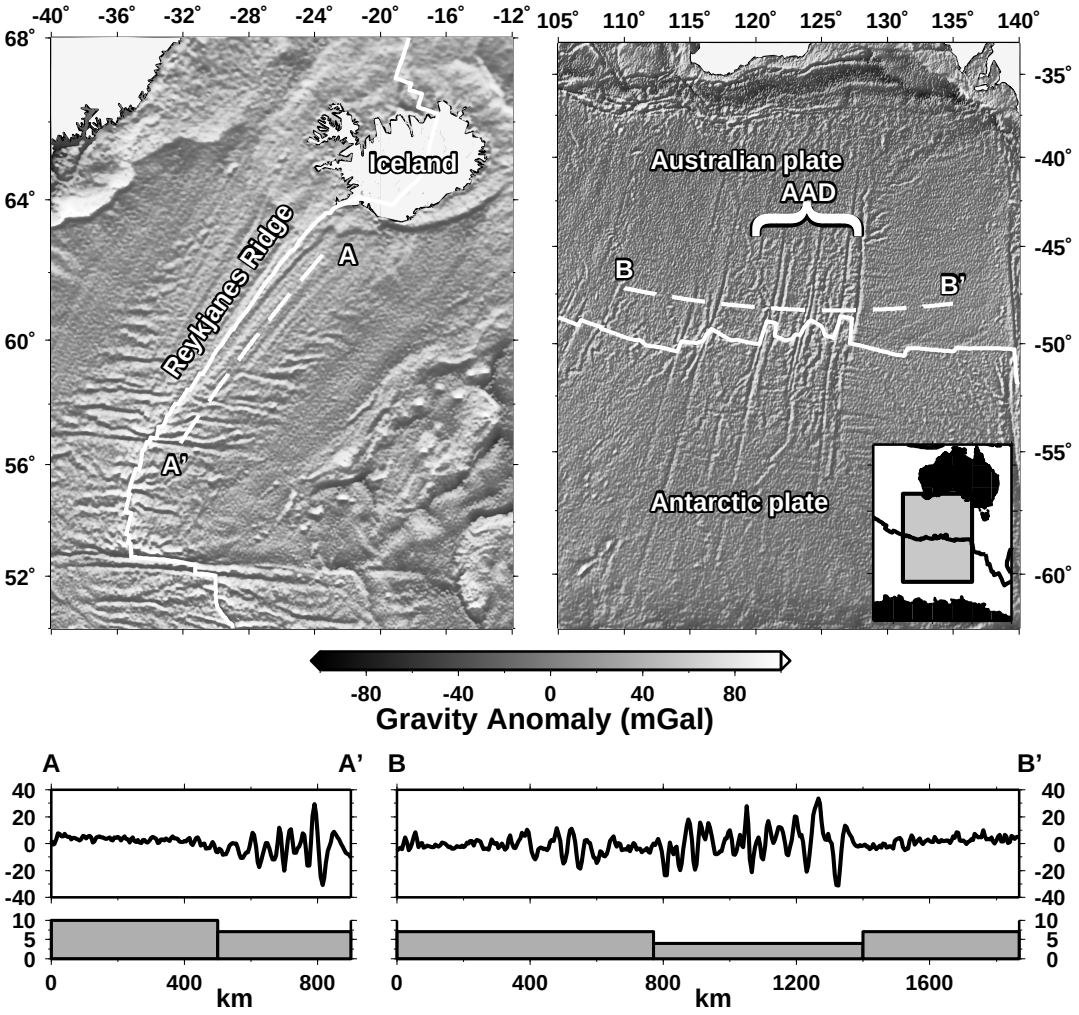

Figure 3.1: Gravity anomaly maps derived from satellite altimetry of the Reykjanes ridge and the Australian-Antarctic Discordance (Sandwell and Smith, 1997). Thick white lines track the plate boundary (Bird, 2003). Each map is illuminated from the azimuths of 0° and 300°, respectively, so that the ridge-normal structures look prominent. Free-air gravity (in mGal) with mean removed (bottom panels) show the profiles (A-A′ and B-B′) with simplified variation of crustal thickness in km (lower plots). See text for crustal thickness references.

Although the magma supply model is consistent with a range of observations, the model has yet to be linked with the brittle manifestation of mid-ocean ridge segmentation. Thermal stress due to the cooling of oceanic lithosphere is one possible driving force responsible for brittle ridge segmentation among many others (cf. Kastens, 1987). Using an order of magnitude argument, Collette (1974) suggested that thermal stress associated with the cooling of oceanic lithosphere should exceed its strength. By computing the bending moment of a semi-infinite thin elastic plate experiencing top-down cooling, it was suggested that segment length should be determined such that a plate can release thermal stress by bending (Turcotte, 1974). Expanding on this theory, Sandwell (1986) showed that ridge-bounding first order discontinuities can release thermal stress effectively when their spacing is proportional to spreading rate. Decomposing thermal stress into contraction and bending components, Haxby and Parmentier (1988) speculated that thermal bending stress, not contraction, would govern the spacing of transform faults because the magnitude of thermal contraction stress was independent of the ridge segment length. These studies, however, provide only an upper bound or indirect estimate of the fracture zone spacing. Sandwell and Fialko (2004) focused on the optimal spacing between thermal cracks, which minimizes stored elastic energy in a bending plate. It is notable that the spacing is not given a priori but is determined by the principle of minimum elastic energy.

A theory of thermal cracks provides useful insight into the spacing of ridge discontinuities if we assume that ridge segmentation occurs due to thermal stress. The stress distribution as a function of distance from a two-dimensional crack has been analyzed by Lachenbruch (1962). In a thermally contracting elastic half space, stresses are assumed to be released on the wall of a vertical crack. At greater distances from the wall, stress will increase to an ambient level so that each crack has a finite zone of stress relief. Since the strength of the material is limited, another crack will form at a distance where the stress exceeds the strength. In this fashion, the spacing between cracks is related to material strength and the size of the stress relief zones, which is determined by the material's elastic properties. Although this model could successfully

explain crack spacing in permafrost, it leads to an apparent paradox for mid-ocean ridge segmentation. The model predicts a shorter spacing of cracks when the ambient level of stress is higher or the depth extent of cracks is shallower (Lachenbruch, 1962). Consequently, for fast and hot spreading centers, the Lachenbruch model implies a smaller fracture zone spacing because the amount of thermal stress is larger and brittle layers thinner compared to slow cooler spreading centers. In fact, the opposite trend is observed.

In this study, we investigate the role of thermal stress on the formation of mid-ocean ridge segmentation in terms of brittle deformation in young oceanic lithosphere. We address the influence of crustal thickness and rheology, factors that reflect a ridge system's tectonic setting, on fracture zone formation. A numerical method is used in which brittle deformation is allowed within the framework of continuum mechanics. This is an exploratory attempt towards a better understanding of ridge segmentation processes: relatively simple numerical models are used to draw implications relevant to actual ridge systems.

3.3 Numerical method

We use SNAC, an explicit finite difference code, to solve for the equations of momentum and heat energy conservation [see Appendix A]. Although the code is fully three-dimensional, because of computational requirements, we only solve for 2-D problems here. The conservation equations are solved by the energy-based finite difference method (Bathe, 1996), which makes SNAC equivalent to a finite element code with linear tetrahedral elements except for the lack of explicit references to shape functions. The well-known over-stiffness of linear tetrahedral elements in the incompressible limit is overcome using a mixed discretization technique (Marti and Cundall, 1982; de Souza Neto et al., 2005). The solution scheme is identical to that used in FLAC (Fast Lagrangian Analysis of Continua) (Cundall, 1989; Poliakov et al., 1993, 1994, 1996), where a dynamic problem is damped to achieve an equilibrium solution. An explicit forward Euler method is used for the solution integration and time-dependent

constitutive update. SNAC benefits from modern software engineering through StGermain, an infrastructure framework for developing modeling software (Quenette et al., 2005).

3.3.1 Constitutive model for brittle and plastic deformation

Strain-weakening plasticity is coupled with viscoelasticity in our elasto-visco-plastic (EVP) model. An additive decomposition of total strain is assumed such that the total strain is the sum of elastic, viscous, and plastic strain (e.g., Albert et al., 2000). The stress update algorithm is very close to a standard rate-independent plasticity (Simo and Hughes, 2004), but the elastic trial stress is replaced with the Maxwell viscoelastic trial stress. This constitutive model enables the failure mechanism, either brittle failure or viscous creep, to be selected uniquely and naturally. For example, an extremely high viscosity at low temperature would allow only a negligible amount of creep, so that material will undergo brittle failure when stressed beyond its strength. On the other hand, elastic stress would be substantially relaxed by creep if viscosity is lowered at high temperature, prohibiting brittle failure. One simplification is the use of effective viscosities derived from power laws for dislocation creep. Instead of using power laws directly for constitutive updates, the derived effective viscosities are inserted into the Maxwell viscoelastic constitutive law. We assume that stress increments at each time step are sufficiently small so that there is no need to iterate the constitutive update step when dealing with the nonlinearity of power law creeps. The term "plastic flow" often means distributed flow by creep (Rutter, 1986; Kohlstedt et al., 1995; Hirth, 2002). However, it should be distinguished from the phenomenological plasticity for brittle deformation used in this study. It is the viscous component in our EVP constitutive model that corresponds to such non-localized flow.

Brittle deformation is characterized by the rapid loss of cohesion after yielding (Jaeger and Cook, 1976) and becomes localized into narrow fault zones. Assuming a strain-weakening rule, a classical plastic constitutive model can lead to brittle failure. Localization is meant to be an outcome of the bifurcation inherent to strain weakening

Table 3.1: List of numerical experiments

Model	Crustal thickness	Type of rheology	Plastic flow
1	Normal (7 km)	Weak*	Associated
2	Thin (4 km)	Weak	Associated
3	Thick (10 km)	Weak	Associated
4	Normal	Strong**	Associated
5	Thin	Strong	Associated
6	Thick	Strong	Associated
7	Normal	Weak	Non-associated
8	Thin	Weak	Non-associated
9	Thick	Weak	Non-associated
10	Normal	Strong	Non-associated
11	Thin	Strong	Non-associated
12	Thick	Strong	Non-associated
13	The same with model 1 except T_{mantle}=1250 °C		
14	The same with model 2 except T_{mantle}=1250 °C		
15	The same with model 4 except T_{mantle}=1250 °C		
16	The same with model 5 except T_{mantle}=1250 °C		

* Chen and Morgan (1990b).
** Mackwell et al. (1998) for crust and Chopra and Paterson (1984) for mantle.

plasticity (Rudnicki and Rice, 1975) rather than of special boundary conditions or the geometry of the domain. The Mohr-Coulomb criterion for fracture strength is adopted and specified by an internal friction angle (φ), a dilation angle (ψ), and cohesion (c). Cohesion is only poorly constrained by experiments, but we take rough estimations based on previous publications: 44 MPa for oceanic crust (Lavier et al., 2000) and 150 MPa for dunite (Hirth, 2002). The weakening rules define cohesion as piecewise linear functions of a non-negative scalar representing the amount of accumulated plastic strain, $(\lambda'^2_1 + \lambda'^2_2 + \lambda'^2_3 + \vartheta^2)^{1/2}$, where λ'_i is the i-th principal value of deviatoric plastic strain and ϑ is the volumetric plastic strain (Lavier et al., 2000; Lavier and Buck, 2002). For simplicity, we fix plastic parameters as well as the weakening rule for all models in this paper (Table 3.2).

3.3.2 Thermo-mechanical coupling

SNAC computes a time-dependent temperature field by solving the equation of heat energy conservation. The resultant temperature variations are coupled to pressure change through the thermal expansion coefficient and bulk modulus (Boley and Weiner, 1960). Although an energy feedback through work done by volume change

Table 3.2: Rheological model parameters

Symbol	Description	Model value
ρ_c	Density of crust	2900 km/m^3
ρ_m	Density of mantle	3300 kg/m^3
λ	Lamé's constant	Crust: 30 GPa
		Mantle: 60 GPa
μ	Shear modulus	Crust: 30 GPa
		Mantle: 60 GPa
A	Pre-exponential coefficient	Crust: 100 (100)*
		Mantle: 1000 (28840)*
H	Activation enthalpy	Crust: 260 (485)* kJ/mol
		Mantle: 520 (535)* kJ/mol
n	Stress exponent	Crust: 3.4 (4.7)*
		Mantle: 3.0 (3.6)*
$\dot{\epsilon}_{ref}$	Reference strain rate	10^{-16} s^{-1}
k_0	Enhanced thermal conductivity	7.5 Wm^{-1}K^{-1}
k_1	Normal thermal conductivity	3.0 Wm^{-1}K^{-1}
τ	Decay time for thermal conductivity	1 My
C_p	Isobaric heat capacity	1100 J kg^{-1}K^{-1}
α_v	Volumetric thermal expansion coefficient	3.2×10^{-5} K^{-1}
R	Gas constant	8.3145 Jmol^{-1}K^{-1}
φ	Friction angle	30°
ψ	Dilation angle	30° or 0°
C_0	Initial cohesion	Crust: 44 MPa
		Mantle: 150 MPa
$\epsilon_{ps,1}$	Parameters for piecewise linear strain softening	0.01
C_1		0.22 MPa
$\epsilon_{ps,2}$		0.05
C_2		4.4 kPa
$\epsilon_{ps,3}$		1000
C_3		0 kPa

* Values for the weak rheology; values within the parentheses for the strong rheology.

and shear heating (e.g., Regenauer-Lieb and Yuen, 2004; Kaus and Podladchkov, 2006) are potentially significant, we do not consider them. This simplification is justified by the fact that brittle failure in the form of thermal cracks is essentially tensional although gravity always adds small shear components. The transient nature of thermal stress also supports this one-way coupling. Unlike problems driven by persistent boundary loading, here thermal stress is the only driving force. Once thermal stresses are released by brittle failure, energy dissipation in the failed regions cannot be sustained.

3.4 Model setup

A series of 2-D models are constructed to represent a vertical cross-section along a straight ridge segment (Fig.3.2). A 500 km long and 50 km deep domain is discretized into 1×1 km quadrilateral elements. To avoid complexities involving ridge axial processes, the domain is assumed to be initially at a small distance from the spreading center such that the initial temperature field is 0.3 My old lithosphere given by a half-space cooling model. Temperature is fixed at 0 °C on the top surface and 1350 °C at the bottom. The effect of hydrothermal cooling is taken into account (e.g., Chen and Morgan, 1990a) through a time-dependent thermal conductivity of crust that is defined as $k = k_0 + k_1 \exp(t/\tau)$, where k_0 is the normal value for crust's thermal conductivity, k_1 is the increment for the enhanced cooling, t is time, and τ is the decay time (fixed at 1 My). This represents the decay of the intensity of hydrothermal circulation with distance from a spreading center (Anderson et al., 1977). The initially high value of k is not a necessary condition for the occurrence of brittle deformation, but is assumed because of the important role that hydrothermal activity plays in transporting heat within young oceanic crust (Chen and Morgan, 1990a). Horizontal heat fluxes are assumed to be zero on the side walls. The side and bottom boundaries have free-slip boundary conditions while the top boundary is a free surface. All the models were integrated for 10 My.

For power law creep rheologies, we use two different sets of data that represent

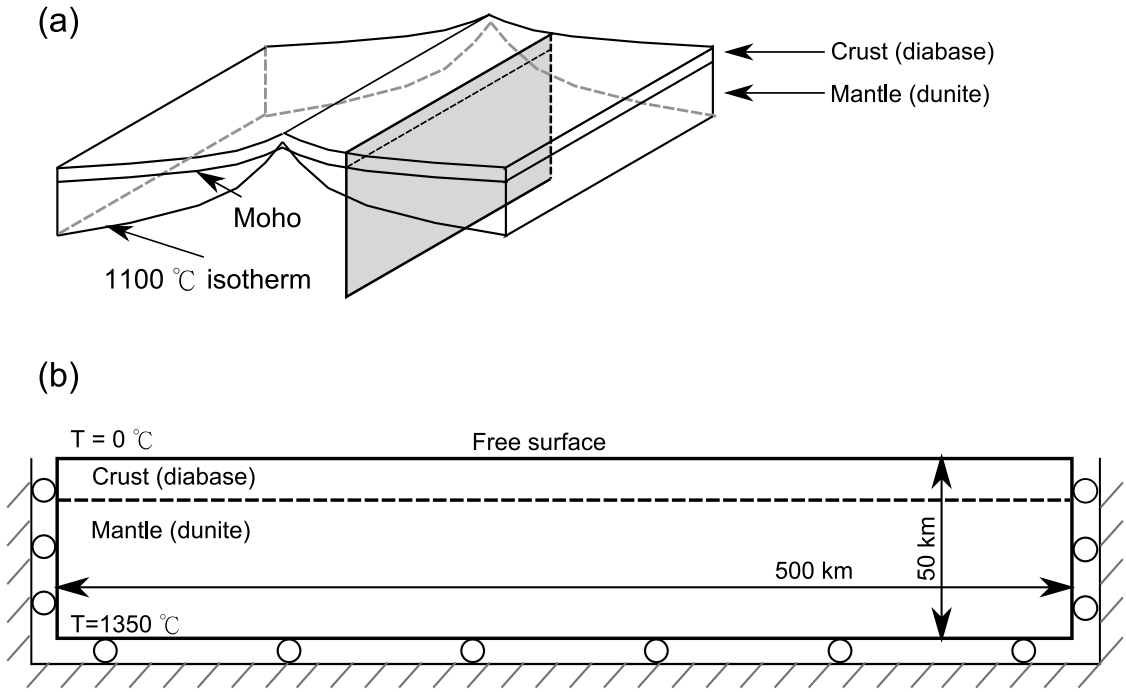

Figure 3.2: Model geometry and boundary conditions. (a) The model domain is a vertical 2-D plane parallel to the ridge axis. The hypothetical ridge segment is assumed to be straight. The oceanic lithosphere has two layers. Temperature change by cooling within the domain is equivalent to tracking a newly formed slice of lithosphere (shaded plane) with time. (b) The domain is 500 km and 50 km deep. Crust and mantle are assumed to be composed of diabase and dunite, respectively. Kinematic boundary conditions are free-slip for all the surfaces except the top one, which can deform freely. Temperature is fixed at 0 °C on top and at 1350 °C on the bottom. The initial temperature field is given by the analytic solution for half-space cooling model with the age of 0.3 My.

weak and strong lower crusts, respectively. The material parameters for weak lower crust are taken from the experimental data compiled by Kirby (1983). The corresponding mantle rheology is that used by Chen and Morgan (1990a) and Shaw and Lin (1996). This weak crustal rheology has been questioned because crustal rocks cannot be as wet as the specimens used in those experiments (e.g., Hirth et al., 1998). So, for comparison, rheologies for strong lower crust composed of dry diabase (Mackwell et al., 1998) and dunite (Chopra and Paterson, 1984) are also used.

Crustal thickness is varied so as to represent several different tectonic environments. Crustal thickness and its along-axis variations are sensitive to plate tectonic environments. For instance, fast spreading centers have relatively uniform thicknesses whereas slow ones show Moho depth variations of a few km (Macdonald et al., 1991; Macdonald, 1998). In addition, proximity to hot spots or cold mantle is also known to affect crustal thickness (e.g., Smallwood and White, 1998). Crustal thickness was emphasized in the context of the axial morphology of spreading ridges due to the potential "decoupling" effect (Chen and Morgan, 1990b). If crust is sufficiently thick, then it can have a weak lower crust that decouples the brittle upper part from the mantle. The wide decoupling zone leads to plastic failure concentrated only at the spreading center and topography close to isostatic equilibrium. In contrast, a narrow decoupling zone enhances the degree of coupling between crustal deformation and mantle flow such that necking occurs in a finite plastic failure zone creating an axial valley (Chen and Morgan, 1990b). Chen and Morgan (1990b) used this model to explain the presence or absence of an axial valley at spreading centers that have anomalously thin or thick crust for their spreading rate. The causes for anomalous crustal thickness could include proximity to a hot spot, anomalous mantle temperature, or the cold edge effect at the ridge-transform intersection. Bell and Buck (1992) also suggested that thick crust due to hot spot activity might compensate for the influence of 3-D upwelling, implying that tectonic environments can differentiate the patterns of ridge segmentation even without variations in mantle flow. To investigate this potentially critical role of crustal thickness, models have one of the following three values: Thin (4 km), normal (7 km), and thick (10 km). For simplicity, models do

not include lateral variations of thickness. The complete list of models and parameter values is given in Tables 3.1 and 3.2, respectively.

3.5 Results

3.5.1 Models with weak crust

The temporal evolution of topography, temperature, viscosity, and plastic strain for the model with weak and normal thickness (7 km) crust (model 1 in Table 3.1) is shown in Fig.3.3. The viscosity field is almost entirely determined by temperature while the dependence on stress is minimal. Lower viscosities are consistently found in the lower crust. Although brittle deformation occurred in the high viscosity uppermost part of the crust and mantle, the amount of plastic strain was only about 1%. The initially uniform brittle deformation in the mantle started to evolve into regularly spaced discrete zones at 4 My. These discrete brittle zones have a visually estimated spacing of 7-10 km. Cooling continues to drive brittle deformation so that by 7 My, some discrete brittle zones have started to accumulate more strain at the expense of others.We term the further growing brittle zones primary cracks and those that stopped growing secondary cracks. These terms are defined in a relative sense at any given time. Some primary cracks at one time might become secondary later if only a selected subset of the primary cracks continue to grow. Fig.3.4 shows magnified images of the upper-left part of the domain in Fig.3.3. The images compare the plastic strain and the second invariant of deviatoric stress (σ_{II}) at 4 and 7 My and show the selective growth of primary cracks from a set of initial cracks that are more numerous and finely spaced. The maximum of σ_{II} increases with the depth extent of brittle zones because it is constrained by a linear pressure-dependence of the yield stress, like strength envelopes used in previous studies (e.g., Parmentier and Haxby, 1986; Haxby and Parmentier, 1988; Wessel, 1992). As seen from the plastic strain (Fig.3.3), the primary localized zones of brittle deformation that continue to grow after 7 My have a spacing of about 15-25 km. The overall subsidence of topography

occurs because of isotropic thermal contraction. So, the topography at a given time step is presented with the mean removed. No cracks could completely penetrate the whole crustal layer. Even the primary cracks did not create significant topographic relief on the top surface. Nucleated in the uppermost mantle, they did not propagate into the overlying lower crust. This discontinuity of brittle deformation across the lower crust is consistent with the existence of a weak lower crust.

Models with different crustal thicknesses follow the same sequence of brittle deformation: Initially uniform brittle deformation in the high viscosity regions, subsequent localization forming discrete brittle zones, and differentiation of brittle zones into primary and secondary cracks. However, they also produced significant differences in terms of the distribution of plastic strain and topography (Fig.3.5a). We summarize results from two models for a weak crust (model 2 and 3 in Table 3.1), of which crustal thickness is varied from 7 km (normal) to 4 km (thin) and 10 km (thick), respectively. They are compared to the normal thickness model described above.

The thin crust model created grabens and half-grabens with ∼50 m of subsidence and a 100-150 km spacing (Fig.3.5a). The topography between grabens is concave upward, indicating that thermal contraction is stronger in the upper part than in the lower part of lithosphere so that a positive bending moment is generated. In contrast to the normal crustal thickness model, the model with the thin crust accumulated more plastic strain (maximum 4%). The primary brittle zones connected to grabens clearly show a V-shaped distribution of accumulated plastic strain that is continuous across the lower crust. These differences between the normal (7 km) and thin (4 km) crust models can be attributed to differences in temperature within the lower crust. In the thin crust model, lower crust is colder and the exponential dependence of viscosity on temperature renders the lower crust essentially brittle.

The thick crust model accumulated a plastic strain of only ∼0.4, negligible compared to the values from models with thinner crust, and the topography is essentially flat (Fig.3.5a). Although the highly viscous parts of the model did yield, the deformation never localized. Thus, the thick crust model did not develop topography associated with primary cracks other than the uniform subsidence due to thermal

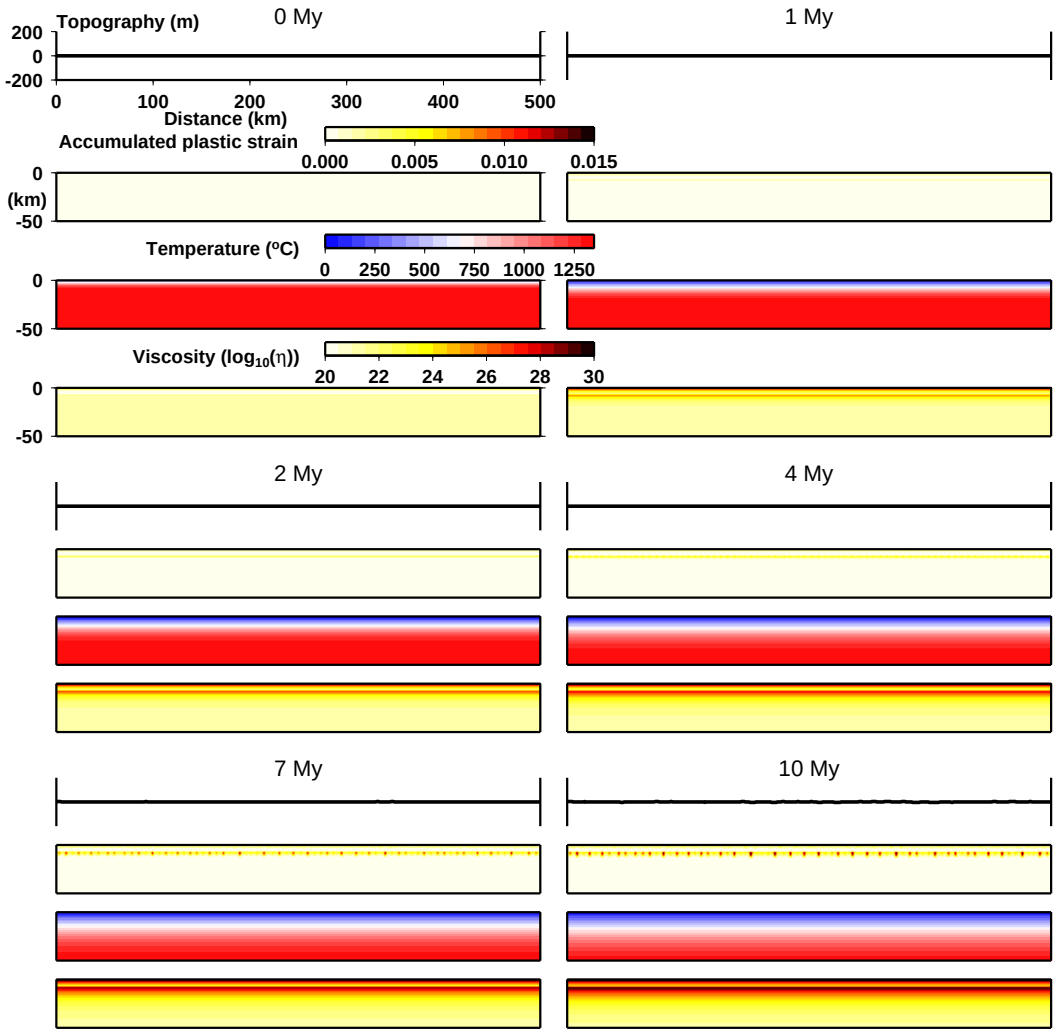

Figure 3.3: Evolution of topography, temperature, viscosity, and brittle deformation (plastic strain) for the model with weak and normal thickness crust (model 1). Viscosity fields directly reflect temperature change, but low-viscosity lower crust highlights the two-layer structure. Brittle zones (with a ∼10 km spacing) start to emerge by 7 My, and some brittle zones continue deforming as cooling proceeds. These later brittle zones create valleys on the surface with a relief of about 20 m by 10 My.

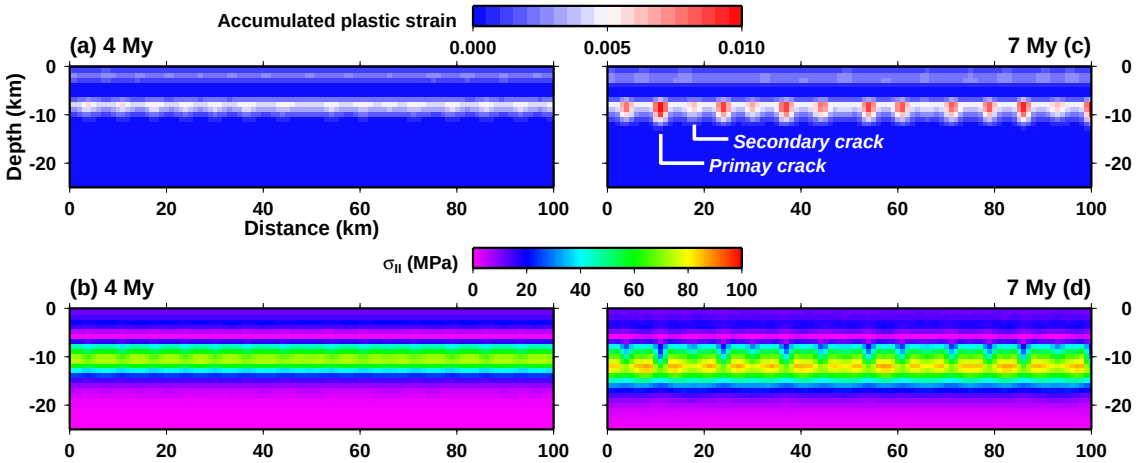

Figure 3.4: The upper left part of the model shown in Fig.3.3 is magnified to compare the brittle zones at 4 and 7 My. Each panel covers 0-100 km in the ridge-parallel direction and 0-25 km in depth. The accumulated plastic strain and the second invariant of deviatoric stress (σ_{II}) at 4 My are shown in (a) and (b), respectively; those at 7 My in (c) and (d).

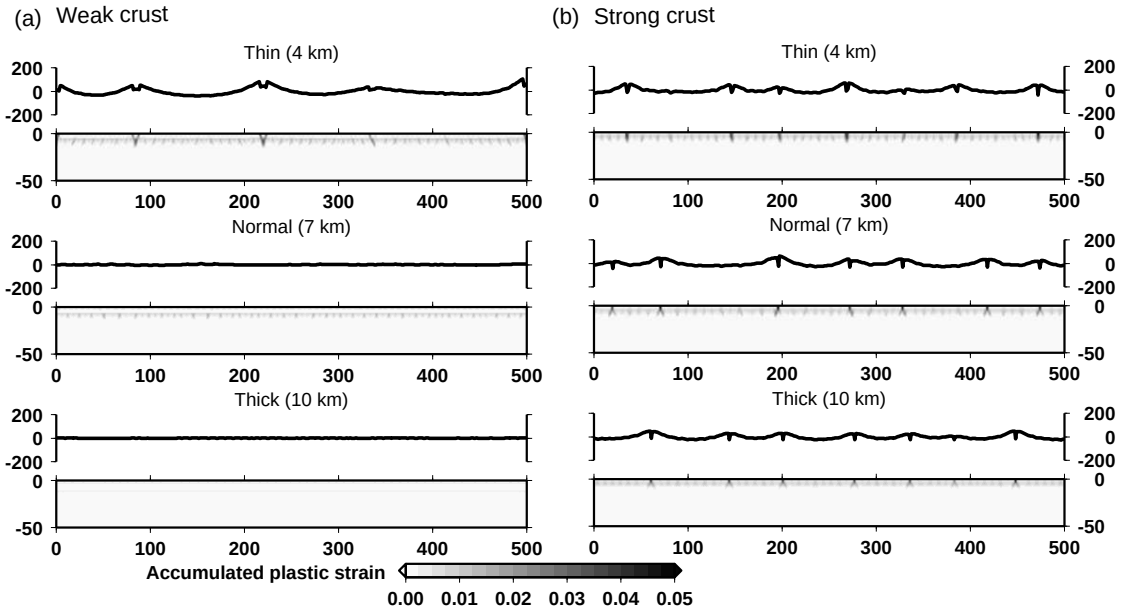

Figure 3.5: Topography (in m) and accumulated plastic strain for the models with associated plasticity at 10 My. (a) Weak crust models with varied crustal thicknesses (model 1-3 in Table 3.1). (b) Models with the strong crustal rheology (model 4-6).

contraction.

3.5.2 Models with strong crust

The model with a strong and 7 km-thick (normal thickness) crust (model 4 in Table 3.1) is clearly distinguished from those of the weak crust models in terms of plastic strain and viscosity (Fig.3.6). The two layer structure of crust is obscured in this model's viscosity because lower crustal viscosities are consistently higher. Persistently active primary cracks are vertical and emerge as early as at 1 My with a spacing of 70-100 km. The topography is characterized by narrow troughs connected to primary cracks and the concave upward segments between the troughs. In contrast to the weak crust models, the primary cracks are nearly vertical, not V-shaped, and develop much earlier: it required 4 My in weak models (Fig.3.3), 1 My in this case.

Reduced or increased crustal thickness in the strong crust models (models 5 and 6 in Table 3.1) did not have as strong an influence as in the weak crust models (Fig.3.5b). All models are similar in terms of temporal evolution and resultant topography although the position of primary cracks was not fixed in space. Amplitude of the concave-upward topography in the trough-bounded segments is nearly constant regardless of crustal thickness.

Models with different crustal thicknesses show differences in the geometry and propagation depth of primary cracks (Fig.3.5b). The models of normal and thick crust have primary cracks that are vertical near the surface and branch towards greater depths, making an inverted V-shape. In contrast, the primary cracks in the thin crustal model remain vertical throughout their extent. The propagation depth is about 10 km in the models with thin and normal crust, while it is smallest with a thick crust ($\sim$5 km). The maximum of accumulated plastic strain is similar in all three strong crust models, but the secondary cracks of the thin crust model exhibit larger plastic strain than the other models.

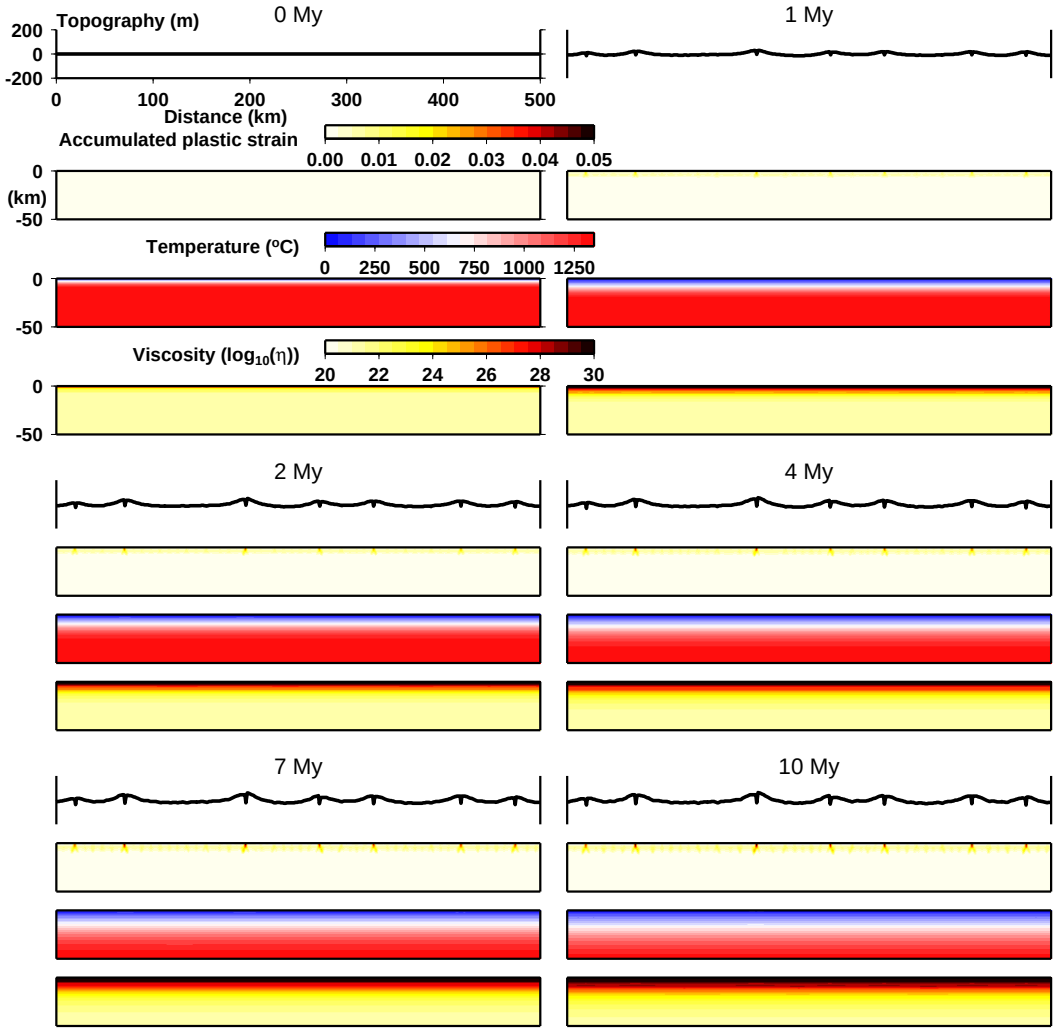

Figure 3.6: Same as Fig.3.3, but the results from the model with a strong and 7 km-thick (normal thickness) crust.

3.5.3 Non-associated plasticity

The previously described results were obtained under the assumption of an associated flow rule: i.e., the dilation angle was set to be equal to the friction angle. We took advantage of the associated flow rule as a numerical means to achieve significant opening in the band of localized strain. However, non-associated flow rules, in which dilation angle is not equal to the friction angle, are usually considered more appropriate for frictional materials like rocks (e.g., Rudnicki and Rice, 1975). Among the possible choices of non-associated plasticity, the assumption of plastic incompressibility, i.e., with a dilation angle of 0° was suggested in studies of shear bands in rocks (e.g., Poliakov and Herrmann, 1994). Although this condition is extreme in the sense that volumetric plastic strain is completely prohibited, we evaluate its effects for comparison. Models with strong and weak crustal rheology as well as variable crustal thickness were computed with a dilation angle of 0° (model 7-12 in Table 3.1). Since all the other parameters and the initial and boundary conditions were the same as described in the previous two sections, these models followed a very similar sequence of temporal evolution while exhibiting substantial differences at the same time. The assumption of plastic incompressibility enables only shear bands to appear, not cracks with opening. However, we use the descriptive terms, primary and secondary cracks, for continuity with the previous discussion. In the following, regardless of the rule used for plastic flow, a primary crack refers to a localized band of plastic strain that penetrates crust and creates a topographic signature, while zones of localized plastic strain that stopped growing before propagating into crust are called secondary cracks.

Differences found in the weak crustal models involve the geometry of primary cracks and resultant topography (Fig.3.7a). Among the models with a weak crust, only the one with thin crust developed significant topography. As in the models with an associated flow rule, this model shows V-shaped primary cracks,which create grabens on the top surface spacing and relief larger than those cases with the associated flow rule (Fig.3.5a). The maximum plastic strain, $\tilde{5}\%$, is larger than 1.5% of the corresponding model of an associated flow rule. The spacing of primary cracks

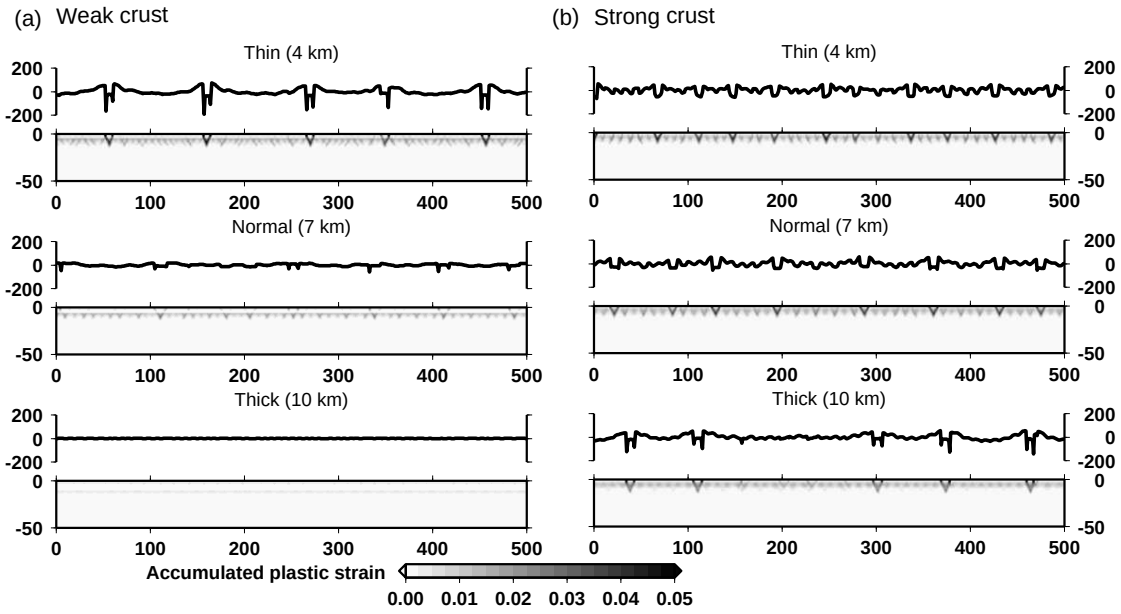

Figure 3.7: Same as Fig.3.5, but for the models with zero dilation angle. (a) Weak crust models with varied crustal thicknesses (models 7-9 in Table 3.1). (b) Models with the strong crustal rheology (models 10-12).

decreased slightly compared to the counterpart with an associated flow rule such that it shows a range of 80-110 km.

The non-associated plasticity in the strong crustal models also resulted in differences in the brittle deformations (Fig.3.7b). In contrast to the corresponding models with non-zero dilation angle (Fig.3.5b), all the strong crustal models developed V-shaped primary cracks and associated grabens. The spacing of primary cracks shows a clear positive correlation with the thickness of crust. The average spacing of primary cracks varies from 49 km in the thin crust model to 99 km in the thick crust model (Table 3.3). When the associated flow rule was used, the relationship between the spacing of primary cracks and crustal thickness was not clear (Fig.3.8a).

Table 3.3: Summary of average spacing of primary cracks at 10 My

Plastic flow rule		Associated	Non-associated ($\psi = 0°$)
Strong	Thin	73±23 km*	47±13 km
	Normal	76±28 km	62±17 km
	Thick	71±22 km	105±50 km
Weak	Thin	125±34 km	100±14 km
	Normal	N/A	N/A
	Thick	N/A	N/A

*Mean±standard deviation

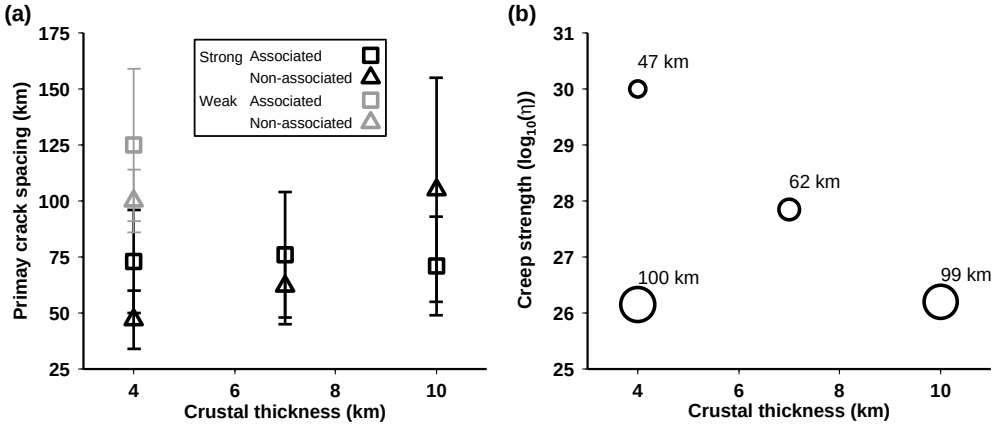

Figure 3.8: (a) Plot of the primary crack spacing at 10 My versus crustal thickness for different combinations of crustal rheology and the plastic flow rule. (b) Plot of the primary crack spacing with respect to crustal thickness and creep strength of lower crust. Only the cases with non-associated plasticity ($\psi = 0°$) are plotted. The crack spacing is denoted by labels and also represented by the sizes of symbols. The creep strength is represented by the logarithm of viscosity (log10(η)) taken from the bottom layer of crust in each model at 10 My and the values of the other parameters are listed in Table 3.3.

3.6 Discussion

3.6.1 Effects of crustal thickness and creep strength

The models show that creep strength and crustal thickness strongly influence brittle deformation by the release of thermal stresses. Through the centers of surface troughs (grabens) that are connected to the primary cracks at depth, we measure the average spacing between the primary cracks (Table 3.3; Fig.3.8).

Crustal thickness determines whether primary cracks are created. If the crust is thicker than a global mean (6-7 km, (Chen, 1992; White et al., 1992)) and thus

has a weak lower part, then the primary cracks do not develop as the stress in the uppermost mantle is released through creep before being transferred to the surface. When the crust is thinner than a threshold value, the entire crustal layer becomes sufficiently cold and strong to create primary cracks. If the creep strength of the crust is "strong", then the role of crustal thickness is less important than when the crust is weak. When the lower crust is sufficiently strong, then primary cracks are always created, at least for the range of crustal thicknesses tested.

When the non-associated flow rule is used in the models, crustal thickness clearly determines the spacing of primary cracks. When a non-associated flow rule is assumed by setting the dilation angle to zero, plastic strain cannot have a volumetric component. Models with a zero dilation angle demonstrate this effect by creating primary and secondary cracks in the non-vertical maximum shear direction determined by thermal stress and gravity. In addition, when the crust is strong, the spacing between primary cracks is proportional to crustal thickness: as the crustal thickness increases from 4 to 10 km, spacing increased from 49 to 99 km (see the trend of black triangles in Fig.3.8a). This relationship can be placed within the context of Lachenbruch's analysis (1962). The temperature drop at 4-7 km depth leads to thermal stresses in either the crust or mantle that depends on crustal thickness. Since the mantle's elastic moduli are larger than those of the crust, the amount of thermal stress is larger when the crust is thin, while smaller thermal stresses are available in the thick crust model. According to the theory of thermal cracks, when the ambient stress (i.e., thermal stress prior to brittle deformation) is higher, the spacing of thermal cracks decreases because the size of the stress relief zone shrinks. As a result, the thinner crust develops more finely spaced primary cracks.

One of the parameters Lachenbruch (1962) considered important in determining the crack spacing is the depth extent of cracks. In his analysis, the deeper cracks have a larger zone of stress relief resulting in a larger crack spacing. However, in our models, cracks always stop propagating downward at some depth regardless of their class, primary or secondary, because yield stress increases with pressure. In spite of the more or less constant depth extent of primary cracks, the differences in the crack

spacing are still observed, indicating that the vertical extent is not a major controlling factor determining crack spacing compared to crustal thickness and creep strength.

Another contribution to the correlation between crustal thickness and crack spacing comes from elastic unloading that occurs outside a shear band after the onset of localization (Vermeer, 1990). Elastic unloading occurs only when the plasticity is non-associated, and the amount of unloading is proportional to yield stress (Vermeer, 1990, Le Pourhiet, pers. comm., 2007). Being pressure-dependent, the yield stress of mantle directly below the Moho is smaller when the crust is thin compared to when it is thick. Consequently, a thin crust experiences a small stress drop with a relatively large ambient stress as a result, while a thick crust goes through a large stress drop reaching a relatively small ambient stress. The different values of ambient stress due to different crustal thickness leads to variations in the primary crack spacing as inferred from Lachenbruch's model described above. Furthermore, the lack of elastic unloading might be the reason the correlation is not obvious in the models with associated plasticity.

3.6.2 Implications of the sensitivity to crustal thickness and creep strength

The sensitivity of the spacing of primary cracks to crustal thickness suggests that the non-uniform tectonic environment of a mid-ocean ridge system can exert a fundamental, but indirect, control over local changes in the ridge system's brittle deformation. Non-uniform mantle temperature and proximity to hot spots can indirectly contribute to brittle deformation through spatial and temporal variations in crustal thickness. For instance, models with mantle temperatures that are low (models 13-16 in Table 3.1) demonstrate the relative insignificance of mantle temperature (Fig.3.9). With the mantle temperature of 1250 °C, lower than in models 1-12 by 100 °C, the magnitude of thermal stress still exceeds the brittle strength of oceanic lithosphere by a substantial amount at shallow depths. As a result, the relationship between crustal thickness and primary cracks is the same as in those models with a higher mantle

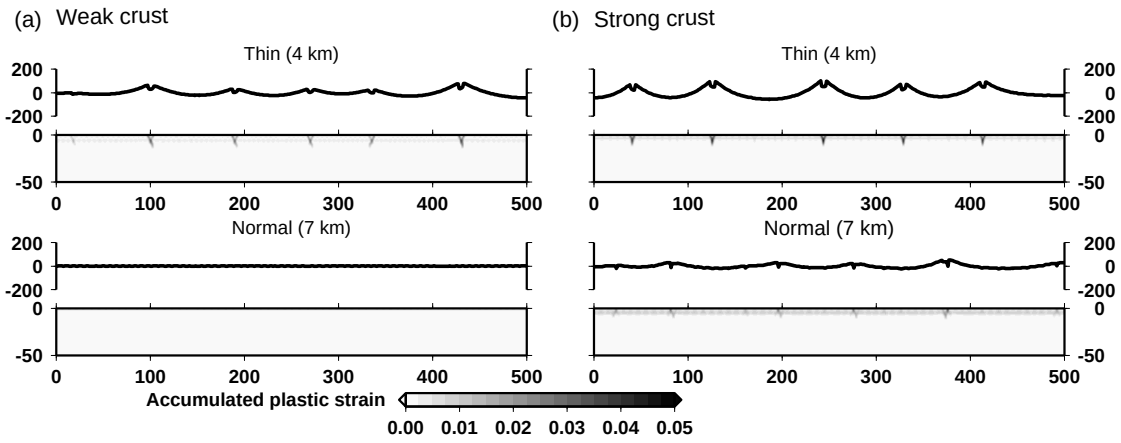

Figure 3.9: Same as Fig.3.5, but the mantle temperature is lowered to 1250 °C from 1350 °C.

temperature. Similarly, the effects of creep strength are not much modified by lowered mantle temperature: The stronger crust has a higher threshold thickness, below which topography associated with primary cracks can be created as in the models with a higher temperature. Consequently, a 7 km-thick crust can develop primary cracks when the lower crust is strong (Fig.3.9).

Evidence for the causal relationship between crustal thickness and the brittle deformation of oceanic lithosphere can be found along the Reykjanes ridge and the Australian-Antarctic Discordance (Fig.3.9). The crust of the Reykjanes ridge is known to be thicker than 10 km (e.g., Smallwood and White, 1998). The lack of fracture zones in this ridge system appears consistent with the subdued brittle deformation and the lack of primary cracks in the thick crust models. The distinction between the Reykjanes ridge and other slow-spreading centers has previously been attributed to thick crust (Chen and Morgan, 1990a; Bell and Buck, 1992). The opposite effects of a thin crust are found in the AAD. The evolution of the AAD was reconstructed by Marks et al. (1999). They suggested that the increase in the number of ridge segments and their offset might be a local outcome of amagmatic extension rather than of regional influence from cold mantle. Based on the detailed observations on the central region of the AAD, Okino et al. (2004) identified asymmetric spreading on oceanic detachments as a dominant mode of extension and attributed it to low

magma supply and cold mantle. Our models with the lowered mantle temperature suggest that the reduced amount of thermal stress due to the cooler mantle is not as significant for brittle deformation as the reduced crustal thickness. We can infer that the magma-starved spreading centers produce thinner crust, and the thinner crust, as shown in this study, facilitates brittle deformation due to cooling, resulting in more rugged topography and more fracture zones.

Our results also show a strong sensitivity of brittle deformation to creep strength of the crust and mantle. Our models show that primary cracks are created regardless of crustal thickness when a high creep strength for dry diabase is used, while crustal thickness governs the degree of fracturing when creep strength is low. However, experiments and observations suggest that the mid-ocean ridge basalts and gabbros are only 5 % saturated with water (Hirth et al., 1998). Even at a wet hot spot like the Reykjanes ridge, the observed maximum water content of 0.4 wt.% (Nichols et al., 2002), although relatively high, is only 10 % of the solubility (e.g., Dixon et al., 1995). Therefore, the major effect of the higher water content at the Reykjanes ridge would be an enhanced degree of melting and thus a thicker crust rather than lowered creep strength. The weakening effect due to the wet mantle source, however, cannot be completely ignored. Our results showed that even the thick crust developed primary cracks when the creep strength of dry diabase was used, which is in contrast with the lack of fracture zones at the Reykjanes ridge. The surface topography was comparably smooth only in the models with weak creep strength.

The spacing of primary cracks from our models is mapped to a two dimensional space spanned by the crustal thickness and lower crustal creep strength (Fig.3.8b). For non-associated plasticity (ψ=0°), models with thin and strong crust have the smallest crack spacing; crack spacing increases as the crust becomes thick and weak (Fig.3.8b). This relationship is expected because the creep strength of lower crust is determined by the crustal thickness. Another trend is found between the crack spacing and the creep strength for a constant crustal thickness (4 km), where the crack spacing is inversely proportional to the creep strength. In addition, sufficiently weak lower crusts with the creep strength of $\sim 10^{26}$ Pa·s do not show significant correlation

with thickness. These trends suggest that creep strength and crustal thickness can independently influence crack spacing.

3.6.3 Flexure of the segments

The upward concavity of all the primary crack-bounded segments indicate that primary cracks impose local boundary conditions so that the segments are free to contract horizontally, which generate a compressional stress field on the top of a cooling and growing plate as shown in previous studies (Parmentier and Haxby, 1986; Haxby and Parmentier, 1988; Wessel, 1992). The free-slip boundary conditions of the whole domain prohibit horizontal contraction and might be expected to result in a stress field with the opposite sign. A cooling plate with its boundaries fixed develops tension on the top due to inhibited contraction (e.g., Turcotte, 1974). The boundary conditions of the whole domain initially do lead to the buildup of tensional stresses on the top of lithosphere, but only until cracks appear. The full thermal stresses can be decomposed into thermal contraction stresses and thermal bending stresses for convenience (Turcotte, 1974; Haxby and Parmentier, 1988). The formation of crack-bounded segments releases the thermal contraction stresses and renders the boundary conditions of the whole domain irrelevant for the behavior of the segments. The segments, now with nearly free boundary conditions imposed by the weak primary cracks, subsequently deform with the remaining thermal bending stresses. Through this sequence of events, the concave upward topography of a freely-shrinking plate is obtained even though the domain itself does not horizontally contract.

3.6.4 Implications for ridge axial processes

The plane strain assumption implies that the cracks would extend all the way to the spreading centers, essentially determining the lengths of ridge segments. If we assume that the primary cracks correspond to fracture zones, the spacing of transform faults and associated fracture zones can be interpreted as that of primary cracks. However, this model must be too simple to be applied to actual mid-ocean ridges.

For instance, a young and hot lithosphere near fast spreading centers would not have accumulated sufficiently large thermal stress and even the available thermal stress is efficiently released by creep rather than by brittle deformation. As a result, thermal cracks initiated off-axis might not have a dominant control on the near-axis brittle deformations including the spacing between first order discontinuities. On the other hand, the increased number of primary cracks in a thin crustal model suggests that the undulating crustal thickness at slow-spreading centers might determine the locations in such a way that brittle deformation occurs only at the relatively thin parts. It might be also possible that hydrothermal cooling is enhanced along thermally induced fractures triggering magmatic segmentation with a similar spacing. Since these hypotheses now include the second-order segments with associated crustal thickness variation and spatially cover both on- and off-axis regions, fully 3-D models as well as magma dynamics would be required to address such possibilities.

The along-axis variations of crustal thickness appear necessary for achieving the observed topographic amplitude. The relief across the primary cracks as well as within a segment is 10s to 100 m, which is considerably smaller than that of actual fracture zones ($\leq$1 km). A simple calculation assuming isostatic equilibrium shows that 3 km of crustal thickness difference between the center and the edge of a segment can cause a relief of about 500 m, a significant contribution on top of bending due to thermal stress ($\sim$100 m). There is also a large discrepancy between the observed length of the first order segments and the primary crack spacing of our models: The observed lengths are 600$\pm$300 km along fast spreading ridges and 400$\pm$200 km for slow ones (Macdonald et al., 1991) while the segments bounded by primary cracks in our models are consistently shorter than 200 km. The values from our models (Table 3.3) are closer to lengths of the second order segments: 140$\pm$90 and 50$\pm$30 km for fast- and slow-spreading ridges, respectively (Macdonald et al., 1991). The discrepancy and the similarity might be only apparent because the association of primary cracks with fracture zones is an assumption and our models cannot have true second order segments that show crustal thickness variations and temporal changes in length. In any case, improved knowledge of the rheological properties and failure mechanism is

one of the prerequisites for a more quantitative analysis of the crack spacing from numerical models.

3.7 Conclusion

We show that crustal thickness, crustal creep strength, and the rule for plastic flow can substantially influence the brittle deformation of oceanic lithosphere. Crustal thickness determines whether brittle deformation would evolve into primary cracks or stay at secondary cracks without associated topographic features. Primary cracks only emerge when a crust is thinner than a certain threshold. Lower crustal creep strength has a net effect of shifting this threshold: When the creep strength is higher, the threshold is raised so that primary cracks emerge even when the crust is 10 km-thick. In contrast, a weaker crust with a smaller thickness did not develop primary cracks. The associated flow rule allows dilatational deformation resulting in vertical extensional primary cracks and the associated narrow troughs on the top surface. In contrast, cracks become V-shaped and grabens are associated with the primary cracks when a non-associated flow rule with a zero dilation angle is imposed. Since the temporal and spatial variations in crustal thickness reflect changes in the tectonic settings of a ridge system, the brittle deformation around the ridge system can also be attributed to tectonic origins. The larger spacing of thermally induced brittle deformation in a thicker crust provides a qualitative explanation for the correlation between anomalously thick crust and the lack of fracture zones in the Reykjanes ridge. By the same token, the connection between thin crust and increased number of fracture zones within the AAD appears parallel to the small spacing of primary cracks in a thin crust.

References

Albert, R., Phillips, R., Dombard, A., Brown, C., 2000. A test of the validity of yield strength envelope with an elastoviscoplastic finite element model. Geophys. J. Int. 140, 399–409.

Anderson, R. N., Langseth, M. G., Scalter, J. G., 1977. The mechanisms of heat transfer through the floor of the Indian Ocean. J. Geophys. Res. 82, 3391–3409.

Barnouin-Jha, K., Parmentier, E., Sparks, D., 1997. Buoyant mantle upwelling and crustal production at oceanic spreading centers: On-axis segmentation and off-axis melting. J. Geophys. Res. 102 (B6), 11979–11989.

Bathe, K.-J., 1996. Finite Element Procedure. Prentice-Hall, Upper Saddle River, New Jersey.

Bell, R., Buck, W., 1992. Crustal control of ridge segmentation inferred from observations of the Reykjanes ridge. Nature 357, 583–586.

Bird, P., 2003. An updated digital model of plate boundaries. Geochem. Geophys. Geosyst. 4, 1027. doi:10.1029/2001GC000252.

Boley, B., Weiner, J., 1960. Theory of Thermal Stresses. Wiley, New York.

Brais, A., Rabinowicz, M., 2002. Temporal variations of the segmentation of slow to intermediate spreading mid-ocean ridges 1. synoptic observations based on satellite altimetry data. J. Geophys. Res. 107 (B5, 2098), 10.1029/2001JB000533.

Bunch, A., Kennett, B., 1980. The crustal structure of the Reykjanes Ridge at 59 degrees 30′N. Geophys. J. Roy. Astr. S. 61 (1), 141–166.

Carbotte, S., Small, C., Donnelly, K., 2004. The influence of ridge migration on the magmatic segmentation of mid-ocean ridges. Nature 429, 743–746.

Chen, Y., 1992. Oceanic crustal thickness versus spreading rate. Geophys. Res. Lett. 19 (8), 753–756.

Chen, Y., Morgan, W. J., 1990a. A nonlinear rheology model for mid-ocean ridge axis topography. J. Geophys. Res. 95 (B11), 17583–17604.

Chen, Y., Morgan, W. J., 1990b. Rift valley/no rift valley transition at mid-ocean ridges. J. Geophys. Res. 95, 17,571–17,581.

Choblet, G., Parmentier, E., 2001. Mantle upwelling and melting beneath slow spreading centers: Effects of variable rheology and melt productivity. Earth Planet. Sci. Lett. 184, 589–604.

Chopra, P., Paterson, M., 1984. The role of water in the deformation of dunite. J. Geophys. Res. 89 (B9), 7861–7876.

Collette, B., 1974. Thermal contraction joints in a spreading seafloor as origin of fracture zones. Nature 251, 299–300.

Cundall, P., 1989. Numerical experiments on localization in frictional materials. Ingenieur Archiv. 58, 148–159.

de Souza Neto, E., Andrade Pires, F., Owen, D., 2005. F-bar-based linear triangles and tetrahedra for the finite strain analysis of nearly incompressible solids. part I: Formulation and benchmarking. Int. J. Num. Meth. Engng. 62 (3), 353–383.

Dixon, J. E., Stolper, E. M., Holloway, J. R., 1995. An experimental study ofwater and carbon dioxide solubilities in mid-ocean ridge basaltic liquids. part i: Calibration and solubility models. J. Petrology 36, 1607–1631.

Haxby, W. F., Parmentier, E. M., 1988. Thermal contraction and the state of stress in the oceanic lithosphere. J. Geophys. Res. 93 (6), 6419–6429.

Hayes, D., Conolly, J., 1972. Morphology of the southeast Indian Ocean. In: Hayes, D. (Ed.), AGU, Washington, D.C. Vol. 19 of Antarctic Oceanography II: The

Australian-New Zealand Sector, Antarct. Res. Ser. AGU, Washington, D.C., pp. 125–145.

Hirth, G., 2002. Laboratory constraints on the rheology of the upper mantle. In: Karato, S., Wenk, H.-R. (Eds.), plastic deformation of minerals and rocks. Vol. 51 of Reviews in mineralogy & geochemistry. The Mineralogical Society of America, pp. 97–120.

Hirth, G., Escartin, J., Lin, J., 1998. The rheology of the lower oceanic crust: Implications for lithospheric deformation at mid-ocean ridges. In: Buck, W. R., Delaney, P. T., Karson, J. A., Lagabrielle, Y. (Eds.), Faulting and magmatism at mid-ocean ridges. Vol. 106 of Geophysical Monograph. AGU, pp. 291–303.

Hirth, G., Kohlstedt, D., 1996. Water in the oceanic upper mantle: Implications for rheology, melt extraction and the evolution of the lithosphere. Earth Planet. Sci. Lett. 144, 93–108.

Jaeger, J., Cook, N., 1976. Fundamentals of Rock Mechanics, 2nd Edition. Chapman and Hall, London, United Kingdom (GBR).

Karato, S., 1986. Does partial melting reduce the creep strength of the upper mantle? Nature 319, 309–310.

Kastens, K. A., 1987. A compendium of causes and effects of processes at transform faults and fracture zones. Rev. Geophys. 25, 1554–1562.

Kaus, B., Podladchkov, Y., 2006. Initiation of localized shear zones in viscoelastoplastic rocks. J. Geophys. Res. 111 (B04412), doi:10.1029/2005JB003652.

Kirby, S., 1983. Rheology of lithosphere. Rev. Geophys. 21, 1458–1487.

Klein, E. M., Langmuir, C. H., Staudigel, H., 1991. Geochemistry of basalts from the Southeast Indian Ridge, 115°E-138°E. J. Geophys. Res. 96, 2089–2107.

Kohlstedt, D., Evans, B., Mackwell, S., 1995. Strength of the lithosphere: Constraints imposed by laboratory experiments. J. Geophys. Res. 100 (B9), 17587–17602.

Lachenbruch, A., 1962. Mechanics of Thermal Contraction Cracks and Ice-wedge Polygons in Permafrost. Special Paper - Geological Societry of America. The Geological Society of America.

Lavier, L. L., Buck, W., 2002. Half graben versus large-offset low-angle normal fault: Importance of keeping cool during normal faulting. J. Geophys. Res. 107 (B6, 2122), 10.1029/2001JB000513.

Lavier, L. L., Buck, W. R., Poliakov, A. N. B., 2000. Factors controlling normal fault offset in an ideal brittle layer. J. Geophys. Res. 105 (B10), 23,431–23,442.

Lin, J., Phipps Morgan, J., 1992. The spreading rate dependence of three-dimensional mid-ocean ridge gravity structure. Geophys. Res. Lett. 19 (1), 13–16.

Macdonald, K., 1998. Linkages between faulting, volcanism, hydrothermal activity and segmentation of fast spreading centers. In: Buck, W. R., Delaney, P. T., Karson, J. A., Lagabrielle, Y. (Eds.), Faulting and magmatism at mid-ocean ridges. Vol. 106 of Geophysical Monograph. AGU, pp. 27–58.

Macdonald, K., Scheirer, D., Carbotte, S., 1991. Mid-ocean ridges: Discontinuities, segments and giant cracks. Science 253 (5023), 986–994.

Mackwell, S. J., Zimmerman, M. E., Kohlstedt, D. L., 1998. High-temperature deformation of dry diabase with application to tectonics on Venus. J. Geophys. Res. 103, 975–984.

Magde, L., Sparks, D., 1997. Three-dimensional mantle upwelling, melt generation, and melt migration beneath segment slow spreading ridges. J. Geophys. Res. 102 (B9), 20571–20583.

Marks, K., Stock, J., Quinn, J., 1999. Evolution of the Australian-Antarctic discordance since Miocene time. J. Geophys. Res. 104 (B3), 4967–4981.

Marti, J., Cundall, P., 1982. Mixed discretization procecure for accurate modelling of plastic collapse. Int. J. Numer. Anal. Methods Geomech. 6, 129–139.

Murton, B., Parson, L., 1993. Segmentation, volcanism and deformation of oblique spreading centres: A quantative study of the Reykjanes ridge. Tectonophysics 222, 237–257.

Nichols, A. R. L., Carroll, M. R., Höskuldsson, A., 2002. Is the Iceland hot spot also wet? Evidence from the water contents of undegassed submarine and subglacial pillow basalts. Earth Planet. Sci. Lett. 202, 77–87.

Okino, K., Matsuda, K., Christie, D., Nogi, Y., Koizumi, K., 2004. Development of oceanic detachment and asymmetric spreading at the Australian-Antarctic Discordance. Geochem. Geophys. Geosyst. 5, Q12012, doi:10.1029/2004GC000793.

Parmentier, E., Phipps Morgan, J., 1990. Spreading rate dependence of three-dimensional structure in oceanic spreading centres. Nature 348, 325–328.

Parmentier, E. M., Haxby, W. F., 1986. Thermal stresses in the oceanic lithosphere: Evidence from geoid anomalies at fracture zones. J. Geophys. Res. 91 (7), 7193–7204.

Poliakov, A., Hermann, H., Podladchikov, Y., Roux, S., 1994. Fractal plastic shear bands. Fractals 2, 567–581.

Poliakov, A., Herrmann, H., 1994. Self-organized criticality of plastic shear bands in rocks. Geophys. Res. Lett. 21 (10), 2143–2146.

Poliakov, A., Podladchikov, Y., Dawson, E., Talbot, C., 1996. Salt diapirism with simultaneous brittle faulting and viscous flow. Geol. Soc. Spec. Publ. 100, 291–302.

Poliakov, A., Podladchikov, Y., Talbot, C., 1993. Initiation of salt diapirs with frictional overburdens: Numerical experiments. Tectonophysics 228 (3-4), 199–210.

Quenette, S., Appelbe, B., Gurnis, M., Hodkinson, L., Moresi, L., Sunter, P., 2005. An investigation into design for performace and code maintainability in high performance computing. ANZIAM J. 46 (E), C101–C116.

Regenauer-Lieb, K., Yuen, D., 2004. Positive feedback of interacting ductile faults from coupling of equation of state, rheology and thermal-mechanics. Phys. Earth Planet. Int. 142 (1-2), 113–135.

Rudnicki, J., Rice, J., 1975. Conditions for the localization of deformation in pressure-sensitive dilatant materials. J. Mech. Phys. Solids. 23, 371–394.

Rutter, E., 1986. On the nomenclature of model of failure transitions in rocks. Tectonophysics 122, 381–387.

Sandwell, D., 1986. Thermal stress and the spacings of transform faults. J. Geophys. Res. 91 (B6), 6405–6417.

Sandwell, D., Fialko, Y., 2004. Warping and cracking of the Pacific plate by thermal contraction. J. Geophys. Res. 109 (B10411), doi:10.1029/2004JB003091.

Sandwell, D. T., Smith, W. H. F., 1997. Marine gravity anomaly from Geosat and ERS 1 satellite altimetry. J. Geophys. Res. 102, 10,039–10,054.

Shaw, W., Lin, J., 1996. Models of ocean ridge lithospheric deformation: Dependence on crustal thickness, spreading rate, and segmentation. J. Geophys. Res. 101 (B8), 17,977–17,993.

Simo, J., Hughes, T., 2004. Computational Inelasticity. Springer, New York.

Smallwood, J., White, R., 1998. Crustal accretion at the Reykjanes Ridge, 61°-62°N. J. Geophys. Res. 103, 5185–5201.

Tolstoy, M., Harding, A., Orcutt, J., Phipps Morgan, J., 1995. Crustal thickness at the Australian-Antarctic discordance and neighboring Southeast Indian Ridge. Eos Trans. AGU 76 (46), Fall Meet. Suppl., F570.

Turcotte, D., 1974. Are transform faults thermal contraction cracks? J. Geophys. Res. 79 (17), 2573–2577.

Vermeer, P., 1990. The orientation of shear bands in biaxial tests. Géotechnique 40, 223–236.

Weissel, J. K., Hayes, D. E., 1974. The Australian-Antarctic Discordance: New results and implications. J. Geophys. Res. 79, 2579–2587.

Wessel, P., 1992. Thermal stresses and the bimodal distribution of elastic thickness estimates of the oceanic lithosphere. J. Geophys. Res. 97, 14,177–14,193.

White, R., McKenzie, D., O'nions, R., 1992. Oceanic crustal thickness from seismic measurements and rare earth element inversions. J. Geophys. Res. 97 (B13), 19,683–19,715.

Chapter 4

Thermomechanics of mid-ocean ridge segmentation[1]

4.1 Abstract

The mechanics responsible for the initiation of the orthogonal pattern characterizing mid-ocean ridges and transform faults are studied using numerical models. The driving forces are thermal stresses arising from the cooling of young oceanic crust and extensional kinematic boundary conditions. Thermal stress can exert ridge-parallel tension comparable to spreading-induced stress when selectively released by ridges and ridge-parallel structure. Two modes of ridge segment growth have been identified in plan view: An overlapping mode where ridge segments overlap and bend toward each other and a connecting mode where two ridge segments are connected by a transform-like fault. As the ratio of thermal stress to spreading-induced stress (γ) increases, the patterns of localized plastic strain change from the overlapping to connecting mode. The orthogonal pattern marks the transition from one mode to the other. Besides the amount of stress from each driving force, the rate of stress accumulation is crucial in determining the emergent pattern. This rate-dependence is characterized by the spreading rate normalized by a reference-cooling rate (Pe'). When Pe' is paired with the ratio of thermal stress to spreading-induced stresses (γ'), they define stability fields of the two modes. The obliquely connecting, the or-

[1]Accepted for publication in *Physics of Earth and Planetary Interior*, 2008.

thogonally connecting, and the overlapping mode are similar to ridge-transform fault intersections observed in ultraslow, slow to intermediate, and fast spreading centers, respectively. The patterns are also sensitive to the strain weakening rate. Fracture zones were created in part as a response to thermal stress.

4.2 Introduction

Mid-ocean ridges and transform faults intersect to make various patterns, one being the idealized orthogonal pattern prominently characterizing plate boundaries. However, the processes responsible for the emergence and stability of such patterns remain poorly understood. Mid-ocean ridges are a hierarchical system of discontinuous ridge segments offset by different types of discontinuities (Macdonald et al., 1991). Segmentation at different scales has invited multiple theories for their origin (e.g., Macdonald et al., 1991; Phipps Morgan, 1991; Abelson and Agnon, 1997). It remains unclear whether the hierarchy is the product of different mechanisms working at different scales or the scale-dependence of a single mechanism. While the overall trend of mid-ocean ridges is imposed by the geometry of continental breakup and passive margin formation, the geometric coincidence between passive margins and mid-ocean ridges led Wilson (1965) to first propose that transform faults are inherited from preexisting structures. Subsequent studies proposed that stepping half-grabens (e.g., Cochran and Martinez, 1988; McClay and Khalil, 1998), segmented gravity and magnetic anomalies (e.g., Behn and Lin, 2000), or segmented weak regions (e.g., Watts and Stewart, 1998) along passive margins ultimately lead to the discontinuities found along mid-ocean ridges. However, other observations support the hypothesis that the orthogonal ridge-transform system is emergent and not solely due to preexisting conditions. Sandwell (1986) presented three lines of evidence supporting this hypothesis:1) that single straight ridges can develop into an orthogonal pattern, 2) the existence of zero offset fracture zones, and 3) a positive correlation between ridge segment length and spreading rate.

Differences in the rate of energy dissipation between ridge segments and trans-

form faults have been suggested to lead to the orthogonal pattern (Lachenbruch, 1973; Froidevaux, 1973). According to this theory, energy dissipation can be more efficient at a spreading center than a transform fault and, as a result, the minimized ridge segment length by an orthogonal pattern results in the least energy dissipation. However, it was subsequently shown that the orthogonal pattern could be created without assuming higher energy dissipation at the spreading centers (Oldenburg and Brune, 1975). Atwater and MacDonald (1977) also questioned the validity of the minimum energy dissipation argument based on inconsistency with observations.

The observation of the oblique fabric of normal faults around ridge-transform fault intersections is such that they must result from both a ridge normal and a ridge parallel component of stress (Gudmundsson, 1995). Gudmundsson (1995) proposed the expansion of a plate's perimeter as an origin of ridge-parallel tension. However, Gudmundsson's hypothesis does not address the possibility that each ridge segment can grow instead of forming fracture zones, and the observed fabric often requires a low degree of mechanical coupling across transform faults and the associated shear stresses (e.g., Fujita and Sleep, 1978; Fox and Gallo, 1984; Grindlay and Fox, 1993; Behn et al., 2002). Also, changes in the direction of plate motion were suggested to lead to the development of the orthogonal pattern (Menard and Atwater, 1969), but this mechanism is not sufficiently general to explain most present mid-ocean ridge systems where changes in plate direction have been limited. A more plausible source for ridge-parallel tension is the cooling of oceanic lithosphere. Thermal cooling stresses make a significant contribution to the stress state of oceanic plates. Heuristic calculations (Collette, 1974), a calculation based on a plate cooling model (Turcotte, 1974; Sandwell, 1986), the presence of near-ridge seismicity (Wiens and Stein, 1984; Bergman and Solomon, 1984), and geoid anomalies over fracture zones (Parmentier and Haxby, 1986; Haxby and Parmentier, 1988) all indicate that thermal stresses can contribute significantly to a ridge parallel component of stress. Thermal stresses are isotropic, but mid-ocean ridges themselves and numerous ridge parallel faults can release thermal stresses in a selective (i.e., ridge-perpendicular) direction when these structures form (Fig.4.1). Therefore, the resultant unreleased stress due to cooling

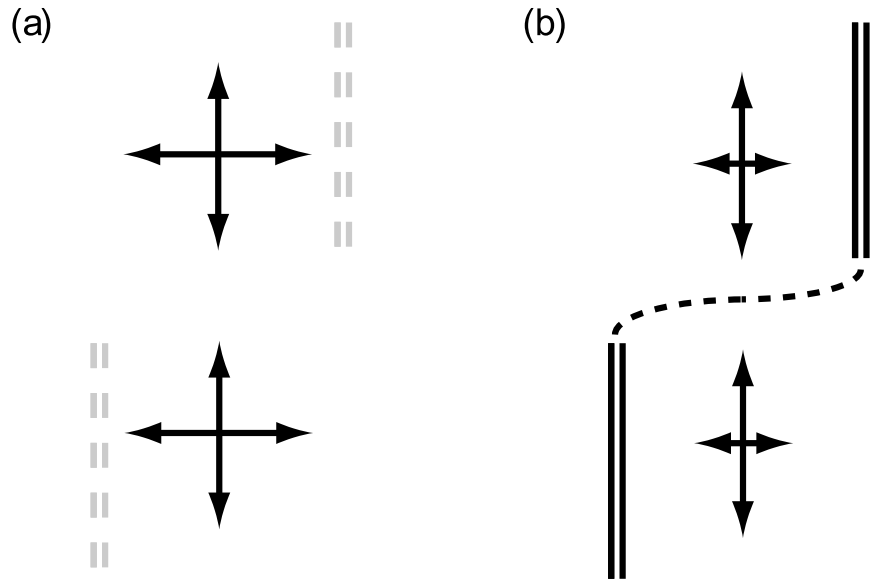

Figure 4.1: Ridge segments and other ridge-parallel structures can release thermal stress in the ridge-normal direction, while leaving ridge-parallel residual stresses. Arrows represent the direction and the magnitude of components of thermal stresses aligned along ridge-perpendicular and ridge-parallel directions. (a) Before ridge segments are created, thermal stress is isotropic and its horizontal components are equal in magnitude. The future location of ridge segments are marked by the pairs of gray dashed lines. (b) The ridge-parallel component becomes dominant when the ridge-normal principal stress is released by the formation of ridge segments (pairs of solid lines). A possible trace of a structure connecting the ridge segments is denoted by a dashed curve.

would be dominated by the ridge-parallel component.

Analog experiments using paraffin wax have been more successful than others in studying the emergence of patterns similar to those found at mid-ocean ridges. Oldenburg and Brune (1972) designed an experiment in which the surface of molten wax was chilled by a fan. The basin containing the molten wax was heated from below. One side of the solidified wax is pulled to generate extensional stresses. They observed the spontaneous growth of an orthogonal system of ridge, transform faults, and fracture zones with characteristics similar to natural systems. They concluded that the orthogonal ridge-transform fault system is a preferred mode of plate separation and that a weak shear resistance on transform faults is required for the system's stability (Oldenburg and Brune, 1975). Based on the high volume change of cooling wax, Sandwell (1986) interpreted that orthogonally intersecting structures made in

wax originated as a mechanism to release thermal stress. Wax was also used to study the microplate formation in a fast-spreading environment (Katz et al., 2005).

The success of the wax models implies that the orthogonal pattern of ridges and transform faults are caused by a combination of spreading and thermal stresses. However, to more fully understand the physics while adding additional processes critical for mid-ocean ridges, we turn to a numerical approach. In numerical simulations, known representative values for the Earth's material can be directly used in models. In addition, numerical experiments allow for a better control on testable mechanisms and a wide range of parameter values. Numerical models can also be used to make explicit predictions of geophysical observables such as bathymetry and gravity.

Our goal is to reveal the mechanism responsible for the emergence of the orthogonal pattern at mid-ocean ridges using a 3-D numerical method. Our approach is distinguished from previous 3-D numerical models for the mid-ocean ridge system that treated transform faults as pre-existing structures or as boundary conditions (e.g., Parmentier and Phipps Morgan, 1990; Furlong et al., 2001). In our study, transform faults and fracture zones, as well as ridge segments are all created as a response of a mechanical system to given initial and boundary conditions. A 2-D elastic damage model has been developed (Hieronymus, 2004), but differed from ours in terms of geometry, material properties, and the physical processes incorporated. We focus our attention on the first order segments and discontinuities, corresponding to ridge segments and transform faults, respectively (Macdonald et al., 1991).

4.3 Numerical method

We use SNAC, an explicit Lagrangian finite difference code, to model the dynamics associated with the initiation of ridge-transform fault systems in three dimensions. SNAC is a framework-based software, using the energy-based finite difference method to solve the force balance equation for elasto-visco-plastic materials (Bathe, 1996). The details of the algorithm are presented in Appendix A.

Implementing the elasto-visco-plastic material type in SNAC is crucial because

localization of plastic strain occurring due to bifurcation inherent to plasticity can be regarded as a large-scale manifestation of localized deformation like fault zones. Propagating ridge segments, transform faults, and fracture zones are all represented by localized plastic strain. In addition, a vertical gradient of temperature determines the transition from cold plastic material near the top to hot Maxwell viscoelastic material below.

Cooling of newly formed lithosphere is one of the key phenomena for modeling the mid-ocean ridge system. SNAC computes thermal diffusion using the same type of solver as the solution of the momentum equation. Temporal variation of the temperature field contributes to the isotropic components of stress through thermal expansion and contraction.

We use an elasto-visco-plasticity (EVP) model in which total strain is the sum of contributions from elastic, viscous, and plastic components (e.g., Albert et al., 2000). This material model assumes a Maxwell viscoelastic rheology at all times, but if the stress exceeds a specified criterion before being relaxed then yielding occurs. We use a Mohr-Coulomb yield criterion and a power-law viscosity (Lavier and Buck, 2002). The EVP constitutive relations allow a wide range of material behavior to emerge: Elastoplastic when temperature is low and viscoelastic at high temperatures. To induce localization, a strain-weakening rule is applied to the yield criteria. The rule is usually a piecewise linear function of accumulated plastic strain such that the plastic material properties (cohesion and angle of internal friction) decrease with increasing plastic strain (Lavier et al., 2000). In addition, elements are assigned initial finite plastic strain so that localization initiates from those elements. In this way, we can prevent the occurrence of localized plastic deformation adjacent to the boundary of the computational domain.

4.4 Model setup

We model a hot block of oceanic lithosphere that cools while it is stretched at a given spreading rate. Spreading initiates ridge segments, which in turn releases accumulat-

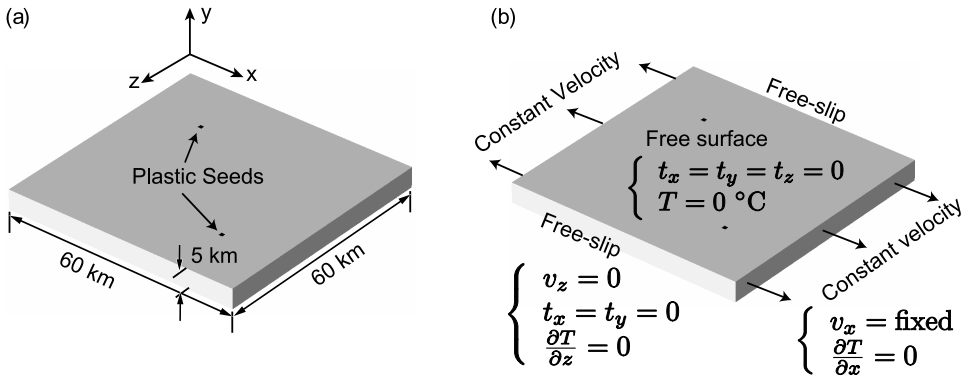

Figure 4.2: Geometry of the model domain. (a) 60×5×60 km domain with equal 1 km grid spacing in each direction. Two plastic seeds, controlling initial localization, are embedded with 30 km separation in the x and z directions. (b) Two side surfaces normal to the x axis are pulled at a constant velocity. The other two sides, normal to the z axis, have free-slip boundary conditions, where the normal velocity (v_z) and tangential components of traction (t_x and t_y) are 0. Zero heat flux is assumed for all the side walls, but the top surface temperature is fixed at 0 °C. See the text for thermal and mechanical boundary conditions for the bottom surface.

ing thermal stress only in the ridge-normal direction. The ensuing process is governed by given parameters and boundary conditions.

The domain is 60×5×60 km and is discretized into 1-km cubic elements (Fig.4.2a). Initial temperature is uniformly 1300 °C except along the top surface, where temperature is 0 °C. The top surface remains isothermal at 0 °C, while the bottom surface has a composite boundary condition. By the zero heat flux condition, heat is lost until the bottom temperature decreases to 750 °C; thereafter the bottom temperature is kept at 750 °C. These thermal initial and boundary conditions are intended to be those of hypothetically pristine oceanic lithosphere that is about to cool and extend. Heat fluxes are zero on all the side walls. We assume that the distinctive thermal structure of slow and fast mature ridges result from long-term spreading, not given initially. In reality, the thickness of lithosphere is not constant over the distance of 60 km across a spreading center. However, we assumed it to be initially uniform in order to exclude the influence of pre-existing structures. If the variation in lithospheric thickness is predefined, so would the pattern we seek because the thinnest part will develop into spreading centers unless other perturbations are considered.

Velocity boundary conditions are applied to two sidewalls while the other two are free-slip (Fig.4.2b). The bottom surface was supported by a frictionless denser foundation called a Winkler foundation (e.g., see p. 95 in Watts, 2001). This bottom boundary condition works in such a way that normal tractions are applied in the opposite direction to the deflection of the bottom surface and with a magnitude given by the surface integral of pressure change, $(\rho_m - \rho_f)g\Delta h(x)$, where ρ_m is the mantle density at the bottom of the domain, ρ_f is the assumed density of the foundation, g is the gravitational acceleration, and $\Delta h(x)$ is the change in the vertical coordinates at location x. For simplicity, we assume $(\rho_m - \rho_f)$ is fixed at 50 km/m^3. The two tangential components of traction are set to be zero.

Two ridge segments develop as narrow regions of localized strain. Strain localization initiates from two seeds, elements with non-zero plastic strain and offset by 30 km in both horizontal directions (Fig.4.2a). In addition, we assumed a piecewise linear function in strain weakening such that 100 MPa of cohesion is reduced to 50 MPa at 1 % plastic strain, and to 10 MPa at 3 %. All the plastic parameters (cohesion, internal friction angle, and dilation angle) are kept the same after plastic strain grows larger than 3 %. Unfortunately, strain weakening is poorly constrained by geological observations (Scholz, 2002; Lavier et al., 2000). Parameters related to the constitutive law are listed in Table 4.1.

4.4.1 Base model and its variations

One model is referred to as the base case and produced a nearly orthogonal transform fault that connected ridge segments (Fig.4.3). The imposed constant spreading rates are equivalent to time-varying forces required to maintain the spreading rate (Lavier and Buck, 2002; Gurnis et al., 2004). The spreading-parallel component of this force (F_x), as a function of time, is useful for monitoring the change in the state of stress. F_x for the base case (Fig.4.3a) shows that the system was initially in equilibrium with 1.22×10^9 N/m of external force remaining invariant for about 7000 yrs. The pattern of localization was determined during this phase, and it was not affected by

Table 4.1: Parameter values

Model	v (cm/yr)	α_v ($\times 10^{-5}\mathrm{K}^{-1}$)	κ ($\times 10^{-6}\mathrm{m}^2/\mathrm{s}$)	$\epsilon_{ps,1}$	C_1 (MPa)	$\epsilon_{ps,2}$
base	3	6	1.12	0.01	50.00	0.03
1	1	6	1.12	0.01	50.00	0.03
2	10	6	1.12	0.01	50.00	0.03
3	3	5.49	1.12	0.01	50.00	0.03
4	3	6.51	1.12	0.01	50.00	0.03
5	3	6	0.915	0.01	50.00	0.03
6	3	6	1.36	0.01	50.00	0.03
7	2	6	1.12	0.01	50.00	0.03
8	4	6	1.12	0.01	50.00	0.03
9	3	5.76	1.12	0.01	50.00	0.03
10	3	6.24	1.12	0.01	50.00	0.03
11	3	6	1.02	0.01	50.00	0.03
12	3	6	1.22	0.01	50.00	0.03
13	2.5	6	1.12	0.01	50.00	0.03
14	3.5	6	1.12	0.01	50.00	0.03
15	3	5.88	1.12	0.01	50.00	0.03
16	3	6.12	1.12	0.01	50.00	0.03
17	3	6	1.07	0.01	50.00	0.03
18	3	6	1.17	0.01	50.00	0.03
19	3.3	6.6	1.12	0.01	50.00	0.03
20	3.03	6.06	1.12	0.01	50.00	0.03
21	3.3	6	1.232	0.01	50.00	0.03
22	2.7	5.4	1.12	0.01	50.00	0.03
23	2.97	5.94	1.12	0.01	50.00	0.03
24	2.7	6	1.008	0.01	50.00	0.03
25	4.68	6.6	1.12	0.01	50.00	0.03
26	4	6.34	1.12	0.01	50.00	0.03
27	3.73	6.24	1.12	0.01	50.00	0.03
28	2.27	5.76	1.12	0.01	50.00	0.03
29	2	5.69	1.12	0.01	50.00	0.03
30	1.34	5.49	1.12	0.01	50.00	0.03
31	2.5	5.65	1.12	0.01	50.00	0.03
32	2.0	5.46	1.12	0.01	50.00	0.03
33	1.34	5.19	1.12	0.01	50.00	0.03
34	2.00	5.19	1.12	0.01	50.00	0.03
35	2.50	5.19	1.12	0.01	50.00	0.03
36	1.34	4.90	1.12	0.01	50.00	0.03
37	2.00	4.90	1.12	0.01	50.00	0.03
38	2.50	4.90	1.12	0.01	50.00	0.03
w1	3	6	1.12	0.01	50.00	0.02
w2	3	6	1.12	0.02	50.00	0.05
w3	3	6	1.12	0.01	25.00	0.03
w4	3	6	1.12	0.01	75.00	0.03
w5	3	6	1.12	0.01	50.00	0.03
w6	3	6	1.12	0.01	50.00	0.03
w7	3	6	1.12	0.01	43.75	0.03
w8	3	6	1.12	0.01	56.25	0.03

density = 2950 kg/m^3; Lame's constants (λ, μ) = 30 GPa, respectively;
$\epsilon_{ps,0} = 0$, C_0=100 MPa, C_2 = 10 MPa;
n=3, Q=380 kJ/mol, and A=1.73×10^5 (Pa·s)$^{1/n}$ for viscosity

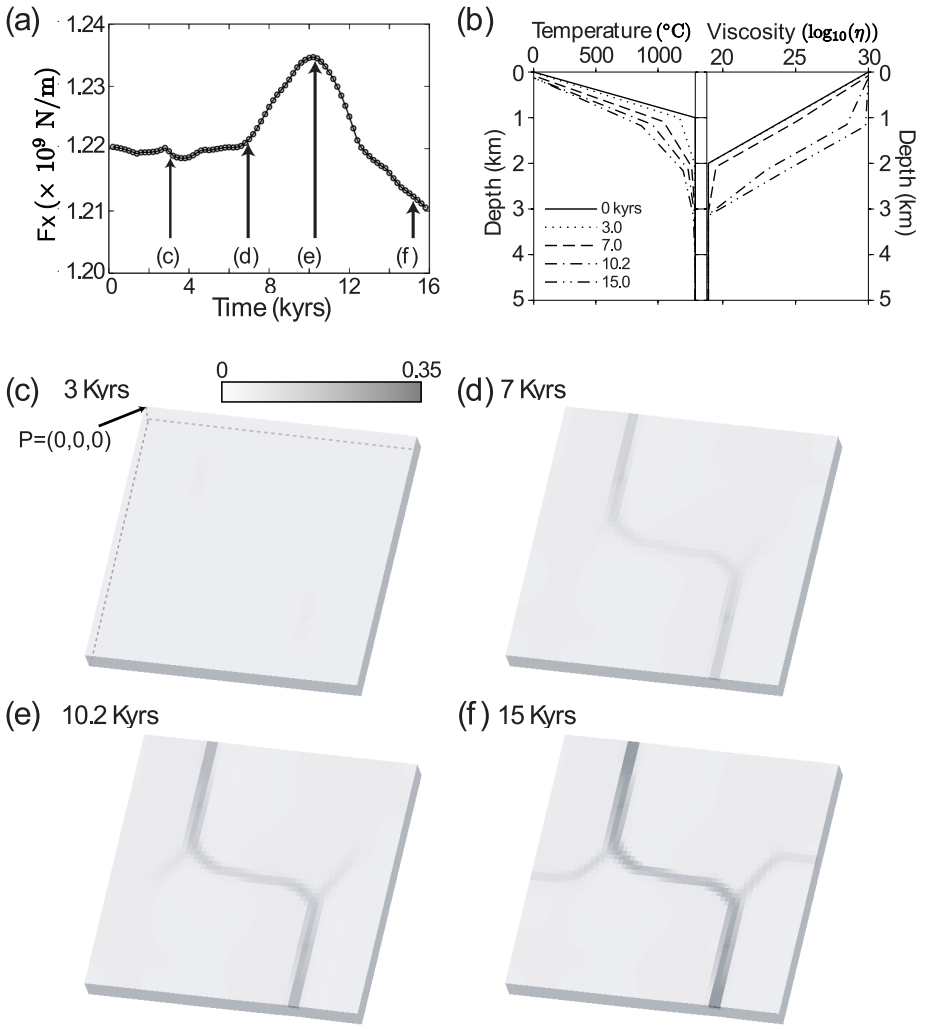

Figure 4.3: (a) F_x, force required to extend the domain at the applied velocity in the x-direction as a function of time. (b) Depth profiles of temperature and viscosity are taken at the point P marked in (a) and compared at different time steps (0, 3, 7, 10.2, and 15 Kyrs). The rise in F_x at ∼7 Kyrs coincides with the cooling and significant increase in viscosity of the subsurface (1-2 km deep) layer. 3-D rendering of the second invariant of plastic strain at the same set of time steps: (c) 3 Kyrs, (d) 7 Kyrs, (e) 10.2 Kyrs, and (f) 15 Kyrs.

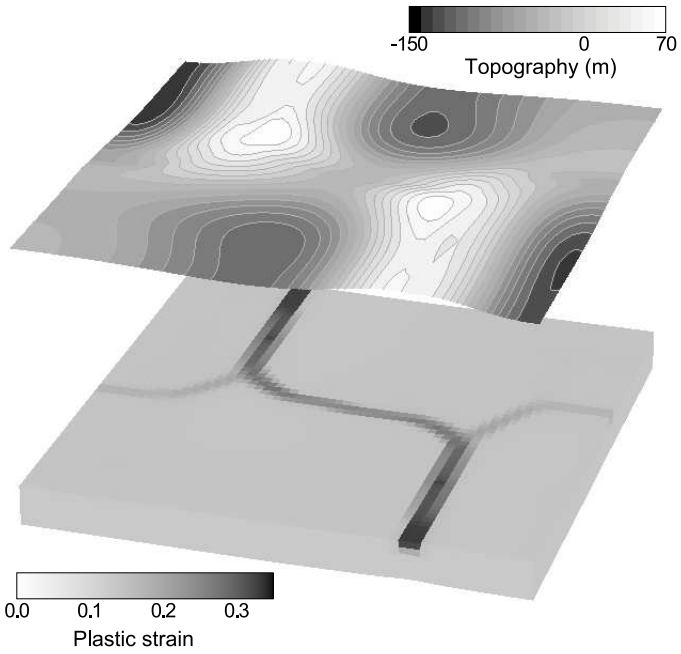

Figure 4.4: A 3-D representation of the surface topography from the base model at 15 Kyrs on top of the model domain. Plastic strain on the surface of the model domain indicated through grey scale shading.

subsequent deformation. When the subsurface layer cooled sufficiently, the exponentially increased temperature-dependent viscosity rendered the layer elastic and thus the overall stiffness of the model increased (Fig.4.3b). Consequently, F_x increases in response to this change after 7000 yrs in the F_x versus time plot. As deformation due to spreading and thermal stress continues, the cooled portions of the layer yield and become weaker beneath ridge segments (Fig.4.3e). This leads to the decrease of F_x (Fig.4.3a).

The total elapsed time, about 15 Kyrs, was insufficient to develop into the morphology seen at mature mid-ocean ridges, as shown with topography along with the deformed mesh and accumulated plastic strain (Fig.4.4). However, it shows the deepening trend of bathymetry away from ridge segments and troughs along ridge-normal localized bands, consistent with an actual ridge-transform fault intersection. The curvature of zones of localized strain at the inner corner is consistent with the fabric of structures observed at slow spreading ridge-transform fault intersections (Fox and Gallo, 1984).

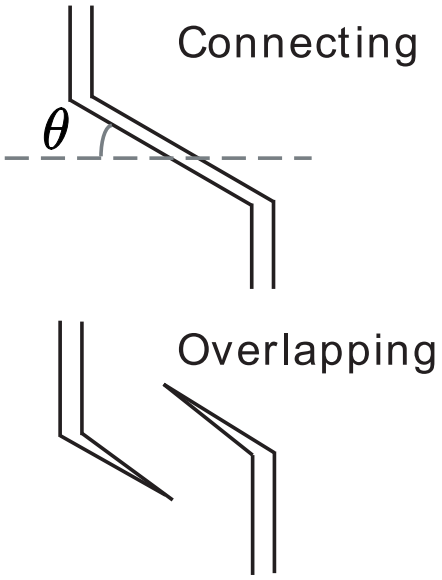

Figure 4.5: Modes of interaction between two mutually approaching ridge segments. The orthogonal ridge-transform fault geometry is a special case of the connecting mode. The angle, θ, is used as a measure of a connecting patterns orthogonality spanning the range 0° to 45°.

Models varied from the base case in terms of their pattern of localization. The patterns could be grouped based on their geometry into two modes: "Connecting" and "overlapping" (Fig.4.5). They are end members of the modes of interaction between two mutually-approaching ridge segments. Connecting modes are further characterized by the angle θ between the connecting segment and the ridge-normal direction; θ ranges from 0° to 45°, and the orthogonal pattern, corresponding to θ=0°, falls in the middle of the morphological range from high-θ connecting modes to overlapping modes.

To assess quantitatively the relative influence of thermal stress and spreading-induced stress on the appearance of localization patterns, we introduce a dimensionless number γ. γ is defined as the ratio of the first invariant of thermal stress to the first invariant of spreading-induced stress:

$$\gamma = \frac{|I_\sigma^{therm}|}{|I_\sigma^{spr}|}. \tag{4.1}$$

Spreading-induced stress is given by constitutive relations for linear isotropic elastic-

ity:

$$\sigma_{ij}^{spr} = \lambda\delta_{ij}\epsilon_{kk}^{spr} + 2\mu\epsilon_{ij}^{spr}, \tag{4.2}$$

where λ and μ are Lamé's constants. Thermal stress is given as (e.g., Boley and Weiner, 1960):

$$\sigma_{ij}^{therm} = -(3\lambda + 2\mu)\delta_{ij}\alpha_l(T - T_0), \tag{4.3}$$

where α_l is the linear thermal expansion coefficient, T is temperature, and T_0 is the reference temperature. When extension in one horizontal direction and zero-strain in the other two directions is assumed, extensional stresses are, from (4.2),

$$\begin{aligned}
\sigma_{11}^{spr} &= \lambda\left(\epsilon_{11}^{spr} + \epsilon_{22}^{spr} + \epsilon_{33}^{spr}\right) + 2\mu\epsilon_{11}^{spr} = (\lambda + 2\mu)\epsilon_{11}^{spr} \\
\sigma_{22}^{spr} &= \lambda\epsilon_{11}^{spr} \\
\sigma_{33}^{spr} &= \lambda\epsilon_{11}^{spr},
\end{aligned} \tag{4.4}$$

Then, the first invariant of spreading-induced stress becomes

$$I_{\sigma}^{spr} = \sigma_{11}^{spr} + \sigma_{22}^{spr} + \sigma_{33}^{spr} = (3\lambda + 2\mu)\epsilon_{11}^{spr}, \tag{4.5}$$

The first invariant of thermal stress is obtained from (4.3):

$$I_{\sigma}^{therm} = \sigma_{11}^{therm} + \sigma_{22}^{therm} + \sigma_{33}^{therm} = -(3\lambda + 2\mu)\alpha_v(T - T_0), \tag{4.6}$$

where α_v is the volumetric thermal expansion coefficient and is equal to $3\alpha_l$. Substituting (4.5) and (4.6) into (4.1) and taking the absolute value, we obtain

$$\begin{aligned}
\gamma &= \frac{|(3\lambda + 2\mu)\alpha_v(T - T_0)|}{|(3\lambda + 2\mu)\epsilon_{11}^{spr}|} = \frac{|\alpha_v(T - T_0)|}{\epsilon_{11}^{spr}} \\
&= \frac{|\alpha_v(\kappa\nabla^2 T)\Delta t|}{\dot{\epsilon}_{11}^{spr}\Delta t} \approx \frac{\alpha_v(\kappa\Delta T/D^2)}{\dot{\epsilon}_{11}^{spr}} \\
&= \frac{\kappa\alpha_v\Delta T}{\dot{\epsilon}_{11}^{spr}D^2},
\end{aligned} \tag{4.7}$$

where $\dot{\epsilon}_{11}^{spr}$ is the strain rate associated with a half-spreading rate, Δt is the charac-

teristic time of thermal diffusion, ΔT is the absolute temperature difference between surface and bottom, κ is the thermal diffusivity, D is the thickness of the domain. $\dot{\epsilon}_{11}^{spr}$ can be further approximated as v/L, where v is the half-spreading rate and L is the width of the domain:

$$\gamma = \frac{\kappa \alpha_v L \Delta T}{v D^2}. \tag{4.8}$$

When γ is defined as in (4.8), it represents the relative importance of conductive cooling with respect to spreading in determining the dominant state of stress for emergent oceanic lithosphere although it is not the stress ratio itself. Since the domain geometry (D and L) and the temperature initial condition (ΔT) are common to all the models, we vary the remaining three parameters, v, α_v, and κ to determine their influence on the pattern of localization.

Another measure of the system is introduced because the same value of γ can be achieved by different values of parameters that are varied in the same proportion. Those models with the same γ but different parameters can produce considerably different patterns because the growth rates of stresses from cooling and spreading are different even for the proportionally varied parameters. The absolute value of rates is important because the material strength governed by plasticity is finite. So, we use the Peclet number as another measure of the system which we physically interpret here as the ratio of forced spreading rate (v) to cooling rate (κ/D). To ensure that separate measures of each process are not inherently correlated by sharing common parameters, we compute them with respect to reference values of v and κ/D. Thus, a pair of non-dimensional numbers, and γ' and Pe', are defined as

$$\gamma' = \frac{\kappa \alpha_v L \Delta T}{v_{ref} D^2}, \tag{4.9}$$

$$Pe' = \frac{v D_{ref}}{\kappa_{ref}}, \tag{4.10}$$

where v_{ref} is 3 cm/yr, κ_{ref} is 10^{-6} m^2/sec, and D_{ref} is 5 km.

Strain weakening during plastic deformation is characterized by a reduction in cohesion, $C(\epsilon_{ps})$, as plastic strain (ϵ_{ps}) accumulates. We define a dimensionless number,

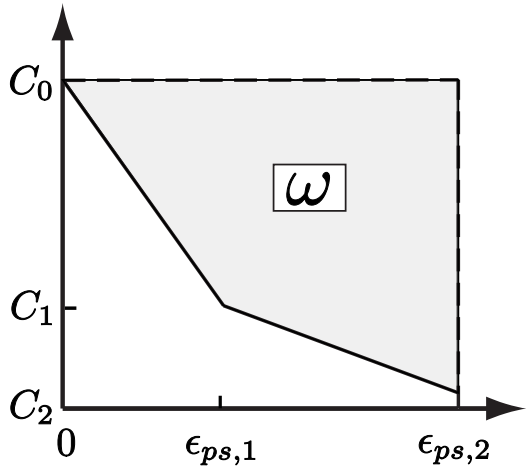

Figure 4.6: The piecewise linear variation of cohesion as a function of accumulated plastic strain (ϵ_{ps}). Two-stage weakening was assumed in this study. ω, the work per unit volume done to reduce 90 % of the initial cohesion, is used to quantify different weakening rules. C_0 and C_2 are 100 MPa and 10 MPa, respectively, for all the models.

ω, as follows:

$$\omega = 1.0 - \frac{\int C(\epsilon_{ps}) d\epsilon_{ps}}{C_{ref}\epsilon_{ps,2}^{ref}}, \tag{4.11}$$

where C_{ref} is a reference value of cohesion, and $\epsilon_{ps,2}^{ref}$ is a reference value of accumulated plastic strain where cohesion becomes 10 % of its initial value (Fig.4.6). C_{ref} and $\epsilon_{ps,2}^{ref}$ are 100 MPa and 3 %, respectively. ω is proportional to the normalized work per unit volume done to reduce cohesion until plastic strain reaches a given value, $\epsilon_{ps,2}$. In this study, the initial value of cohesion (C_0) and $\epsilon_{ps,2}$ are always equal to C_{ref} and $\epsilon_{ps,2}^{ref}$. If ω is higher than the base model, then more work would have been done to reduce cohesion; such a model ends up with lower cohesion even with the same amount of accumulated plastic strain. Table 4.1 lists values of all model parameters.

4.5 Results

We group models either with different γ and the same weakening rates (base case to model 38 in Table 4.1) or models with the same γ but different strain weakening rules (W1 to W8).

4.5.1 Variation of γ

Using a subset of models with the same weakening rate (base case to model 38 in Table 4.1), localization patterns show a clear trend in the modes of interaction between ridge segments when arranged in order of increasing γ (Fig.4.7). Patterns corresponding to relatively high γ (> 0.24) are those of oblique spreading ridges. For the highest γ, corresponding to the strongest influence of thermal stress, two propagating segments are connected by a 45°-oblique ridge segment. θ decreases as γ becomes smaller and thus the spreading-induced stress becomes stronger. Eventually, a nearly orthogonal pattern emerges within a narrow range of γ, from 0.22 to 0.23. When γ becomes smaller than 0.22, two ridge segments grow, overlap, and then bend toward each other. When the spreading-induced stress becomes even stronger ($\gamma < 0.1$), each segment propagates through the domain instead of bending or being connected by a shear band. The same trend is observed in both results after a constant time (Fig.4.7a) or after constant extension (Fig.4.7b).

When the force associated with spreading is plotted as a function of extension, we find two clearly divided populations of curves that correspond to the connecting and overlapping modes (Fig.4.8). In terms of the rise time of F_x, the base model falls on the boundary between these two groups. The differences in the shape of the curves in Fig.4.8 can be quantified when the curves are integrated over their extended distance. The portion of the F_x curves after the peak does not exhibit a clear distinction between modes as before the peaks; consequently, we integrate F_x from 0 to the extension corresponding to the peak of F_x. The integrated values have units of work per unit length. When only one of the parameters v, α, or κ was varied from the base model, the work decreases with increasing γ (gray symbols, Fig.4.9). As γ decreases and the work increases, the angle between the connecting segment and the spreading direction (θ, Fig.4.5) decreases, marking the transition to the overlapping mode at its minimum. Among models in the overlapping-mode, the correlation between work or γ and θ is not as clear. When two parameters (v and α, or v and κ) are varied simultaneously, models do not show systematic variations in

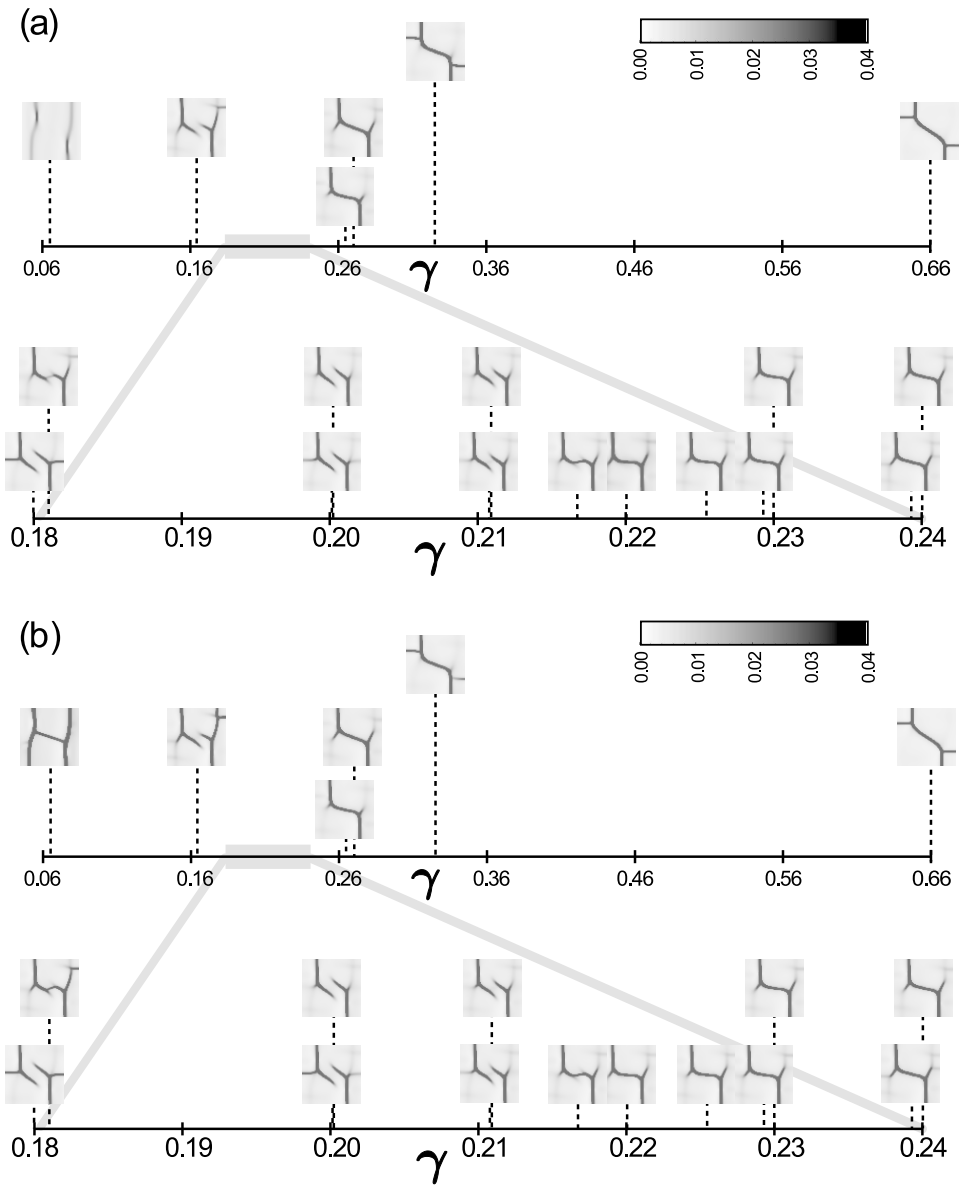

Figure 4.7: Patterns of localized plastic strain, made on the top surface of models, are arranged in order of increasing γ. The patterns were captured (a) after 10.6 Kyrs and (b) after a given amount of spreading-induced strain, 0.535 %. As γ increases, the mode of interaction between two mutually-approaching ridge segments changes from oblique rifting through orthogonal rifting to overlapping-bending.

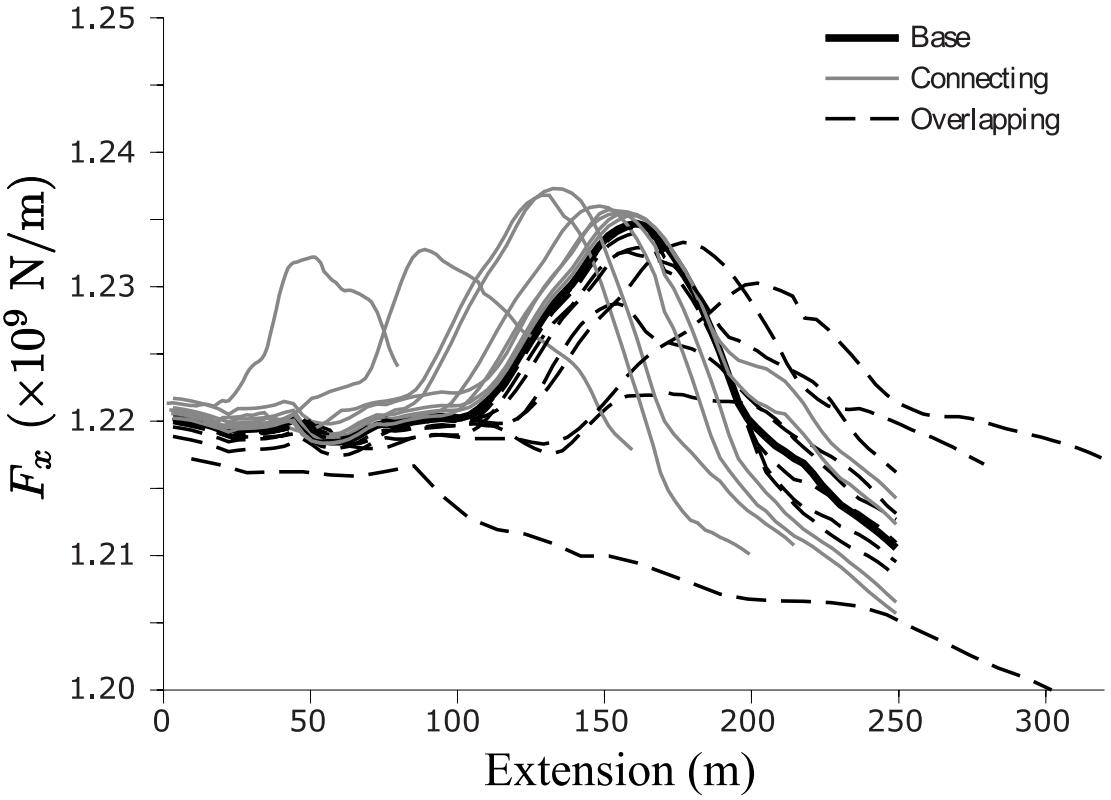

Figure 4.8: For various models, F_x as a function of amount of extension. The base model (thick solid line) forms a boundary between curves for models in connecting modes (thin gray solid lines) and those models exhibiting overlapping modes (thin dashed lines).

mode or θ (black symbols, Fig.4.9). Modes and the values of $\theta$are mixed in the low-γ ranges. Thus, γ and work cannot uniquely predict the emerging pattern for all the models even though there is an obvious correlation.

The inability of predicting the emergent pattern is resolved when the Peclet number is considered as well, as shown when γ' is varied against Pe'. Since Pe' is a separate measure of the spreading rate with respect to a reference cooling rate, we are able to separate the two rate-dependent processes that are inherent in γ. All the models with the same weakening rate are plotted in Fig.4.10. In contrast to the previous work versus γ plots, here the domains of each mode can be clearly divided. The boundary between the two modes that define the orthogonal pattern can be roughly traced along a single curve. The variation in θ is also systematic within the connected-mode domain. For a given spreading rate (constant Pe'), θ increases

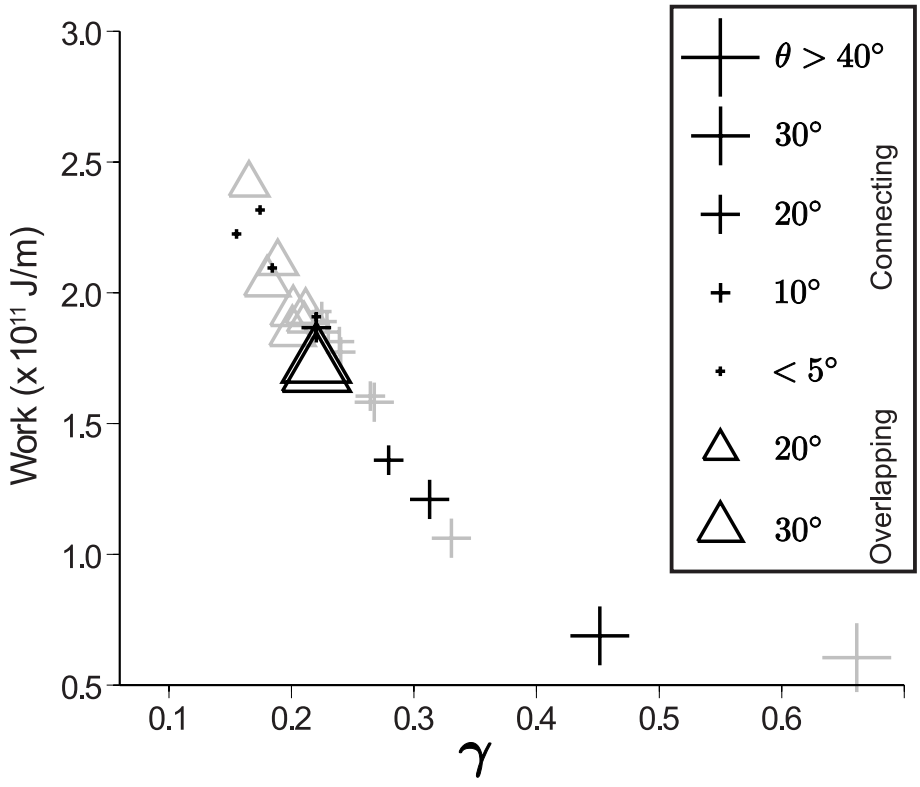

Figure 4.9: Work done by the external extension until the peak in F_x versus γ for models with a single parameter (v, α, or κ) varied from the base model (gray symbols) and those with two parameters varied simultaneously (either v and α, or v and κ, black symbols). Work and γ show an overall negative correlation. Models with connecting-mode patterns (crosses) show an approximately monotonic increase in θ as γ increases and work decreases. However, the modes of deformation and θ appear mixed in the low range of γ, indicating that γ and work cannot be unique indicators of emerging patterns. The overlapping-mode models (triangles) exhibit neither a broad variation in θ nor a one-to-one relation between work and γ.

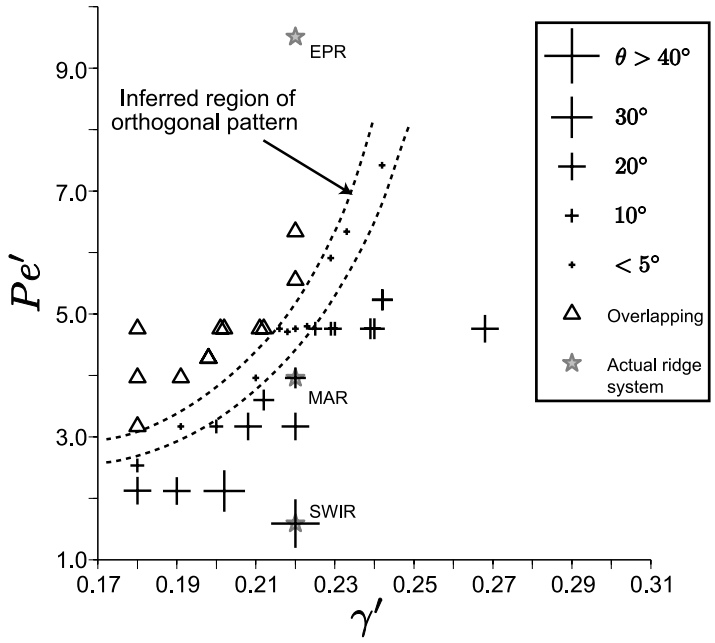

Figure 4.10: Plot of Pe' versus γ'. The domain of connecting and overlapping mode is well defined and the boundary between them defines the stability field of the orthogonal pattern. Within the connecting-mode domain, the variation in θ is systematic: θ becomes smaller as the values of Pe'-γ' pair gets closer to the inferred region of orthogonal pattern.

as thermal stress becomes dominant; for a given set of cooling-related parameters (constant γ'), θ increases as spreading becomes slower. The inferred stable region of orthogonal patterns suggests that when spreading rate is sufficiently small the overlapping mode is unable to form, regardless of γ'.

The transition from one faulting pattern to another occurred at specific values of Pe', which was confirmed by a suite of higher resolution models. We solved models on a mesh with half the horizontal grid spacing. The vertical resolution was not changed to maintain the same cooling rate with the original models and γ' was fixed at 0.202, the same value as the reference model. As Pe' increased from 1.585 (corresponding to the spreading rate, v=1 cm/yr) to 4.756 (v=3 cm/yr), models with the higher resolutions exhibited the same transition with the reference grid spacing from the obliquely connecting to the orthogonal pattern (Fig.4.11). The patterns varied from the orthogonal to overlapping when Pe' was further increased to 6.342 (v=4 cm/yr) (Fig.4.11), as also seen in the models with the reference resolution.

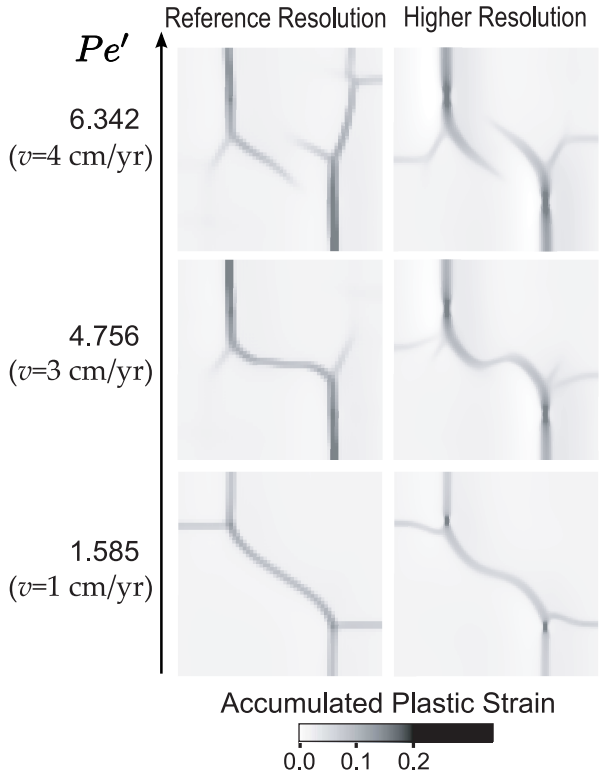

Figure 4.11: Models with a twice higher horizontal resolution than those in Fig.4.10. confirm that the transition of patterns occurs at consistent values of Pe'. The γ' of 0.202 was the same for all the compared models.

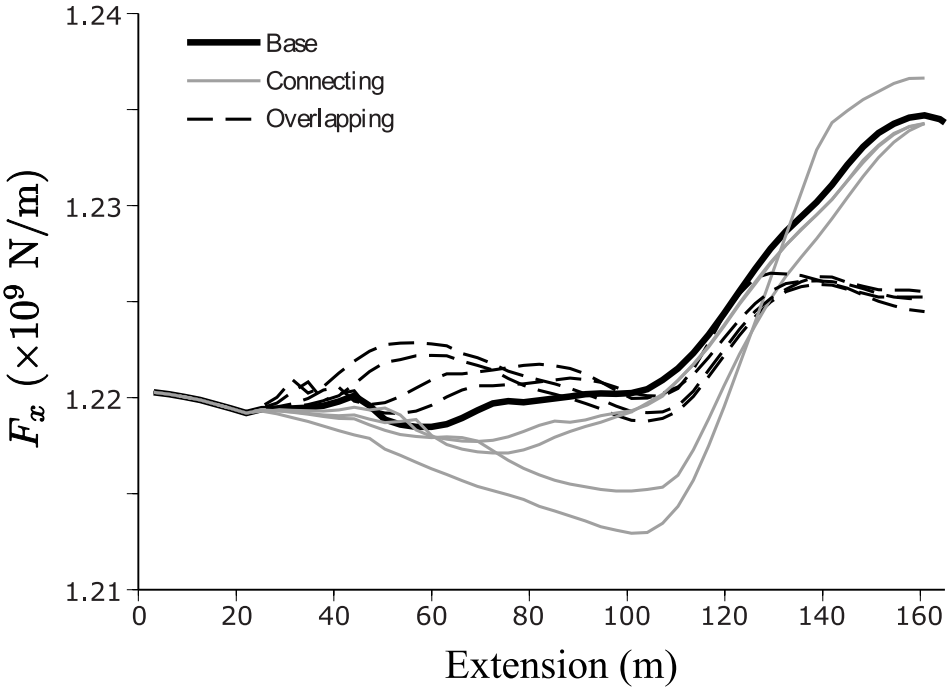

Figure 4.12: For models with different weakening rates F_x is plotted as a function of the amount of extension. Models that are relatively slower in weakening (thin gray lines) develop larger differences between the lowest and the highest value in F_x and connecting-mode patterns emerge from them. In contrast, faster-weakening models (dashed lines) showed smaller differences between the lowest and the highest F_x and developed overlapping-mode patterns. This solid line corresponds to the base model, which developed an orthogonal pattern.

4.5.2 Variation in rate of weakening

The rate of strain weakening is another pattern-controlling factor. The eight models (W1 to W8 in Table 4.1) share the two-stage weakening parameterization (Fig.4.6), but differ in the rate of cohesion reduction. F_x-extension curves for these eight models are shown in Fig.4.12. Models with higher ω (eqn. 4.11) consistently resulted in the overlapping patterns, while the connecting mode appeared in the models with lower ω. The map-view patterns from those models, taken after 10 Kyrs, are arranged in the order of increasing ω in Fig.4.13, demonstrating the sensitivity of pattern to ω.

ω represents the amount of cohesion reduced after strain weakening occurred. Since the first appearance of localization from the seed elements is ridge segments that propagate in the direction perpendicular to the spreading direction, different

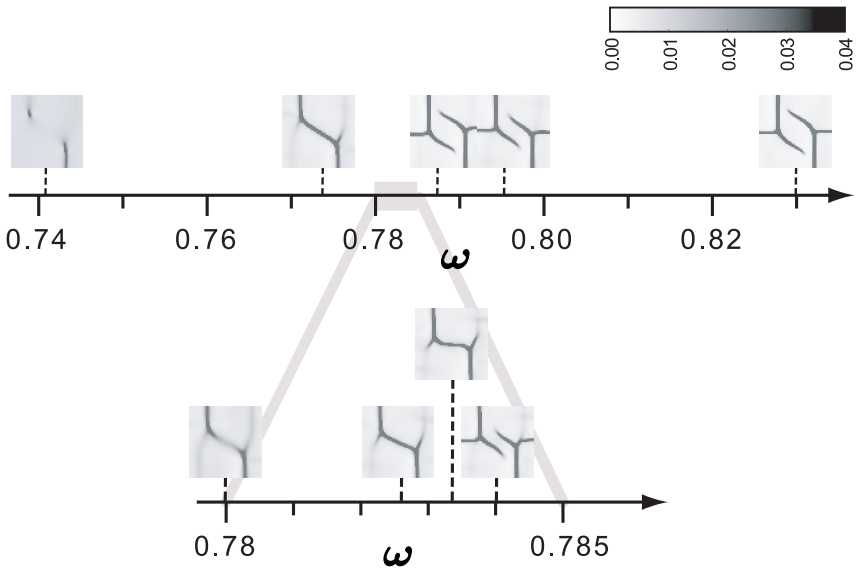

Figure 4.13: Patterns of localized plastic strain on the top surface are arranged in the increasing order of ω. The smaller ω is, the larger is the cohesion at any point in accumulated plastic strain as long as cohesion is larger than 10 % of its initial value (see Fig.4.6). Patterns show the transition of patterns from high-θ connecting modes through the orthogonal pattern to overlapping modes as ω increases.

values of ω have a prominent influence on that propagation. When a model has a higher ω while all other parameters remain the same compared to the base case, a lower level of cohesion is achieved and the propagation of ridge segments is facilitated. The net effect is equivalent to reducing γ by increasing the spreading rate, and the mode of interaction between two ridge segments becomes overlapping. In contrast, when a model has a lower value of ω while all other parameters remain the same as the base model, the model remains at a relatively high level of cohesion and ridge propagation is hindered. As a result, a high-θ connecting mode emerges because the net effect is to raise γ by lowering the spreading rate.

4.6 Discussion and conclusion

Our model results are in good agreement with observations: As spreading rate (v) increases while all other variables remain constant, γ decreases and the mode of ridge interaction changes from connecting to overlapping. Consistent with this trend,

orthogonal ridge-transform fault intersections are often found in the slow-spreading Mid-Atlantic Ridge (MAR). The overlapping mode of interaction would correspond to the formation of microplates, which are found only at the fastest spreading East Pacific Rise (EPR) (Naar and Hey, 1991). The large-θ connecting modes for the models at the lower end of Pe' appear to be relevant to the very-slow-spreading ridges (Dick et al., 2003). The Southwest Indian ridge (SWIR) between the Atlantis II and Gauss fracture zones, one of the very-slow-spreading oceanic ridges, shows a resemblance to the patterns of large-θ connecting mode seen in our low-γ models: Segments that are normal to the spreading direction alternate with oblique ones (see Fig.5a in Dick et al., 2003). According to Atwater and MacDonald (1977), observations show that slow spreading centers ($v < 3$ cm/yr) are oblique to transform faults in most cases; spreading centers with intermediate rates ($v \approx 3$ cm/yr) intersect transform faults both orthogonally and obliquely; only fast spreading centers ($v > 5$ cm/yr) are nearly orthogonal to transform faults. Thus, it is consistent with these observations that the slow-spreading Southwest Indian ridge falls in the high-θ connecting-mode domain of the Pe'-γ' plot, while the intermediate-spreading mid-Atlantic ridge corresponds to the relatively low-θ near the field of orthogonal patterns (Fig.4.10).

The deformation patterns found in the models are consistent with where actual ridge systems fall in the domain of Pe'-γ' (star symbols in Fig.4.10). Assuming the same thermal parameters with the base case, the γ' value remains the same with that of the base case, 0.22, while the half-spreading rate (v) determines the value of Pe' and thus the position on the plot. The SWIR with v=1 cm/yr is located well within the high-θ connecting-mode domain; the MAR, spreading at v=2.5 cm/yr, falls in the low-θ connecting-mode region, implying that slight variations in thermal state or spreading rate can yield both orthogonal and obliquely connecting patterns; and the fast-spreading EPR ($v > 10$ cm/yr) is in the overlapping-mode region.

It is possible that simplifications made in our model are the source of the discrepancy between modeling results and observations. For example, one of the factors that influence the localization pattern but was not addressed in this study is the offset between ridge segments. While observations on the newly formed oceanic basins sup-

port the discrete nucleation of spreading centers and their propagation as assumed in our model (e.g., Taylor et al., 1995), we did not take into account other characteristics inherited from the continental rifting phase. The size of our models is also fixed at the smallest possible for the first-order segmentation, and only the initial stage of pattern formation is considered. The mid-ocean ridge systems, however, exhibit a relatively wide range of ridge segment and transform fault lengths. They show a large amount of variability in the patterns of ridge-transform fault intersections, too. The EPR, for example, is dominated by overlapping segments but also has some orthogonal ones. The MAR has both orthogonal and oblique segments. The SWIR and the Gakkel ridge show the most striking variability implying that for the same spreading rate adjacent segments can be either orthogonal or oblique (M. Cannat, pers. comm.). However, it can be inferred from our model that segmentation is likely to be variable for one given spreading rate because factors such as magma supply rates, hydrothermal cooling and rheological properties are critical in determining the nature of segmentation and they are highly variable along axis as well as between mid-ocean ridge systems.

The assumed value of the volumetric thermal expansion coefficient (α_v) needs further justification. Typical values of v for rocks composing oceanic crust are 2 to 3×10^{-5} K^{-1} (Turcotte and Schubert, 2001), whereas we take 6×10^{-5} K^{-1} as a reference value. Volume change due to solidification is included in this larger value. Since oceanic crust was once melted and our initial temperature is well above the elastic temperature limit ($\sim$700 to 900 °C) (Reiter et al., 1987), we believe that it is essential to account for thermal stresses accumulated since the time of partial melt solidification, provided that newly-formed oceanic crust can retain at least a portion of those stresses. If the liquid-to-solid phase change is taken into account, a jump in density (inversely proportional to volume change in case of mass conservation) is expected at the moment of phase transition (e.g., Kushiro, 1980). Below the elastic temperature limit, α_v becomes close to the conventional value. Thus, the value of α_v we used can be thought of as an average over the entire cooling process. One of the waxes that easily created the orthogonal patterns (Oldenburg and Brune, 1975),

Shell Wax 200, is also characterized by a large density change from solidification and subsequent cooling (Sandwell, 1986).

Mantle upwelling patterns and their relation to along-axis segmentation have been studied extensively (e.g., Parmentier and Phipps Morgan, 1990; Shaw and Lin, 1996; Barnouin-Jha et al., 1997; Magde and Sparks, 1997; Choblet and Parmentier, 2001). However, the causal relation between them is not clear (Phipps Morgan, 1991). The time scale of mantle flow models is also significantly different from that of this study: It takes no longer than 10 Kyrs for the patterns of strain localization to emerge, while the time scale associated with mantle convection is typically on the order of million years. The segmentations were speculated to cause axial variations in mantle upwelling, not vice versa, because the patterns were made without the organized mantle upwelling in numerical experiments with an elastic damage model (Hieronymus, 2004). Our results support this point of view because the patterns were created without explicit consideration of mantle flow. Thus, we suggest that the patterns of ridge segments and transform faults are determined during the earliest period of spreading without substantial influence from mantle flow patterns. Later in time, the patterns are possibly modified by the change in plate motion, mantle upwelling, and magma supply.

Fracture zones were made in our models as a response to thermal stress. The thermal stress origin is consistent with previous analyses of thermal stress (Collette, 1974; Turcotte, 1974; Sandwell, 1986) and the role of ridge segments to release only the ridge-normal component of thermal stress assumed in this study. The orientation of their straight portion is parallel to the spreading direction as observed in mid-ocean ridge systems and wax experiments. The timing of fracture zone formation was always later than the emergence of patterns, which confirms the thermal origin of fracture zones because a sufficient amount of thermal stress alone would take longer to accumulate until yielding. Fracture zones were found to connect to the end of the non-connected branch of ridge segments rather than to extend in parallel from transform faults as most often found in the mid-ocean ridge systems (Fig.4.4).

Similar patterns were found to emerge from 2-D elastic damage models (Hierony-

mus, 2004). Comparable patterns included oblique 45°-connection (OC), transform fault (TF), and overlapping spreading centers (OSC). While keeping all other parameters the same as in their TF models, OCs require a stronger shear weakening due to distortional energy (defined as the double contraction of deviatoric stress and deviatoric strain tensors), while OSCs need a larger tensile strain as well as zero contribution to shear weakening from the distortional energy and the second invariant of deviatoric stress. The importance of the amount of tensile strain is comparable to our results: Larger applied strains correspond to faster spreading rates in terms of emergent patterns. Adjusting their damage properties roughly corresponds to varying our strain-weakening parameter, ω. However, the fundamental difference from our study is their emphasis on material properties rather than loading conditions. Although it was implied that different oceanic lithospheres are composed of inherently different materials, Hieronymus's study did not address the reason and processes responsible for such heterogeneity. On the contrary, we showed that the inclusion of thermal stresses is critical to determining the patterns in the mid-ocean ridge systems and that the differently loaded ridge systems can produce different patterns even for the same material properties. This allows our work to be more closely linked to the underlying physics as well as previous works which invoked thermal stress as the key driving force in mid-ocean ridge segmentation (Oldenburg and Brune, 1972, 1975; Collette, 1974; Turcotte, 1974; Sandwell, 1986). We note that rheology and loading, the two fundamental aspects of continuum mechanical problems, are not mutually exclusive. In the future it would be desirable to adopt an elasto-plasticity combined with damage.

In summary, we showed that selectively-released thermal stress can be a significant source of ridge-parallel tension. Numerical thermo-mechanical models showed that the resultant ridge-parallel tension from cooling and ridge-normal extension by far-field tectonic forces together create variation in the mode of interaction between two mutually-approaching ridge segments. The ratio of thermal stress to spreading-induced stress is a first-order measure of the mode that subsequently develops. When the rates of each driving process are measured separately, the models were clearly

divided into different modes of interaction. In general, the larger ratio of thermal stress to spreading-induced stress leads to the connecting mode, while the smaller ratio to the overlapping one. This correlation can translate to the observed correlation between the spreading rate and the modes of intersection between spreading centers and transforms faults. Magma-supply models have been successful in explaining the along-axis variability of mid-ocean ridge systems. Factors considered significant in those models such as magma supply rate and hydrothermal cooling eventually give rise to the local variations in thermal state. In that sense, our thermo-mechanical model would be complementary to such a long-term mode. A better understanding of the segmentation of the mid-ocean ridge systems would come from longer-term models that incorporate the continental rifting and magma supply models. In light of the high sensitivity of models to strain-weakening rates, it would be also crucial to use geologically-constrained plastic parameters.

References

Abelson, M., Agnon, A., 1997. Mechanics of oblique spreading and ridge segmentation. Earth Planet. Sci. Lett. 148 (3-4), 405–421.

Albert, R., Phillips, R., Dombard, A., Brown, C., 2000. A test of the validity of yield strength envelope with an elastoviscoplastic finite element model. Geophys. J. Int. 140, 399–409.

Atwater, T., MacDonald, K. C., 1977. Are spreading centres perpendicular to their transform faults? Nature 270 (5639), 715–719.

Barnouin-Jha, K., Parmentier, E., Sparks, D., 1997. Buoyant mantle upwelling and crustal production at oceanic spreading centers: On-axis segmentation and off-axis melting. J. Geophys. Res. 102 (B6), 11979–11989.

Bathe, K.-J., 1996. Finite Element Procedure. Prentice-Hall, Upper Saddle River, New Jersey.

Behn, M. D., Lin, J., 2000. Segmentation in gravity and magnetic anomalies along the U.S. east coast passive margin; implications for incipient structure of the oceanic lithosphere. J. Geophys. Res. 105 (11), 25,769–25,790.

Behn, M. D., Lin, J., Zuber, M. T., 2002. Evidence for weak oceanic transform faults. Geophys. Res. Lett. 29 (24), 2207, doi:10.1029/2002GL015612.

Bergman, E., Solomon, S., 1984. Source mechanisms of earthquakes near mid-ocean ridges from body waveform inversion: Implications for the early evolution of oceanic lithosphere. J. Geophys. Res. 89 (B13), 11415–11441.

Boley, B., Weiner, J., 1960. Theory of Thermal Stresses. Wiley, New York.

Choblet, G., Parmentier, E., 2001. Mantle upwelling and melting beneath slow spreading centers: Effects of variable rheology and melt productivity. Earth Planet. Sci. Lett. 184, 589–604.

Cochran, J. R., Martinez, F., 1988. Evidence from the northern Red Sea on the transition from continental to oceanic rifting. Tectonophysics 153 (1-4), 25–53.

Collette, B., 1974. Thermal contraction joints in a spreading seafloor as origin of fracture zones. Nature 251, 299–300.

Dick, H. J., Lin, J., Schouten, H., 2003. An ultraslow-spreading class of ocean ridge. Nature 426 (6965), 405–412.

Fox, P., Gallo, D., 1984. A tectonic model for ridge-transform-ridge plate boundaries: Implications for the structure of oceanic lithosphere. Tectonophysics 104, 205–242.

Froidevaux, C., 1973. Dissipation and geometric structure at spreading plate boundaries. Earth Planet. Sci. Lett. 20 (3), 419–424.

Fujita, K., Sleep, N. H., 1978. Membrane stresses near mid-ocean ridge-transform intersections. Tectonophysics 50 (2-3), 207–221.

Furlong, K., Sheaffer, S., Malservisi, R., 2001. Thermal-rheological controls on deformation within oceanic transforms. In: Holdsworth, R., Strachan, R., Magloughlin, J., Knipe, R. (Eds.), The Nature and Tectonic Significance of Fault Zone Weakening. Vol. 186. Geological Society, London, pp. 65–83.

Grindlay, N. R., Fox, P. J., 1993. Lithospheric stresses associated with nontransform offsets of the mid-Atlantic Ridge - Implications from a finite-element analysis. Tectonics 12 (4), 982–1003.

Gudmundsson, A., 1995. Stress fields associated with oceanic transform faults. Earth Planet. Sci. Lett. 136 (3-4), 603–614.

Gurnis, M., Hall, C., Lavier, L., 2004. Evolving force balance during incipient subduction. Geochem. Geophys. Geosyst. 5, Q07001, doi:10.1029/2003GC000681.

Haxby, W. F., Parmentier, E. M., 1988. Thermal contraction and the state of stress in the oceanic lithosphere. J. Geophys. Res. 93 (6), 6419–6429.

Hieronymus, C., 2004. Control on seafloor spreading geometries by stress- and strain-induced lithospheric weakening. Earth Planet. Sci. Lett. 222, 177–189.

Katz, R. F., Ragnarsson, R., Bodenschatz, E., 2005. Tectonic microplates in a wax model of sea-floor spreading. New J. Phys. 7 (37), doi:10.1088/1367–2630/7/1/037.

Kushiro, I., 1980. Viscosity, density, and structure of silicate melts at high pressures, and their petrological applications. In: Hargraves, R. B. (Ed.), Physics of Magmatic Processes. Princeton Univ. Press, Princeton.

Lachenbruch, A. H., 1973. A simple mechanical model for oceanic spreading center. J. Geophys. Res. 78 (17), 3395–3413.

Lavier, L. L., Buck, W., 2002. Half graben versus large-offset low-angle normal fault: Importance of keeping cool during normal faulting. J. Geophys. Res. 107 (B6, 2122), 10.1029/2001JB000513.

Lavier, L. L., Buck, W. R., Poliakov, A. N. B., 2000. Factors controlling normal fault offset in an ideal brittle layer. J. Geophys. Res. 105 (B10), 23,431–23,442.

Macdonald, K., Scheirer, D., Carbotte, S., 1991. Mid-ocean ridges: Discontinuities, segments and giant cracks. Science 253 (5023), 986–994.

Magde, L., Sparks, D., 1997. Three-dimensional mantle upwelling, melt generation, and melt migration beneath segment slow spreading ridges. J. Geophys. Res. 102 (B9), 20571–20583.

McClay, K., Khalil, S., 1998. Extensional hard linkages, eastern Gulf of Suez, Egypt. Geology 26 (6), 563–566.

Menard, H. W., Atwater, T., 1969. Origin of fracture zone topography. Nature 222 (5198), 1037–1040.

Naar, D. F., Hey, R. N., 1991. Tectonic evolution of the Easter microplate. J. Geophys. Res. 96 (5), 7961–7993.

Oldenburg, D., Brune, J., 1975. An explanation for the orthogonality of ocean ridges and transform faults. J. Geophys. Res. 80 (17), 2575–2585.

Oldenburg, D. W., Brune, J. N., 1972. Ridge transform fault spreading pattern in freezing wax. Science 178 (4058), 301–304.

Parmentier, E., Phipps Morgan, J., 1990. Spreading rate dependence of three-dimensional structure in oceanic spreading centres. Nature 348, 325–328.

Parmentier, E. M., Haxby, W. F., 1986. Thermal stresses in the oceanic lithosphere: Evidence from geoid anomalies at fracture zones. J. Geophys. Res. 91 (7), 7193–7204.

Phipps Morgan, J., 1991. Mid-ocean ridge dynamics - Observations and theory. Reviews of Geophysics Supplement 29, 807–822.

Reiter, M., Barroll, M. W., Minier, J., Clarkson, G., 1987. Thermo-mechanical model for incremental fracturing in cooling lava flows. Tectonophysics 142, 241–260.

Sandwell, D., 1986. Thermal stress and the spacings of transform faults. J. Geophys. Res. 91 (B6), 6405–6417.

Scholz, C. H., 2002. The Mechanics of Earthquakes and Faulting, 2nd Edition. Cambridge University Press.

Shaw, W., Lin, J., 1996. Models of ocean ridge lithospheric deformation: Dependence on crustal thickness, spreading rate, and segmentation. J. Geophys. Res. 101 (B8), 17,977–17,993.

Taylor, B., Goodliffe, A. M., Martinez, F., Hey, R. N., 1995. Continental rifting and initial sea-floor spreading in the Woodlark Basin. Nature 374 (6522), 534–537.

Turcotte, D., 1974. Are transform faults thermal contraction cracks? J. Geophys. Res. 79 (17), 2573–2577.

Turcotte, D. L., Schubert, G., 2001. Geodynamics, 2nd Edition. Cambridge University Press.

Watts, A. B., 2001. Isostasy and Flexure of the Lithosphere. Cambridge University Press.

Watts, A. B., Stewart, J., 1998. Gravity anomalies and segmentation of the continental margin offshore West Africa. Earth Planet. Sci. Lett. 156 (3-4), 239–252.

Wiens, D. A., Stein, S. A., 1984. Intraplate seismicity and stresses in young oceanic lithosphere. J. Geophys. Res. 89 (13), 11,442–11,464.

Wilson, J. T., 1965. A new class of faults and their bearing on continental drift. Nature 207 (4995), 343–347.

Chapter 5

Coupling models of crustal deformation and mantle convection with a computational framework[1]

5.1 Abstract

Crust and mantle exhibit contrasting compositions and thus distinct rheologies, making it challenging to model their combined mechanical behaviors. A code coupling technique is explored in order to solve multi-material and multi-physics problems. We adapt Pyre, a framework allowing distinct codes to exchange variables through shared interfaces, to the coupling of a Lagrangian and an Eulerian code. Motivated by computationally challenging problems like crust-mantle interaction, we couple an explicit code for the solution of crustal deformation for the mechanics of lithosphere with a finite element model for mantle dynamics, both in a spherical domain. The continuity of velocities and tractions and the no-slip conditions are imposed on the interfaces. The benchmarks against analytic solutions to the bending of a thin plate verifies that SNAC can give accurate solutions for the traction boundary conditions and that Pyre can correctly handle the crucial data exchanges. As a preliminary model in anticipation of more realistical problems, an elasto-visco-plastic lithosphere is coupled to a Newtonian viscous mantle. Flow in the mantle is driven by a hot

[1]Parts of this work were published by Eh Tan, Eun-seo Choi, Pururav Thoutireddy, Michael Gurnis, and Michael Aivazis in *Geochemistry, Geophysics, Geosystems*, 2006, 7, doi: 10.1029/2005GC001155.

sphere placed at the center of the mantle. This coupled model shows a steady growth of a dome in the lithosphere directly above the hot sphere, as expected. Unnecessarily high numerical cost is caused by the mismatch of time marching schemes adopted in each code.

5.2 Introduction

The dynamic coupling of the crust with the mantle on geological time-scales (such as those occurring on $>10^5$ yrs) is a long-standing problem that has been difficult to approach numerically. Together, the crust and mantle have a complex, composite rheology in which different layers and domains deform on vastly different time and spatial scales (e.g., Goetze and Evans, 1979; Kohlstedt et al., 1995; Ranalli, 1995). The mantle is usually treated as a linear (or non-linear) viscously dominated fluid with an infinite Prandtl number (the ratio of the diffusion of momentum to heat) (Davies, 1999; Schubert et al., 2001). The crust and upper lithosphere is commonly subdivided into several layers of elastic, elasto-plastic, and/or viscoelastic solids (e.g., Bodine et al., 1981; McNutt et al., 1988; Buck, 1991; Burov and Diament, 1995; Albert and Phillips, 2002). Modeling of geodynamics usually involves large displacements, rotation and strains and non-linearities such as brittle fracturing and non-linear viscoelastic creep (e.g., Lavier et al., 2000; Hall et al., 2003). In recent years the adoption of new numerical techniques (e.g., Cundall, 1989; Poliakov et al., 1993a; Fullsack, 1995; Beaumont et al., 2000; Hansen, 2003; O'Neill et al., 2006) has allowed for the modeling of a wide variety of problems related to deformation of lithosphere in 2-D and 3-D. These choices of non-linear rheologies to model the deformation of the mantle and crust as well on the widely different length scales of deformation, typically >10 km for the mantle and from a few meters (faults) to >100 km (long term elastic strength) for the lithosphere poses a vast challenge to numerical modeling of dynamics. The high resolution required for the solutions for 3D multi-scale phenomena leads to exorbitant numerical cost.

Various geophysical problems can be better addressed when the distinct rheolo-

gies of the crust and mantle are modeled as a composite system. For example, the initiation and the evolutionary processes of the Afar triple junction is the result of the mechanical interaction between the lithosphere and a mantle plume (e.g., Manighetti et al., 2001a,b). With a linear viscous rheology only, the transition from continental rifting to the formation of a mid-oceanic ridge through extension of the lithosphere cannot be properly modeled (e.g., Lavier and Manatschal, 2006). On the other hand, without the dynamic motion of the mantle, the time evolution of a triple junction cannot be realistically considered. A more complex example is the Cenozoic evolution of the Basin and Range Province in the western U.S. during which low angle normal faults accommodated extension occurring over a broad region (e.g., Wernicke, 1981). The Basin and Range Province is suggested to be extending under its own weight as well as due to contributions from other mantle-originated forces (e.g., Sonder and Jones, 1999, Chapter 2). The long-term deformation of such regions would be better simulated with a coupling between the mantle and the crust.

In this chapter, we explore the coupling of distinct numerical models as a potential option for such multi-material and multi-scale geodynamic problems. In particular, using facilities provided by Pyre (Tan et al., 2006), one mantle convection code is coupled with a code for modeling lithospheric deformation. We use a variation of CitcomS (**C**alifornia **I**nstitute of **T**echnology **CO**nvection **M**odel, **S**pherical) (Zhong et al., 2000) for mantle convection in a regional spherical cap (RegionalCitcomS hereafter). It is an Eulerian finite element program for solving the Stokes and energy equations and has been widely used for modeling mantle convection. SNAC (**S**tGermai**N** **A**nalysis of **C**ontinua) is used for lithospheric deformation. This code is based on the same algorithm for FLAC (**F**ast **L**agrangian **A**nalysis of **C**ontinua) and the code PARAVOZ developed by Y. Podlatchikov and A. Poliakov (e.g., Poliakov et al., 1993a) but has been extended to 3-D through a computational framework called StGermain (Quenette et al., 2005). SNAC uses an explicit scheme to acquire static or quasi-static equilibrium through a dynamic relaxation technique. Since SNAC can model various rheologies including plasticity, this code is well suited for the modeling of lithospheric deformation, such as those problems studied with the code PARAVOZ or

FLAC (Cundall, 1989; Poliakov et al., 1993a; Burov and Poliakov, 2001; Lavier and Buck, 2002; Hall et al., 2003; Buck et al., 2005). More theoretical background on SNAC is given in Appendix A. In Chapters 3 & 4 we give detailed applications to lithospheric deformation using SNAC without coupling.

5.3 Numerical method

5.3.1 SNAC: Overview

SNAC is a Lagrangian finite difference code for modeling a finitely deforming elasto-visco-plastic solid in 3-D. SNAC is very similar to a conventional finite element code with linear tetrahedral elements and thus shares many benefits with it. However, SNAC does not make explicit use of shape functions. For this reason, it is technically classified as a finite difference code. Another important characteristic of SNAC is that the dynamic relaxation technique is used to achieve static or quasi-static solutions from a dynamic momentum equation. This technique lets SNAC obtain solutions without solving a large matrix equation. A static finite element code whould typically involve inversion of a stiffness matrix and often suffers slow convergence when a non-linear constitutive law is adopted. Since the equation for heat energy balance can be optionally solved, SNAC can solve thermomechanical problems and have temperature-dependent rheologies. Although formulated in the small strain limit, long-term geodynamic problems eventually develop finite deformations. Two potential problems associated with large deformations acquired by accumulating small strains are the loss of objectiveness (the invariance under rotation (e.g. Rudnicki and Rice, 1975)) and the mesh distortion. To avoid these problems, SNAC updates stresses based on the objective Jaumann stress rate (e.g., Rudnicki and Rice, 1975) and performs remeshing when the mesh becomes too distorted.

5.3.2 StGermain framework

SNAC is built up from the StGermain framework, an environment for the development of numerically intense scientific codes (Quenette et al., 2005). As frameworks, StGermain and Pyre differ in that StGermain provides the infrastructural components needed to build complete codes while Pyre provides the superstructure to couple codes together; for this reason we refer to the former as an *infrastructure framework* and the latter as a *superstructure framework*.

StGermain provides a suite of libraries needed by general physical modeling software such as flow control, domain discretization, and initial/boundary condition management (Quenette et al., 2005). One of the advantages of using the StGermain framework is that a code can be easily extended through entry points and plug-ins. By adding or removing entry points, a problem-specific algorithm can be implemented while keeping the modification of source codes limited. Plug-ins are small pieces of codes that work as a part of the program, but can be compiled separately and dynamically loaded at run time. Thus, their development can be completely independent of the main program. For example, a new constitutive relation or time-varying boundary conditions can be made available as plug-ins without modifying or compiling the whole program that already exists.

5.4 Coupling through Pyre

We extend Pyre, a Python-based modeling framework that is originally developed to solve fluid structure interaction problems (Cummings et al., 2002). Technical details as well as an overview of Pyre have been published in (Tan et al., 2006). For completeness, however, we present the most relevant features of this framework and then describe under what physical principles the two solvers, RegionalCitcomS and SNAC, are coupled.

5.4.1 Overview of Pyre

Pyre is a full-featured, object-oriented environment that is capable of handling all aspects of the specification and launch of numerical investigations. Pyre operates on massively parallel supercomputers including both shared memory computers and Beowulf clusters. Pyre is written in the Python programming language, an open-source, well-maintained and widely used interpretive environment.

Pyre leverages the extensibility of the Python interpreter to allow for the seamless integration of rather diverse computational facilities. The framework provides enough flexibility to allow the dynamic discovery of available facilities as part of simulation staging. There is a well-defined and well-documented method by which a new solver or a new material model can be made available to the framework, while the flexibility allows the user to specify solvers and algorithms in the simulation script, without the need for recompilation or relinking. The combination promotes experimentation with new algorithms by lowering the overall overhead associated with trying out new approaches.

Each simulation model under Pyre is called an *Application*. An *Application* could contain one or more *Solvers*. An *Application* and its *Solver(s)* can run on multiple processors, but each processor has only one *Application* and one *Solver* on it (Fig.5.1). The role of the *Application* is to assign each processor a *Solver* and orchestrate the simulation staging of the *Solver(s)*, such as initialization (including memory allocation and variable assignment), time marching, and output (Tan et al., 2006).

5.4.2 *Coupler*

"Coupling" means running two spatially overlapping geophysical applications in such a way that interaction occurs through sharing physical quantities (such as velocity and traction) at interfaces. The sharing of information at an interface typically takes the form of sending and receiving data between two solvers and is managed by a *"Coupler"*.

The *Coupler* is one of the Pyre's classes that control the general procedure of

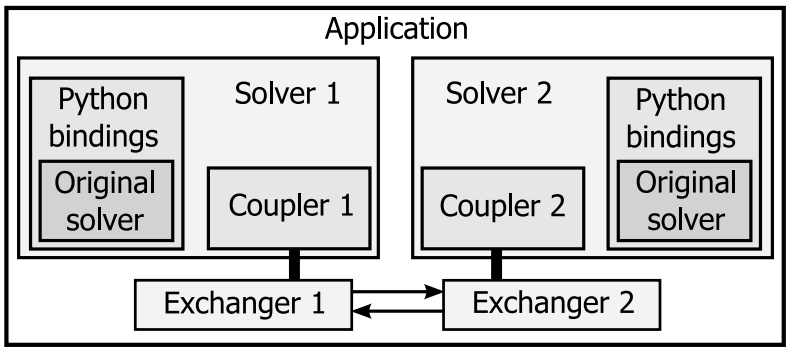

Figure 5.1: The architecture of a coupled *Application*. The *Application* has two *Solvers*. The original code of the solver (in C/C++/Fortran) is complied into a library, which is called by the Pyre *Solver* via the Python bindings. *Solver 1* is the containing solver and has a *Coupler 1*, and the other solver, *Solver 2*, has a *Coupler 2*. The *Couplers* communicate via the *Exchangers*, which are external to the *Solvers*.

coupling between elements in the Pyre. The *Coupler* controls only the top level of coupling, i.e., orchestrates the timing for sending and receiving information in the context of global time marching. The interaction details (for example, what quantities are exchanged and how received information will be used) vary with the nature of the problem (e.g., coupling earthquake rupture to tectonic loading versus coupling crustal deformation with mantle flow).

The actual information exchange occurs in the Exchanger (Fig.5.1), which consists of a number of C++ classes. The *Exchanger* of a *Solver* can communicate with another *Exchanger* of a different *Solver*. An *Exchanger* is specific to its host *Solver*, but independent from the *Solver* that it is coupled to. The different types of the coupling mechanism can be easily implemented by virtue of the flexibility and the extensibility of the *Exchanger*. For example, the *Exchanger* of RegionalCitcomS was originally developed to couple with another CitcomS (Tan et al., 2006); it is used here to couple with SNAC with only little modifications. Since a goal is to leverage existing modeling code, the *Exchanger* is external to the *Solver* and not required for uncoupled applications.

For simplicity, let us first consider the case of a single-processor *Solver* coupled with another single-processor *Solver*. *Solver A*, which is going to send a message, has an *Outlet*, while *Solver B*, which is going to receive, has an *Inlet*. Their meshes

would look like Fig.5.2 or Fig.5.3A in more general settings. First, *Solver B* has a *BoundedMesh*. The *BoundedMesh* contains a set of nodes at the interfaces of coupling *Solvers* and maintains a bounding box of those nodes, hence its name. Here we use "interface" in a loose sense. The set can be the whole collection of boundary nodes of a *Solver* (Fig.5.3B), or only part of it, or the nodes in the overlapping region (Fig.5.3C). The *Inlet* sends the *BoundedMesh* to the *Outlet*. The *Outlet* uses the bounding box as an efficient check on whether the *BoundedMesh* overlaps with the domain of *Solver A*. The *Outlet* then assembles the requested data (usually by interpolation of a local field variable to the nodes in the *BoundedMesh*) and sends them to the *Inlet*. With finite elements, the interpolation involves finding the corresponding element and computes the shape functions of each node in the *BoundedMesh* and is the most time-consuming procedure. If both meshes are static (Eulerian), this procedure is performed only once and the shape functions are stored for subsequent use. If one of the meshes changes with time (i.e., Lagrangian), this procedure repeats at every time step. The *Inlet* then imposes the data received to the interface nodes. Depending on the use of the data, the action of "impose" can have different meanings. If it is used as boundary conditions (BC), the BC arrays are updated; otherwise, it might simply replace the field variable. In the case of multi-processor coupling, the procedure becomes more complicated (for actual codes, see Tan et al., 2006). Each processor still has an *Inlet* (for *Solver B*) or an *Outlet* (for *Solver A*). Additionally, each processor of *Solver A* has a *Source*, but only the leading processor of the *Solver B* has a *Sink*. Each processor of *Solver B* constructs a *BoundedMesh* according to its local mesh. Those local *BoundedMeshes* are broadcast out by the *Sink* to all *Sources*. Each *Source* passes the received *BoundedMesh* coordinates to the *Outlet*, which performs the same interpolation procedure as the single-processor case. The *Outlet* passes the interpolated results to the *Source*. The *Sink* collects the results from all *Sources* in *Solver A* and distributes the collected data to all *Inlets*. *Inlets* then impose these data to the interface nodes. In general, *Solvers* have their own domain decomposition scheme, and the decomposition boundaries of two *Solvers* do not coincide. Therefore, nodes in a local *BoundedMesh* of an *Inlet* might be interpolated by different *Outlets*.

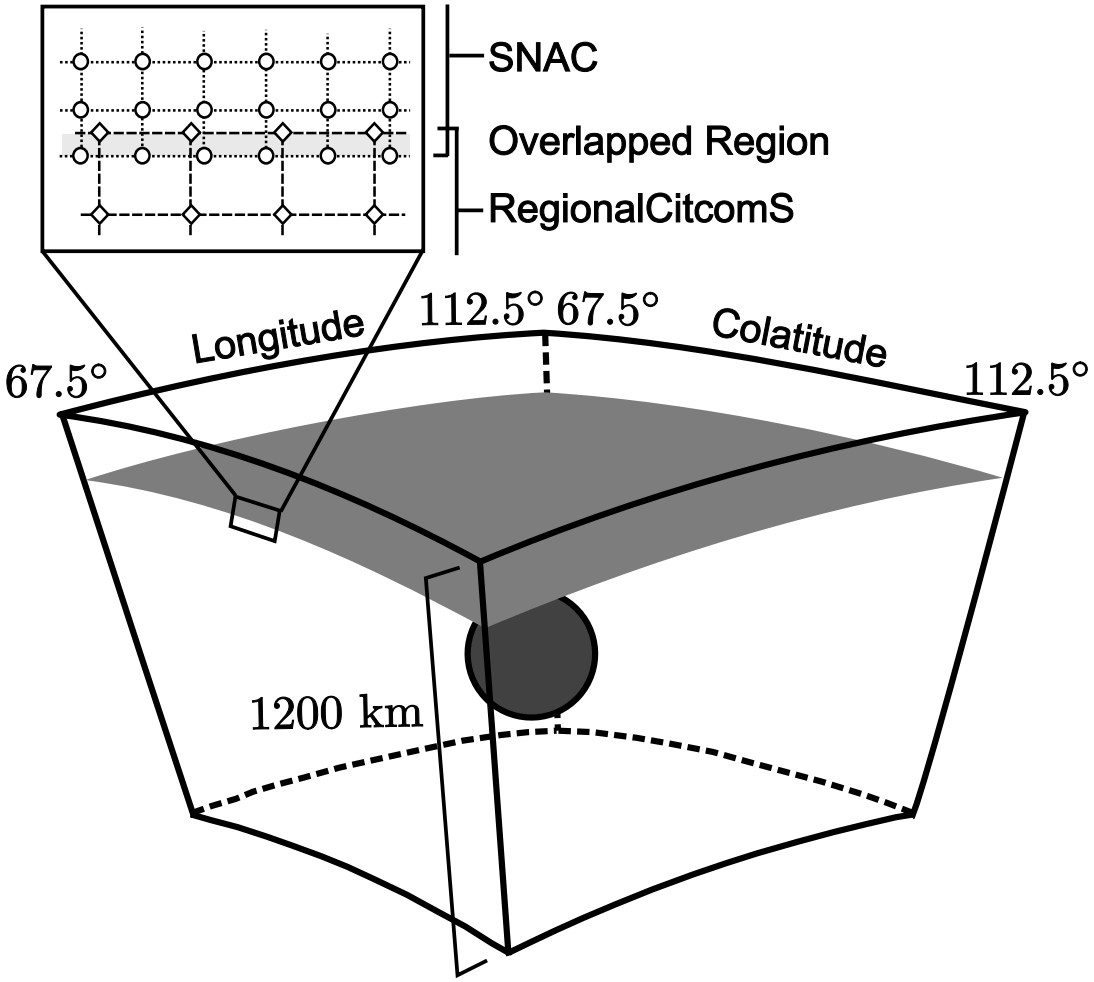

Figure 5.2: Drawings showing the domains of the coupled solvers as a whole. The gray plane at a constant depth represents the interface between two solvers. The spherical object below the interface represents a hot sphere that drives mantle flow.

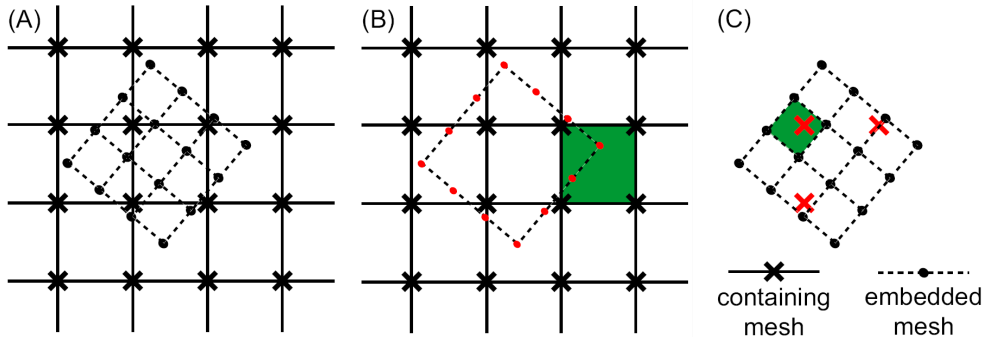

Figure 5.3: An example of a 2-D mesh and a portion of the other mesh. (A) One fine grid is in dashed line, and the other coarse grid in solid line. The fine-grid nodes are shown as dots, and the coarse-gird nodes as crosses. The meshes reside on separated *Solvers* but overlap in the modeling space. The fine mesh is completely immersed within the coarse mesh in this particular example. The two meshes are not required to be parallel to each other. Two scenarios of *BoundedMesh* are presented. (B) The fine-grid *Solver* is *Solver B*. Its *BoundedMesh* consists of twelve boundary nodes (red). The coordinates of these nodes are sent to *Solver A* (the coarse-grid *Solver*) to find the corresponding elements (green, only one element is colored) and shape functions. (C) The coarse-grid *Solver* is *Solver B*. Its *BoundedMesh* is the three nodes (red) in the overlapping region. One corresponding element is shown in green.

The *Sources* and *Sink* maintain the bookkeeping of overlapping nodes.

Different *Solvers*, depending on their design, usually have different coordinate systems and units to represent the physical quantities internally. To facilitate information exchange, we require that any quantities be exchanged in Cartesian coordinates and SI units. Conversion from and to the native coordinate system and units is carefully handled within the *Inlet* and *Outlet*. An option of skipping conversion is available if the *Solvers* use the same coordinate system and units.

During a coupled computation, the *Coupler* monitors the model times of both *Solvers* (for actual codes, see Tan et al., 2006). If the model times of both *Solvers* are equal, they are synchronized. For example, in Fig.5.4, step M+3 and step N+1 are synchronized, but step M+2 and step N+1 are not. Only when the times are synchronized, is the *coarse-grid Solver* allowed to march forward to the next time step. Generally, the *coarse-grid Solver* has a larger stable time step than the *fine-grid Solver*. As a result, at the end of a time step, the *coarse-grid Solver* will be ahead of the *fine-grid Solver* (Fig.5.4A). The *coarse-grid Solver* must wait until the *fine-grid*

Solver catches up (Fig.5.4B-C). The *fine-grid Solver*, if necessary, will clip the size of its stable time step so as to synchronize with the *coarse-grid Solver* (Fig.5.4D).

5.4.3 Coupling RegionalCitcomS and SNAC

The physical principles applied to the interfaces of RegionalCitcomS and SNAC are the continuity of velocity and traction. We also assume the no-slip condition, requiring the continuity of all three components of velocities. A coupling scheme satisfying those principles is implemented as follows:

1. RegionalCitcomS and SNAC are both initiated on a multi-processor computer.
2. RegionalCitcomS gets a solution for an initially given thermal anomaly in the mantle and boundary conditions that are updated later.
3. RegionalCitcomS sends the new stress field to SNAC.
4. SNAC computes a solution (velocity, stress and pressure) for the new traction boundary conditions retrieved from the received stresses.
5. SNAC sends back to RegionalCitcomS an updated velocity field.

Steps 2-5 are repeated until the end of simulation. Since velocities and tractions are determined by one solver at a time and the other simply uses them, the continuity across the interfaces is automatically enforced at all times. This method of coupling a Lagrangian code with an Eulerian code can prevent numerical instabilities caused by substantially different physics working in each code (Fedkiw, 2002).

The time step size for RegionalCitcomS is set to be larger than that of SNAC, which is consistent with the time scales associated with mantle and crustal deformations as well as with implicit and explicit time marching in each code. For this reason, the step (4) includes an inner time loop for SNAC to catch up with RegionalCitcomS. Related to this property, SNAC's dynamic relaxation can potentially pose a problem. A system modeled by SNAC would not be in equilibrium immediately following the update of traction boundary conditions as it takes a finite amount of time to dissipate inertial

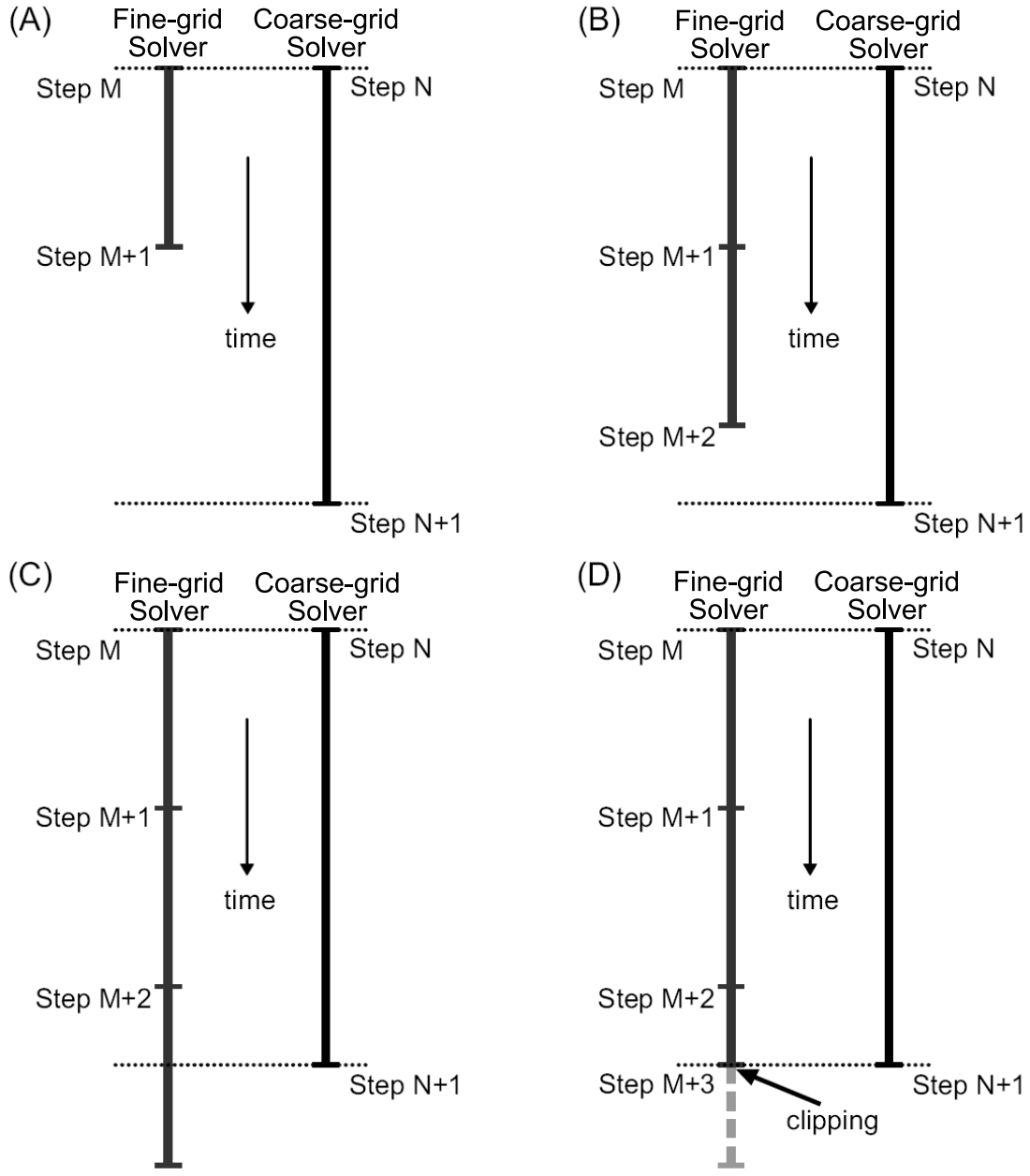

Figure 5.4: Synchronizing time steps of two *Solvers*. (A) After a synchronized step, the coarse-grid *Solver* will be ahead of the fine-grid Solver. (B) and (C) The fine-grid *Solver* keeps marching forward. The coarse-grid *Solver* waits until the fine-grid *Solver* catches up. (D) The fine-grid *Solver* clips the size of its stable time step so as to synchronize with the containing *Solver*.

forces and reach a new equilibrium state within SNAC. Unlike in a true dynamic problem, these transient solutions are not physically meaningful. If a data exchange occurs during this transient phase, RegionalCitcomS would attempt to adjust to that state and can become numerically unstable. To prevent this numerical artifact, transient effects in SNAC should diminish substantially by the time of the next data exchange. In practice, this is achieved by setting the ratio of RegionalCitcomS's time step size to that of SNAC to be sufficiently large.

The incompressibility condition is another problem-dependent detail associated with the coupling of RegionalCitcomS and SNAC. For the convergence of RegionalCitcomS, the incompressibility condition should be enforced for the kinematic boundary conditions. However, the velocity field received from SNAC might have non-zero flux leading to numerical instability. The material near the interface is a Maxwell viscoelastic material in SNAC, according to which viscous responses are guaranteed to be incompressible by the formulation, but even a small dilatational component due to elasticity can violate the RegionalCitcomS's incompressibility condition. Thus, SNAC performs the operation that removes a net flux in its velocity field before being sent to RegionalCitcomS.

Interpolation is a necessary operation in the data exchanges because the meshes of the solvers are usually not perfectly identical (Fig.5.2). Unit conversion is also required because variables are non-dimensional in RegionalCitcomS while SNAC's variables have physical dimensions.

The deformation of the interface is assumed to be negligible on the RegionalCitcomS's side although it is a crucial output from the Lagrangian code, SNAC. If a significant deformation of the interface is expected for the Eulerian code, the use of techniques such as ghost fluids or Arbitrary Lagrangian Eulerian would be required to account for the effect of moving boundaries (Fedkiw, 2002; Arienti et al., 2003). However, the deflection of the interface in this study is on the order of a few km, which is small compared to the typical radial dimension of a RegionalCitcomS's domain (>1000 km). Thus, the effects of moving boundary on the flow field in RegionalCitcomS can be safely ignored.

5.5 Benchmarks

5.5.1 Traction boundary conditions applied on SNAC

A problem of plate bending is solved by SNAC under the thin plate approximation. The purpose is to validate SNAC's solution for traction boundary conditions, which are the type used in the coupled modeling. The analytic solution is easily acquired for the case where two ends are embedded and a uniform transverse loading is applied (Fig.5.5a) (e.g., Turcotte and Schubert, 2001):

$$w(x) = \frac{q}{24D}x^2(L-x)^2, \tag{5.1}$$

where q is the applied load with the unit of N/m^2, L is the length of the plate, and D is the flexural rigidity. The flexural rigidity is defined as $Eh^3/(12(1-\nu^2))$, where E is the Young's modulus, h is the thickness of the plate, ν is the Poisson's ratio. We use different resolutions to test the convergence of numerical solutions to the analytic one. The following values of parameters are used: L=1 km, h=20 m, E= 75 GPa, ν=0.25, and q=10 kPa. While adjusting the resolution, the other dimension of SNAC's 3-D domain is determined such that each hexahedral element becomes a cube. The relative error defined as $\|w-w'\|/\|w\|$ is 1.3 % for the model with 401×7 nodes, where w is the analytically computed flexure, and w' is a numerical solution. Fig.5.5b compares numerical solutions for various resolutions with the analytic one. The expected trend of decreasing error with increased resolution is observed.

5.5.2 The RegionalCitcomS-to-SNAC transfer of traction

A similar numerical experiment is set up to test if Pyre can correctly handle the data exchange between RegionalCitcomS and SNAC. The type of problem is the same with the previous section, but the transverse loading is now computed and given by RegionalCitcomS. Although set up in the spherical coordinate system, thin slices along the equator are used as problem domains. Since the domains are then essentially rectangular slabs, the approximate solutions can be directly compared with the thin

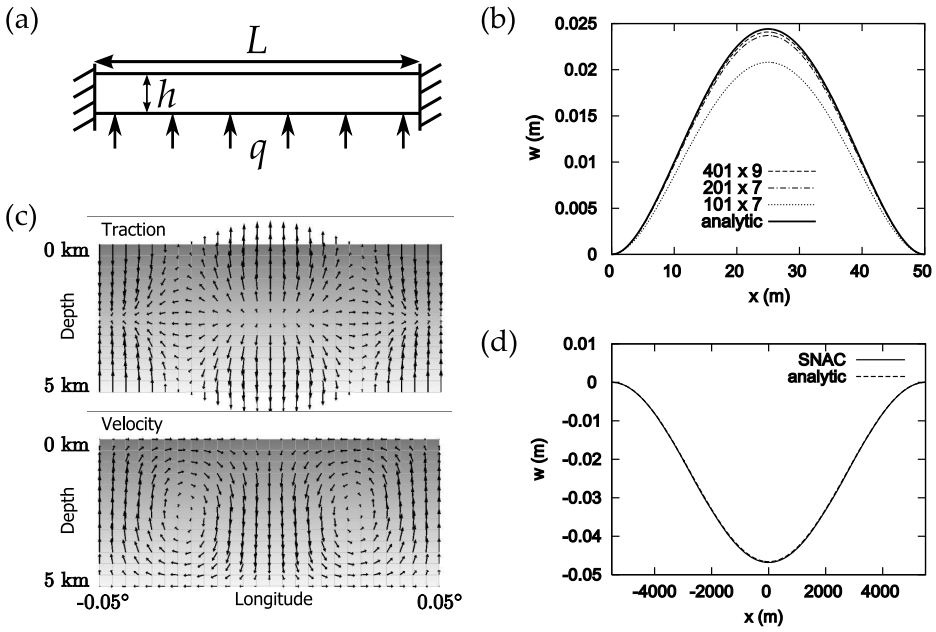

Figure 5.5: (a) A schematic diagram showing the geometry for the thin-plate benchmark problem. (b) Displacement (w) as a function of the transverse distance (x). (c) Arrows represent tractions (upper panel) and velocities (lower panel) resulted from a temperature perturbation with a cosine form. Gray shades represent the temperature normalized by 1700 °C: The darkest for 0 and the lightest for 0.82. (d) Same as (b).

plate theory based on the Cartesian coordinate system. The longitudinal range of the SNAC domain is 0.1° (L=∼10 km) centered on 90° and the thickness is 200 m. The length to thickness ratio is about 50, a sufficiently high value for the thin plate approximation. The RegionalCitcomS's domain covers the same longitudinal range but its radial dimension is 5 km. The overlapped region between the two domains is 15 m.

A cosine perturbation is added to a temperature field of RegionalCitcomS that is otherwise horizontally uniform and varies linearly along the radial direction. Such a temperature field can be described by the following function:

$$T(\varphi, r) = \Delta T_0 \sin^2\left(\pi \frac{r - r_i}{r_o - r_i}\right) \cos\left(2\pi \frac{\varphi - \varphi_{min}}{\varphi_{max} - \varphi_{min}}\right) + (T_t - T_b)\frac{r - r_i}{r_o - r_i}, \qquad (5.2)$$

where r and φ are the radial and longitudinal coordinates, ΔT_0 is the magnitude of perturbation, r_i and r_o are the inner and outer radius of the domain, φ_{min} and

φ_{max} are the minimum and maximum of the longitudinal coordinate of the domain, and T_t and T_b are the top and the bottom temperature. With a uniform viscosity of 10^{21} Pa·s, the resultant velocities and stresses have the form of a cosine function (Fig.5.5c). Then, the traction boundary conditions derived from such a stress field also takes a cosine form. The tractions shown in Fig.5.5c are defined as $\sigma_{ij}(n_r)_j$, where σ_{ij} is the stress tensor and n_r is the unit vector along the radial direction, and computed at each grid point of the RegionalCitcomS domain. Note that the tractions actually applied on the SNAC's boundary are appropriately determined by the local unit normal vector. The Rayleigh number and the values of other parameters are listed in Table 5.1. The velocity boundary conditions for RegionalCitcomS are free-slip on all the surfaces. Zero heat fluxes are assumed on the side walls while the top and the bottom temperature (non-dimensional) are fixed at 0 and 0.82, respectively. The boundary conditions for SNAC are the same with those in the previous section.

A simple analytic solution is acquired for a thin plate with a sinusoidal loading. If the loading is given by $q = q_0 \cos(2\pi x/L)$, the corresponding analytic solution for a thin plate with both ends embedded is

$$w(x) = \left(\frac{L}{2\pi}\right)^4 \frac{q_0}{D}\left[\cos\left(\frac{2\pi}{L}x\right) - 1\right]. \tag{5.3}$$

The numerical solution from a model with 601 by 13 nodes is compared against to the analytic solution in Fig.5.5d. The relative error for this model, defined in the previous section, is 0.62 %.

5.6 Application

5.6.1 Model Setup

As an example of the coupling of RegionalCitcomS and SNAC via Pyre, we solve the following problem motivated by the thermal and mechanical response of continental lithosphere to a persistent hot spot. A domain for viscous mantle is defined by lines

Table 5.1: List of parameters

For the benchmarks	
Ra	4.226363×10^{8}
ΔT	1700 °C
η_{ref}	10^{21} Pa·s
κ	10^{-6} m^2/s
g	9.8 m/s^2
R	6371 km
α	3.0×10^{-5} K^{-1}
ρ	3280 kg/m^3
ΔT_0	10^{-8*}
r_i	0.99215193847119 76*
r_o	0.99997017736619054*
φ_{min}	1.5699236621688994
φ_{max}	1.5716689914208937
T_t	0*
T_b	0.82*
For the coupled application†	
ΔT_0	0.18*
d_{blob}	0.07*
E	45.0
C	1.0

*Non-dimensionalized with respect to R or ΔT.

†The Rayleigh number and its defining parameters are the same with those for the benchmarks.

of constant colatitude and longitude, marking 67.5° and 112.5° respectively (Fig.5.2). The top and bottom boundary of the domain are at the depth of 145 km and 1200 km, respectively. A portion of the lithosphere resides in a separate but overlapping domain defined by the lines of the same colatitude and longitude. This lithosphere has a thickness of 150 km, creating a 5 km-thick region overlapped with the mantle (Fig.5.2). Since the overlapped region is sufficiently thin that one can ignore radial gradients of all the variables within the region, it is essentially same as having a single surface as an interface between two solvers. This model was assigned 432 processors, 400 for SNAC and 32 for RegionalCitcomS. The computation took 10 days for the model time of 1.5 Myrs.

The entire system is composed of 100 Ma elasto-visco-plastic lithosphere, Newtonian viscous mantle, and a hot sphere in the mantle. Temperatures are fixed at 1400 °C on the bottom surface of RegionalCitcomS, and the top surface has a fixed temperature corresponding to the depth of 145 km according to a half space cooling model. SNAC has the temperature of 0 °C on the top surface, but the bottom temperature is determined in the same way with RegionalCitcomS (Fig.5.6a). The hot sphere, placed at the depth of 700 km, is defined by the following temperature field:

$$T(\vartheta, \varphi, r) = \Delta T_0 \exp(-(d/d_{blob})^2) + T_{amb}(\vartheta, \varphi, r), \tag{5.4}$$

where ΔT_0 is the temperature difference between the center of the blob and the reference mantle temperature, d is the Euclidean distance from the center of the blob, d_{blob} is the characteristic length scale equivalent to the radius of the blob, and T_{amb} is the ambient temperature field given by a half-space cooling model. Zero heat fluxes are assumed on the side walls of both codes. The radial profiles of temperature through normal mantle and the hot sphere are shown in Fig.5.6c. Table 5.1 lists the values used for these parameters.

Kinematic boundary conditions are free-slip on all the surfaces of both codes except for the top surface of RegionalCitcomS and the side walls of SNAC. The top surface of the mantle domain has zero velocities in the beginning, but SNAC-derived

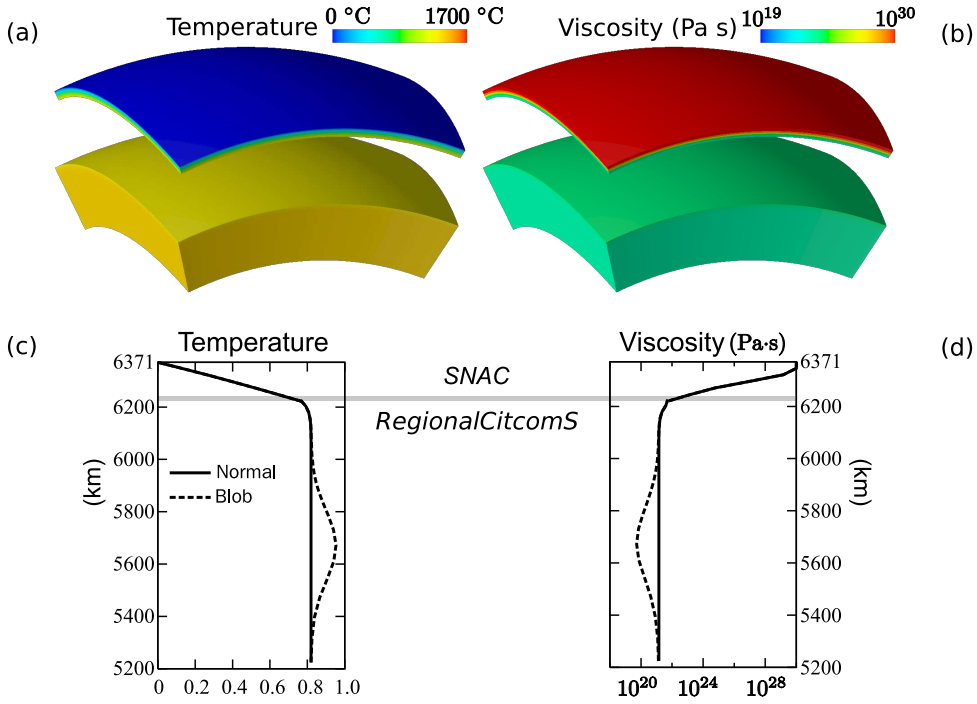

Figure 5.6: (a,b) Temperature and viscosity distribution mapped on the 3-D domains of each solver. (c,d) The depth profiles of temperature and viscosity taken right through the hot sphere are compared with the reference profiles. Note that the temperature is normalized with respect to 1700 °C in (c).

velocities are imposed on it later. The SNAC's side walls are all fixed like the embedded plate discussed in the previous section. As described earlier, SNAC has traction boundary conditions for the bottom surface (the interface with the mantle solver), derived from the stress field received from RegionalCitcomS.

Viscosity is given by a temperature-dependent function:

$$\eta(T) = \eta_{ref} \exp\left(\frac{E}{T+C} - \frac{E}{1.0+C}\right), \tag{5.5}$$

where η_{ref} is the reference viscosity, T is the non-dimensional temperature, E and C are constants determining the range of viscosity variations. In this study parameters are chosen such that the viscosity varies from 10^{21} to 10^{28} Pa·s. This function is shared by both codes so that the common temperature distribution can ensure the continuity of viscosity across the interface (Fig.5.6b,d). The rheology for lithosphere is elasto-visco-plastic with the Mohr-Coulomb yield criterion and a non-associated flow rule (Albert et al., 2000; Poliakov et al., 1993b; Simo and Hughes, 2004). All the parameters and their values are listed in Table 5.1.

5.6.1.1 A qualitative 3-D test

This test verifies that the 3-D coupled model behaves reasonably in a qualitative sense. For simplicity, SNAC represents an elastic plate while mantle flow in RegionalCitcomS is driven by a hot blob as described in the previous section. However, the sphere's depth and radius are slightly different such that it is located at the depth of 573.39 km and the radius is about 400 km. The elastic flexure computed by the coupled SNAC is compared with topographies computed by the standalone RegionalCitcomS. We obtain topography from RegionalCitcomS in two different ways: One is to convert the σ_{rr} component of stress tensor to topography under the assumption of Airy isostasy; the other is to directly integrate over time the radial component of velocity on the top surface (Zhong et al., 1996). Since pressure from the evolving topography is applied on the top surface as a traction boundary condition, the system eventually reaches an equilibrium state in which the internal loading is perfectly balanced with the load of

topography. Since the growth of topography is much faster than the advection of the hot sphere, we can obtain a surface topography that is almost time independent and comparable to the one by stress conversion. In general, the two types of calculation should coincide (Zhong et al., 1996).

We compare various profiles of the surface topography along the equator from the coupled SNAC and the standalone RegionalCitcomS in Fig.5.7. Since we are interested only in the instantaneous elastic response, it is sufficient to let SNAC and RegionalCitcomS interact only once in the beginning. The inertial forces in SNAC were sufficiently damped out after 2000 time steps. So, the topography from the coupled SNAC is constant afterward and it is this static topography that we use for the comparison. Consistent with physical intuition, the elastic plate added on the top of RegionalCitcomS reduces the height of the central dome when compared with that achieved by RegionalCitcomS alone. Furthermore, the height is inversely proportional to flexural rigidity of the plate.

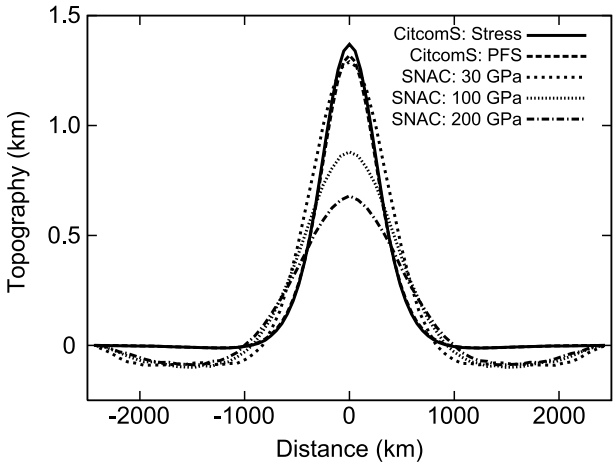

Figure 5.7: Topography along the equator for various coupled models.

5.6.2 Results

The overall behavior of the coupled model can be described by a dome growing in response to a hot sphere in the mantle. The temporal evolution of topography is tracked at the top center of the SNAC's domain (Fig.5.8a). The lithosphere with

no pre-stress responded to the mantle flow such that the topography grew to about 380 m during the first 10^4 yrs. Afterward, the viscoelastic plate is slowly flexured further upward, reaching a topography of about 520 m at 1.5 Myrs. Magnitudes of the radial tractions that drive the deformation of lithosphere are in the order of 1 GPa (Fig.5.8b). The magnitudes increase with time as the rising hot sphere gets near the interface. The rising speed of the hot sphere is about 10 cm/yr but the magnitude of velocity near the interface is must smaller ($\leq\sim$1 mm/yr) because the lithosphere is elastically stiff, more viscous, and initially at rest (Fig.5.8c). After adjusting to the velocities received from SNAC for the first time at 0.2 Myr, RegionalCitcomS reaches a steady state. The same trends in topography, traction, and velocity are depicted in Fig.5.9. This figure, however, shows profiles of each variable along the equator from 0 to 1.5 Myr at the 0.3 Myr interval.

5.6.3 Discussion

According to the above results, the coupled model could simulate a continuous and predictable process of doming due to a thermal anomaly in the mantle. Although the rheology is capable of non-linear processes such as yielding and localization of plastic strain, the maximum amount of deformation was not sufficient for the triggering of these processes. The computation took 10 days for the model time of 1.5 Myrs using 432 processors. With the same problem sizes and the number of processors, a simple extrapolation gives an estimate that two months would take to cover about 10 Myrs of model time, which is a prohibitively long time considering large parameter spaces to explore.

The rate-limiting factor in this coupling study is the high ratio between two solver's time step size. Currently, that ratio of SNAC to RegionalCitcomS is 10^4. Such a high ratio was required because of the dynamic nature of SNAC as discussed in 5.4.3. If SNAC were an implicit code, the whole computation would be greatly accelerated. Although each time step would be more expensive than that of the current explicit time marching, the convergence to a certain static or steady state would be generally faster

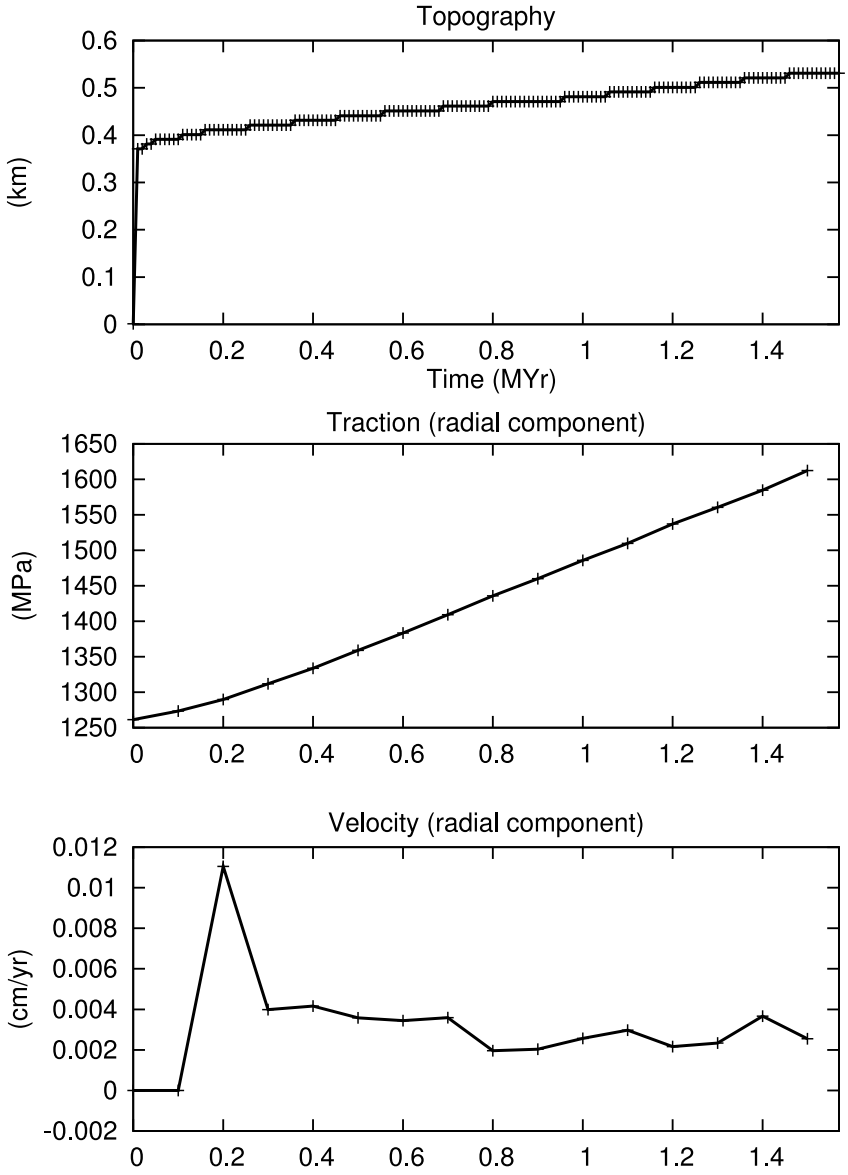

Figure 5.8: Temporal variations of topography from SNAC (top), the radial component of traction from RegionalCitcomS (middle), and the radial component of velocity of RegionalCitcomS (bottom). All three quantities were taken at the top center of each solver's domain.

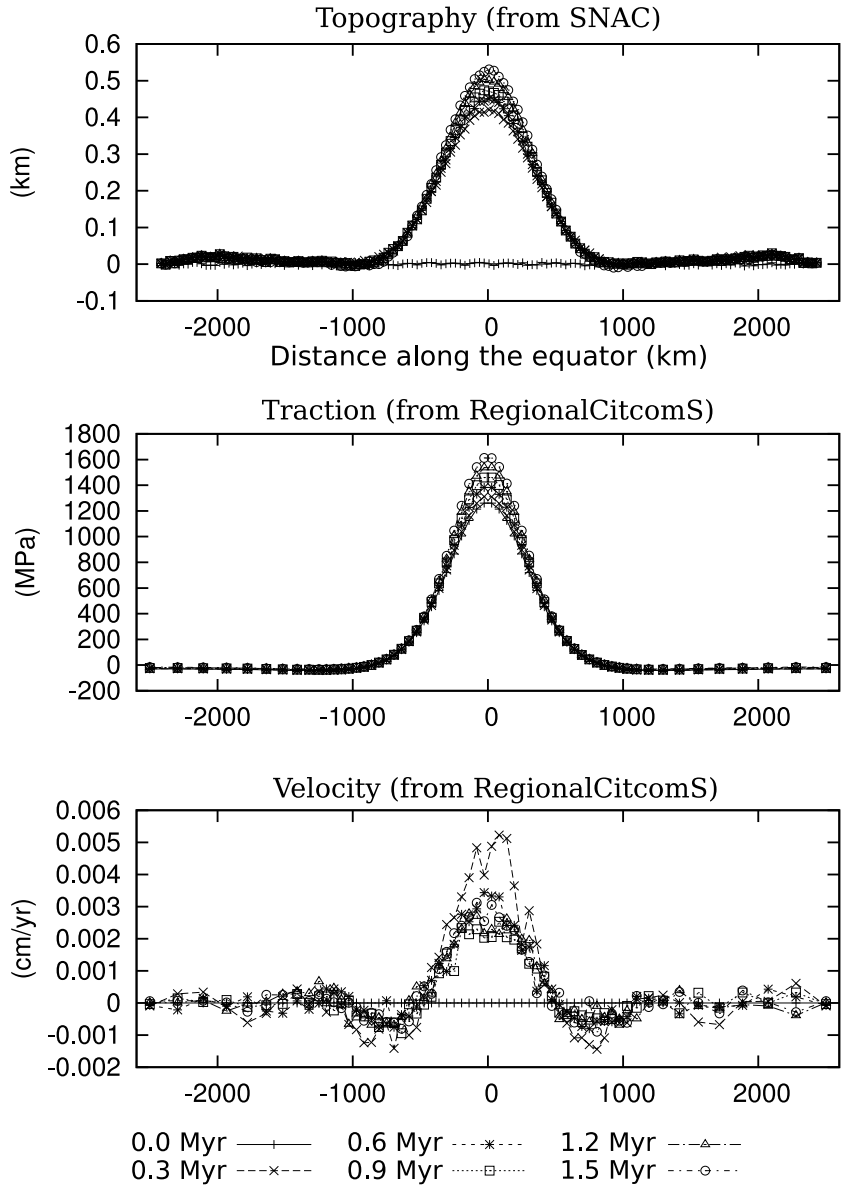

Figure 5.9: Along-equator profiles of topography and the radial component of traction and velocity.

than damping artificial inertial forces. The efficiency in parallelism implemented in Pyre as well as within each node can be another issue, but it is only secondary in the present case. If this demanding numerical cost can be reduced, the coupling technique presented in this chapter can be applied to a variety of geophysical problems.

References

Albert, R., Phillips, R., Dombard, A., Brown, C., 2000. A test of the validity of yield strength envelope with an elastoviscoplastic finite element model. Geophys. J. Int. 140, 399–409.

Albert, R. A., Phillips, R. J., 2002. Time-dependent effects in elastoviscoplastic models of loaded lithosphere. Geophys. J. Int. 151, 612–621.

Arienti, M., Hung, P., Morano, E., Shepherd, J. E., 2003. A level set approach to Eulerian-Lagrangian coupling. J. Comput. Phys. 185, 213–251.

Beaumont, C., Munoz, J. A., Hamilton, J., Fullsack, P., 2000. Factors controlling the Alpine evolution of the central Pyrenees inferred from a comparison of observations and geodynamical models. J. Geophys. Res. 105, 8121–8145.

Bodine, J. H., Steckler, M. S., Watts, A. B., 1981. Observations of flexure and the rheology of the oceanic lithosphere. J. Geophys. Res. 86, 3695–3707.

Buck, W., Lavier, L., Poliakov, A., 2005. Modes of faulting at mid-ocean ridges. Nature 434, 719–723.

Buck, W. R., 1991. Modes of continental lithospheric extension. J. Geophys. Res. 96, 20,161–20,178.

Burov, E., Poliakov, A., 2001. Erosion and rheology controls on synrift and postrift evolution; verifying old and new ideas using a fully coupled numerical model. J. Geophys. Res. 106, 16,461–16,481.

Burov, E. B., Diament, M., 1995. The effective elastic thickness (T_e) of continental lithosphere; what does it really mean? J. Geophys. Res. 100, 3905–3927.

Cummings, J., Aivazis, M., Samtaney, R., Radovitzky, R., Mauch, S., Meiron, D., 2002. A virtual test facility for the simulation of dynamic response in materials. J. Supercomput. 23, 39–50.

Cundall, P., 1989. Numerical experiments on localization in frictional materials. Ingenieur Archiv. 58, 148–159.

Davies, G. F., 1999. Dynamic Earth: Plates, Plumes, and Mantle Convection. Cambridge University Press, Cambridge.

Fedkiw, R., 2002. Coupling an Eulerian fluid calculation to a Lagrangian solid calculation with the Ghost Fluid Method. J. Comput. Phys. 175, 200–224.

Fullsack, P., 1995. An arbitrary Lagrangian-Eulerian formulation for creeping flows and its application in tectonic models. Geophys. J. Int. 120, 1–23.

Goetze, C., Evans, B., 1979. Stress and temperature in the bending lithosphere as constrained by experimental rock mechanics. Geophys. J. Roy. Astron. Soc. 59, 463–478.

Hall, C., Gurnis, M., Sdrolias, M., Lavier, L. L., Mueler, R. D., 2003. Catastrophic initiation of subduction following forced convergence across fracture zones. Earth Planet. Sci. Lett. 212, 15–30.

Hansen, D. L., 2003. A meshless formulation for geodynamic modeling. J. Geophys. Res. 108, 2549, doi:10.1029/2003JB002460.

Kohlstedt, D., Evans, B., Mackwell, S., 1995. Strength of the lithosphere: Constraints imposed by laboratory experiments. J. Geophys. Res. 100 (B9), 17587–17602.

Lavier, L. L., Buck, W., 2002. Half graben versus large-offset low-angle normal fault: Importance of keeping cool during normal faulting. J. Geophys. Res. 107 (B6, 2122), 10.1029/2001JB000513.

Lavier, L. L., Buck, W. R., Poliakov, A. N. B., 2000. Factors controlling normal fault offset in an ideal brittle layer. J. Geophys. Res. 105 (B10), 23,431–23,442.

Lavier, L. L., Manatschal, G., 2006. A mechanism to thin the continental lithosphere at magma-poor margins. Nature 440, 324–328.

Manighetti, I., King, G. C. P., Gaudemer, Y., Scholz, C. H., Doubre, C., 2001a. Slip accumulation and lateral propagation of active normal faults in Afar. J. Geophys. Res. 106, 13,667–13,695.

Manighetti, I., Tapponnier, P., Courtillot, V., Gallet, Y., Jacques, E., Gillot, P. Y., 2001b. Strain transfer between disconnected, propagating rifts in Afar. J. Geophys. Res. 106, 13,613–13,665.

McNutt, M. K., Diament, M., Kogan, M. G., 1988. Variations of elastic plate thickness at continental thrust belts. J. Geophys. Res. 93, 8825–8838.

O'Neill, C., Moresi, L., Müller, D., Albert, R., Dufour, F., 2006. Ellipsis 3d: A particle-in-cell finite-element hybrid code for mantle convection and lithospheric deformation. Comput. Geosci. 32, 1769–1779.

Poliakov, A., Podladchikov, Y., Talbot, C., 1993a. Initiation of salt diapirs with frictional overburdens: Numerical experiments. Tectonophysics 228 (3-4), 199–210.

Poliakov, A. N. B., Cundall, P. A., Podladchikov, Y. Y., Lyakhovsky, V. A., 1993b. An explicit inertial method for the simulation of viscoelastic flow: An evaluation of elastic effects on diapiric flow in two- and three-layers models. In: Flow and Creep in the Solar Systems: Observations, Modeling and Theory. Kluwer Academic Publishers, pp. 175–195.

Quenette, S., Appelbe, B., Gurnis, M., Hodkinson, L., Moresi, L., Sunter, P., 2005. An investigation into design for performace and code maintainability in high performance computing. ANZIAM J. 46 (E), C101–C116.

Ranalli, G., 1995. Rheology of the Earth. Chapman & Hall, London, United Kingdom.

Rudnicki, J., Rice, J., 1975. Conditions for the localization of deformation in pressure-sensitive dilatant materials. J. Mech. Phys. Solids. 23, 371–394.

Schubert, G., Turcotte, D. L., Olson, P., 2001. Mantle Convection in the Earth and Planets. Cambridge University Press, Cambridge.

Simo, J., Hughes, T., 2004. Computational Inelasticity. Springer, New York.

Sonder, L. J., Jones, C. H., 1999. Western United States extension; how the west was widened. Annu. Rev. Earth Planet. Sci. 27, 417–462.

Tan, E., Choi, E., Thoutireddy, P., Gurnis, M., Aivazis, M., 2006. Geoframework: Coupling multiple models of mantle convection within a computational framework. Geochem. Geophys. Geosyst. 7, Q06001, doi:10.1029/2005GC001155.

Turcotte, D. L., Schubert, G., 2001. Geodynamics, 2nd Edition. Cambridge University Press.

Wernicke, B., 1981. Low-angle normal faults in the Basin and Range Province; nappe tectonics in an extending orogen. Nature 291 (5817), 645–648.

Zhong, S., Gurnis, M., Moresi, L., 1996. Free-surface formulation of mantle convection - I. basic theory and application to plumes. Geophys. J. Int. 127 (3), 708–718.

Zhong, S., Zuber, M. T., Moresi, L., Gurnis, M., 2000. The role of temperature-dependent viscosity and surface plates in spherical shell models of mantle convection. J. Geophys. Res. 105 (B5), 11,063–11,082.

Appendix A

Algorithm of SNAC

A.1 Governing equations

The software package SNAC solves the momentum and the heat energy balance equations in the following differential form:

$$\frac{\partial \sigma_{ij}}{\partial x_j} + \rho g_i = \rho \frac{Dv_i}{Dt}, \tag{A.1}$$

$$\frac{\partial q_i}{\partial x_i} + r = \rho C_p \frac{DT}{Dt}. \tag{A.2}$$

In the momentum balance equation, ρ is the mass density, v_i is velocity, σ_{ij} is the Cauchy stress tensor, and g_i is the gravitational acceleration. T is temperature, C_p is the specific heat at constant pressure, q_i is the heat flux vector, and r is the volumetric heat source. D/Dt represents the material time derivative. In this study, no heat sources are considered, including shear heating. Viscosity is temperature- and/or stress-dependent. The elastic component of stress has an extra contribution from thermal stress.

A.2 Spatial discretization

A 3-D domain is discretized into hexahedral elements, each of which is filled with two sets of 5 tetrahedra (Fig. A.1a). In this mesh hierarchy, called the mixed discretization (Marti and Cundall, 1982), hexahedral elements are used only as an averaging

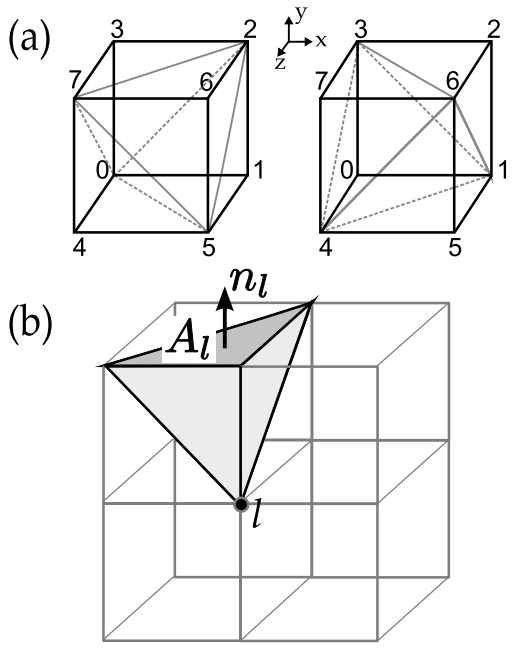

Figure A.1: (a) Two configurations of five tetrahedra in a hexahedral element used in the mixed discretization. Numbers next to apexes indicate the local node numbering. (b) Conventions for the notation. A_l and n_l denote the face and the unit normal vector, respectively, associated with a local node l.

unit for volumetric strain. The averaging is enforced at all times, for incompressible viscoelastic or plastic constitutive laws. The use of two equivalent sets of tetrahedra is required to ensure a symmetric response. For a given loading, responses of one set of tetrahedra can be different from those of the other set because of the differently orientated faces of tetrahedra in each set (e.g., Zienkiewicz et al., 1995).

The approximation of partial derivatives with respect to spatial variables follows the integral definitions (e.g., Wilkins, 1964):

$$\int_{\Omega} f_{,i} dV = \int_{\partial\Omega} f n_i d\Gamma, \tag{A.3}$$

where Ω represent a tetrahedron as an integration domain, $\partial\Omega$ is the boundary surfaces of the tetrahedron, $f_{,i}$ is the partial derivative of a variable f with respect to i-th spatial coordinate, n_i is the i-th component of the unit normal vector of the surface.

If the partial derivative is constant within a tetrahedron, it is evaluated as

$$f_{,i} = \frac{1}{V}\int_{\partial\Omega} f n_i d\Gamma, \tag{A.4}$$

where V is the volume of the tetrahedron. By further substituting an algebraic expression for the surface integral, reordering terms, and using $\int_{\partial\Omega} n_i d\Gamma = 0$ (when $f = 1$ in (A.4)),

$$\begin{aligned} f_{,i} &= \frac{1}{V}\sum_{l=1}^{4} \bar{f}^l n_i^l A^l = \frac{1}{V}\sum_{l=1}^{4}\frac{1}{3}\sum_{m=1,\neq l}^{4} f^m n_i^l A^l \\ &= \frac{1}{3V}\sum_{m=1}^{4} f^m \sum_{l=1,\neq m}^{4} n_i^l A^l \\ &= -\frac{1}{3V}\sum_{m=1}^{4} f^m n_i^m A^m, \end{aligned} \tag{A.5}$$

where l is the local node index varying from 1 to 4, A^l and n^l are the area and the unit normal vector of the triangular surface not having the node l as one of its apexes (Fig. A.1b). Hereafter, we call such a face a *corresponding* face to node l. $\bar{f}^l$ is the averaged f on the surface l.

A.3 Nodal assemblage

We can convert the differential equation for momentum balance (A.1) (the following description is applied to the heat equation in the same fashion) to a principle of minimum work rate as in the standard finite element formulation:

$$\int_\Omega \delta v_i \rho \frac{Dv_i}{Dt} dV = \int_\Omega \delta v_i \rho g_i dV + \int_\Omega \delta\xi_{ij}\sigma_{ij} dV, \tag{A.6}$$

where ξ_{ij} are components of the strain rate tensor, δv_i and $\delta\xi_{ij}$ represent variations of velocity and strain rate, and Ω here corresponds to the whole domain. The local contribution to nodes corresponding to each term can be computed by following the standard finite element procedure for linear tetrahedral elements. However, our

method does not need to construct coefficient matrices such as mass and stiffness matrices since it adopts an explicit time discretization. The resultant momentum equation is

$$M^n \frac{Dv_i^n}{Dt} = \frac{1}{3} T_i^{[n]} + \frac{1}{4} \rho^{[n]} g_i V^{[n]}, \tag{A.7}$$

where the superscript n represents values evaluated at the global node n, the superscript $[n]$ means the sum of contributions from all the tetrahedra having the global node n as an apex, T_i is the traction that is defined as $\sigma_{ij} n_j$ and evaluated on a face of one of the contributing tetrahedra. The nodal mass M^n is not the actual inertial mass but an adjusted one to satisfy a local stability criterion discussed in the section A.5. The correspondence between an apex and a face for the traction calculation is determined as in the derivation of the expression, (A.5). Note that the factor of 1/3 in the traction term is inherited from (A.5) and the factor of 1/4 in the body force term implies that the nodal contribution takes one quarter of a tetrahedrons volume-dependent quantity.

While looping over the entire set of nodes, mass and nodal forces are assembled by adding up the contributions from boundary conditions and all the tetrahedra sharing that node as one of their apexes. The structured mesh of SNAC renders the assemblage step conveniently static. The acquired net force (or heat flux) at each node is used to update velocities and node coordinates (or temperature).

A.4 Damping and explicit time marching

We seek static or quasi-static solutions through a dynamic relaxation method. Instead of adding a usual velocity-dependent friction term, we adopt a local non-viscous damping scheme (Cundall, 1987):

$$F_i^{damped} = F_i - \alpha \ \mathrm{sgn}(v_i) |F_i|, \tag{A.8}$$

where F_i is the i-th component of the residual force vector, α is a positive coefficient less than 1, $\mathrm{sgn}(v_i)$ returns the sign of the i-th component of velocity, v_i. Once net

forces are assembled and damped, velocity at that node is updated using a forward Euler method:

$$v(t + \frac{\Delta t}{2}) = v(t - \frac{\Delta t}{2}) + \Delta t \frac{F_i^{damped}}{M} \tag{A.9}$$

$$x(t + \Delta t) = x(t) + \Delta t v(t + \frac{\Delta t}{2}). \tag{A.10}$$

Damping is irrelevant to the update of temperature field, but the same forward Euler method is used.

A.5 Mass scaling for numerical stability

The conventional CourantFriedrichsLewy (CFL) condition imposes a stringent upper limit for the time step size such that dynamic relaxation takes long time to get quasi-static solution over a geological time scale. To overcome this limit, a mass scaling technique is applied. This technique adjusts each nodal mass such that the stability condition for a user-specified time step can be locally satisfied. The stability condition to be satisfied, however, is not the same as in the CFL condition, i.e., $\Delta t \leq (l_{min}/v_p)$, where Δt is the time step, l_{min} is the minimum element size, and v_p is the P wave velocity. Instead, through an analogy of continuum to an infinite mass-spring system, we use a criterion that does not explicitly include length scale and P wave velocity (see Ch. 9 in Bathe, 1996):

$$\Delta t \leq \frac{T}{\pi}, \tag{A.11}$$

where T is the period of system, $2\pi(m/k)^{1/2}$, m is a point mass, and k is the stiffness of the spring attached to the point mass. Now, reducing the infinite series of mass and springs in one dimension to a single mass-spring system, the stiffness of that single system becomes $4k$, leading to an expression for the mass scaling:

$$m \geq k(\Delta t)^2. \tag{A.12}$$

For a given size of Δt, the nodal mass is adjusted according to (A.12) to automatically satisfy the stability critetion, (A.11). The value of k is computed by equating internal

force contribution at a node with ku_i:

$$\begin{aligned} \frac{1}{3}T_i &= -ku_i \Rightarrow \\ \frac{1}{3}(\lambda + 2\mu)(\dot{\epsilon}_{ii}dt)n_i S &= -k(v_i dt) \text{ (no sum)}, \end{aligned} \tag{A.13}$$

where only the volumetric contribution from internal forces is taken into account. By substituting the approximation for the partial derivative (A.5) into the above equation and dividing both sides by $v_i dt$, we obtain

$$k_i^l = \frac{1}{9V}(\lambda + 2\mu)(n_i^l S^l)^2, \tag{A.14}$$

where l is the local index for apexes of a tetrahedron and the surface-related quantities are computed on the corresponding face of the tetrahedron. Finally, a tetrahedron's contribution to the scaled mass is given as

$$m^l = \frac{\lambda + 2\mu}{9V} \max[(n_i^l S^l)^2, i = 1, \ldots, 3]. \tag{A.15}$$

As in the standard FEM, appropriate mappings between local and global indices are required.

A.6 Constitutive update

SNAC uses a general elasto-visco-plastic rheological model to update the Cauchy stress tensor (e.g., Albert et al., 2000). First, the initial guess of stress is acquired by the Maxwell viscoelastic constitutive law (Poliakov et al., 1993). If this initial guess exceeds a given yield stress, it is projected onto the yield surface using a return mapping method (Simo and Hughes, 2004); otherwise, the viscoelastic stress update is retained. This elasto-visco-plastic model can deal with various constitutive laws that are typically used for the Earth's crustal and mantle material as its limiting cases. For example, elastic, viscoelastic and elastoplastic material are realized in the following cases:

1. Elastic material corresponds to the limit of infinite viscosity and yield stress.

2. Viscoelastic material corresponds to the limit of infinite yield strength.

3. Elasoplastic material corresponds to the inifinte viscosity.

Using the viscoplastic rheology is physically more realistic than using one of the limiting cases listed above since all materials have dissipative mechanisms and hence viscosity. This viscosity also provides a length scale for the problem of localization, which in turn enables physically meaningful mesh independent solution when the mesh size is smaller than this length scale.

Since the nodal variables are velocities and whose spatial gradients are deformation rates, we formulate the constitutive update in terms of strain rate. The objective stress rate of choice is the Jaumann or the corotational stress rate ($\Delta\sigma^{\Delta J}$) (Rudnicki and Rice, 1975)

$$\Delta\sigma^{\Delta J} = \frac{\partial(\Delta\sigma)}{\partial t} - W \cdot \Delta\sigma - \Delta\sigma \cdot W^T, \tag{A.16}$$

where $W_{ij} = (1/2)(\partial v_i/\partial x_j$-$\partial v_j/\partial x_i)$ are the components of spin tensor and $\Delta\sigma$ is the increment of stress tensor. Correction to the stresses due to rotation can be given as

$$\sigma^{t+\Delta t} = \sigma^t + \Delta\sigma^{\Delta J}.\Delta t \tag{A.17}$$

References

Albert, R., Phillips, R., Dombard, A., Brown, C., 2000. A test of the validity of yield strength envelope with an elastoviscoplastic finite element model. Geophys. J. Int. 140, 399–409.

Bathe, K.-J., 1996. Finite Element Procedure. Prentice-Hall, Upper Saddle River, New Jersey.

Cundall, P. A., 1987. Distinct element models of rock and soil structure. In: Brown, E. T. (Ed.), Analytical and Computational Methods in Engineering Rock Mechanics. London: Allen & Unwin., Ch. 4, pp. 129–163.

Marti, J., Cundall, P., 1982. Mixed discretization procecure for accurate modelling of plastic collapse. Int. J. Numer. Anal. Methods Geomech. 6, 129–139.

Poliakov, A. N. B., Cundall, P. A., Podladchikov, Y. Y., Lyakhovsky, V. A., 1993. An explicit inertial method for the simulation of viscoelastic flow: An evaluation of elastic effects on diapiric flow in two- and three-layers models. In: Flow and Creep in the Solar Systems: Observations, Modeling and Theory. Kluwer Academic Publishers, pp. 175–195.

Rudnicki, J., Rice, J., 1975. Conditions for the localization of deformation in pressure-sensitive dilatant materials. J. Mech. Phys. Solids. 23, 371–394.

Simo, J., Hughes, T., 2004. Computational Inelasticity. Springer, New York.

Wilkins, M. L., 1964. Calculation of elastic-plastic flow. Meth. Comput. Phys. 3, 211–263.

Zienkiewicz, O. C., Huang, M., Pastor, M., 1995. Localization problems in plasticity using finite elements with adaptive remeshing. Int. J. Numer. Anal. Methods Geomech. 19, 127–148.

Appendix B

Verification of plastic solutions

We compare the approximate solutions from SNAC with the analytic solutions to two simple problems including plasticity: an oedometer test and a problem of a thick cylinder with a pressurized inner wall. Readers are referred to standard textbooks on plasticity for more details of these problems (e.g., Hill, 1998; Davis and Selvadurai, 2002).

B.1 Oedometer test

This simple problem tests if SNAC can properly handle the angular geometry of the Mohr-Coulomb yield surface.

B.1.1 Problem Setup

A cube of Mohr-Coulomb material is pressed on one surface while all the other surfaces are confined such that they have free-slip boundary conditions (Fig.B.1).

Special care is needed for the angular yield envelope of the Mohr-Coulomb model. This oedometer test provides a direct test in this regard because the post-yielding stress state resides on one of the edges of the Mohr-Coulomb yield surface.

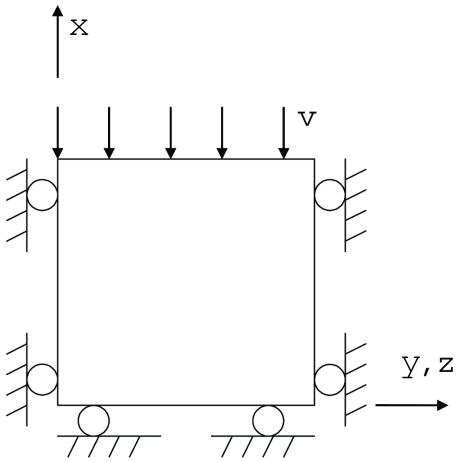

Figure B.1: Schematic diagram depicting the oedometer test.

B.1.2 Analytic Solutions

B.1.2.1 Elastic solution

$$\Delta\epsilon_x = \frac{v\Delta t}{L - vt} \tag{B.1}$$

$$\Delta\epsilon_y = \Delta\varepsilon_z = 0. \tag{B.2}$$

$$\Delta\sigma_x = (\lambda + 2\mu)\Delta\epsilon_x \tag{B.3}$$

$$\Delta\sigma_y = \lambda\Delta\epsilon_x \tag{B.4}$$

$$\Delta\sigma_z = \sigma_y. \tag{B.5}$$

B.1.2.2 Plastic solution

Yield criteria for Mohr-Coulomb plasticity are defined as

$$F^1 = \sigma_x - \sigma_y N_\phi + 2c\sqrt{N_\phi} \tag{B.6}$$

$$F^2 = \sigma_x - \sigma_z N_\phi + 2c\sqrt{N_\phi}. \tag{B.7}$$

During plastic flow, the strain increments are composed of elastic and plastic parts and we have

$$\Delta\epsilon_x = \Delta\epsilon_x^e + \Delta\epsilon_x^p \tag{B.8}$$

$$\Delta\epsilon_y = \Delta\epsilon_y^e + \Delta\epsilon_y^p \tag{B.9}$$

$$\Delta\epsilon_z = \Delta\epsilon_z^e + \Delta\epsilon_z^p. \tag{B.10}$$

Using the boundary conditions, we may write

$$\Delta\epsilon_x^e = \frac{v\Delta t}{L - vt} - \Delta\epsilon_x^p \tag{B.11}$$

$$\Delta\epsilon_y^e = -\Delta\epsilon_y^p \tag{B.12}$$

$$\Delta\epsilon_z^e = -\Delta\epsilon_z^p. \tag{B.13}$$

The flow rule for plastic flow along the edge of the Mohr-Coulomb criterion corresponding to $\sigma_y = \sigma_z$ has the form

$$\Delta\epsilon_x^p = \lambda_1\frac{\partial G^1}{\partial\sigma_x} + \lambda_2\frac{\partial G^2}{\partial\sigma_x} \tag{B.14}$$

$$\Delta\epsilon_y^p = \lambda_1\frac{\partial G^1}{\partial\sigma_y} + \lambda_2\frac{\partial G^2}{\partial\sigma_y} \tag{B.15}$$

$$\Delta\epsilon_z^p = \lambda_1\frac{\partial G^1}{\partial\sigma_z} + \lambda_2\frac{\partial G^2}{\partial\sigma_z}, \tag{B.16}$$

where G^1 and G^2 are the potential functions corresponding to F^1 and F^2:

$$G^1 = \sigma_x - \sigma_y N_\psi \tag{B.17}$$

$$G^2 = \sigma_x - \sigma_z N_\psi. \tag{B.18}$$

After substitution,

$$\Delta\epsilon_x^p = \lambda_1 + \lambda_2 \tag{B.19}$$

$$\Delta\epsilon_y^p = -\lambda_1 N_\psi \tag{B.20}$$

$$\Delta\epsilon_z^p = -\lambda_2 N_\psi. \tag{B.21}$$

By symmetry, we know $\lambda_1 = \lambda_2$:

$$\Delta\epsilon_x^p = 2\lambda_1 \tag{B.22}$$

$$\Delta\epsilon_y^p = -\lambda_1 N_\psi \tag{B.23}$$

$$\Delta\epsilon_z^p = -\lambda_1 N_\psi. \tag{B.24}$$

The stress increments are given as

$$\Delta\sigma_x = (\lambda + 2\mu)\Delta\epsilon_x^e + 2\lambda\Delta\epsilon_y^e \tag{B.25}$$

$$\Delta\sigma_y = (\lambda + 2\mu)\Delta\epsilon_y^e + \lambda(\Delta\epsilon_x^e + \Delta\epsilon_y^e) \tag{B.26}$$

$$\Delta\sigma_z = \Delta\sigma_y, \tag{B.27}$$

$$\Delta\sigma_x = (\lambda + 2\mu)\left(\frac{v\Delta t}{L - vt} - 2\lambda_1\right) + 2\lambda\lambda_1 N_\psi \tag{B.28}$$

$$\Delta\sigma_y = (\lambda + 2\mu)\lambda_1 N_\psi + \lambda\left(\frac{v\Delta t}{L - vt} - 2\lambda_1 + \lambda_1 N_\psi\right) \tag{B.29}$$

$$\Delta\sigma_z = \Delta\sigma_y. \tag{B.30}$$

During plastic flow, the consistency condition that $\Delta F^1 = 0$ should be satisfied, which takes the form

$$\Delta\sigma_x - \Delta\sigma_y N_\phi = 0. \tag{B.31}$$

Solving for λ_1, we get

$$\lambda_1 = \frac{(\lambda + 2\mu - \lambda N_\phi)\frac{v\Delta t}{L - vt}}{2(\lambda + 2\mu) - 2\lambda(N_\phi + N_\psi) + 2(\lambda + \mu)N_\phi N_\psi}. \tag{B.32}$$

B.1.3 Results

The following parameters are used:

- Bulk modulus: 200 MPa.
- Shear modulus: 200 MPa.
- Cohesion: 1 MPa.
- Friction angle: 10°.
- Dilation angle: 10°.
- Tension cut-off: 5.67 MPa.
- Boundary Conditions: v_x = -1.0×10^{-5} m/sec.
- $\Delta t = 1$ sec.
- Mesh size: 1×1×1 m, and 5×5×5 nodes.

The stress (σ_{xx}) is plotted against the strain (ϵ_{xx}) in Fig.B.2 for the solution of SNAC and the analytic solution. Those two solutions show a good agreement.

B.2 Thick cylinder with a pressurized inner wall

B.2.1 Problem Setup

We compute the equilibrium solution for a thick cylinder with a pressure applied on its inner and outer wall. The cylinder is assumed to be long along its axis such that the problem becomes a plane-strain one.

The problem is constructed by the following mathematical statements:

- Momentum balance:

$$\frac{d\sigma_{rr}}{dr} + \frac{\sigma_{rr} - \sigma_{\theta\theta}}{r} = 0. \tag{B.33}$$

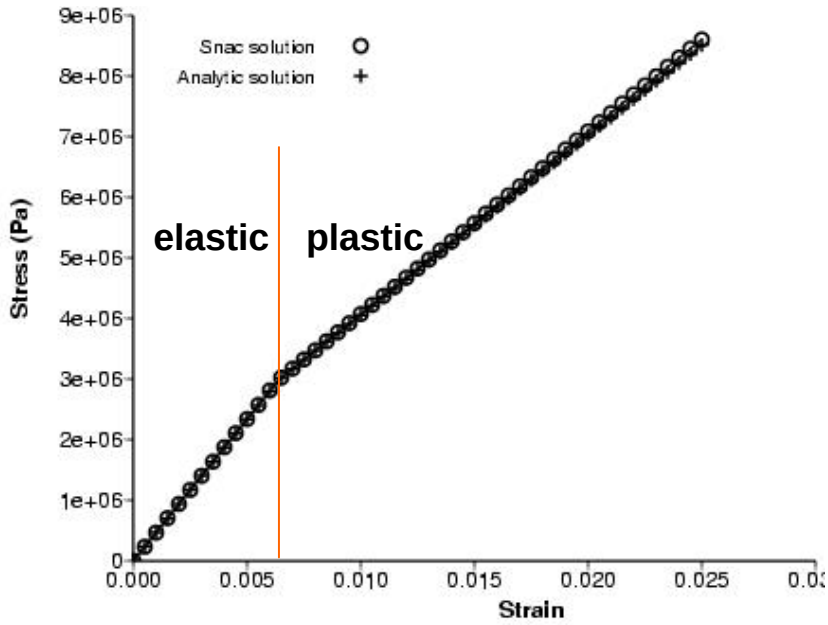

Figure B.2: Plots of stress vs. strain for analytic solutions and those from SNAC.

- Boundary conditions:

$$\sigma_{rr}(a) = -P_i, \tag{B.34}$$

$$\sigma_{rr}(b) = -P_o. \tag{B.35}$$

***Note**: The sign is negative because compressional.*

- Plane strain:

$$\epsilon_{zz} = 0, \tag{B.36}$$

$$\sigma_{zz} = \nu(\sigma_{rr} + \sigma_{\theta\theta}). \tag{B.37}$$

- Constitutive Relations:

$$\epsilon_{rr} = \frac{du_r}{dr}, \tag{B.38}$$

$$\epsilon_{\theta\theta} = \frac{u_r}{r}, \tag{B.39}$$

$$\sigma_{rr} = \lambda e + 2G\epsilon_{rr}, \tag{B.40}$$

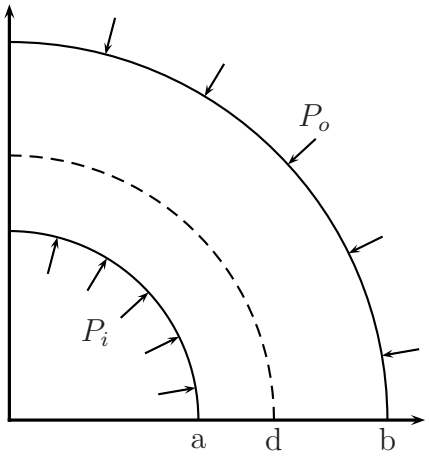

Figure B.3: Schematic diagram for the problem of the thick cylinder with a pressurized inner wall

$$\sigma_{\theta\theta} = \lambda e + 2G\epsilon_{\theta\theta}, \tag{B.41}$$

where e is the volumetric strain.

- Yield and flow functions:

  Since $\sigma_{\theta\theta}(> 0) > \sigma_{zz} > \sigma_{rr}(< 0)$,

$$f = \sigma_{\theta\theta} - N\sigma_{rr} - 2c\sqrt{N} \leq 0, \;\; N = \frac{1+\sin\phi}{1-\sin\phi}, \tag{B.42}$$

$$g = \sigma_{\theta\theta} - M\sigma_{rr}, \;\; M = \frac{1+\sin\psi}{1-\sin\psi}. \tag{B.43}$$

B.2.2 Analytic Solutions

By combining (B.33) and (B.38)-(B.41), we get the momentum balance equation in terms of the non-trivial radial component of displacement, u_r:

$$\frac{d^2u_r}{dr^2} + \frac{1}{r}\frac{du_r}{dr} - \frac{u_r}{r^2} = 0. \tag{B.44}$$

A general solution has the form

$$u_r = C_1 r + \frac{C_2}{r}. \tag{B.45}$$

Then, strain components become

$$\epsilon_{rr} = C_1 - \frac{C_2}{r^2}, \tag{B.46}$$

$$\epsilon_{\theta\theta} = C_1 + \frac{C_2}{r^2}. \tag{B.47}$$

B.2.2.1 Elastic solution

$$\begin{aligned} \sigma_{rr}(a) = -P_i &= \lambda(2C_1) + 2G\left(C_1 - \frac{C_2}{a^2}\right) \\ &= 2(\lambda + G)C_1 - \frac{2G}{a^2}C_2, \end{aligned} \tag{B.48}$$

$$\begin{aligned} \sigma_{rr}(b) = -P_o &= \lambda(2C_1) + 2G\left(C_1 - \frac{C_2}{b^2}\right) \\ &= 2(\lambda + G)C_1 - \frac{2G}{b^2}C_2. \end{aligned} \tag{B.49}$$

From (B.48) and (B.49),

$$C_1 = \frac{a^2 P_i - b^2 P_o}{2(\lambda + G)(b^2 - a^2)}, \tag{B.50}$$

$$C_2 = \frac{P_i - P_o}{2G}\frac{a^2 b^2}{b^2 - a^2}. \tag{B.51}$$

The full solution for the radial component of displacements is

$$u_r = \frac{a^2 P_i - b^2 P_o}{2(\lambda + G)(b^2 - a^2)} r + \frac{P_i - P_o}{2G}\frac{a^2 b^2}{b^2 - a^2}\frac{1}{r}. \tag{B.52}$$

Components of strains are given as

$$\epsilon_{rr} = \frac{a^2 P_i - b^2 P_o}{2(\lambda + G)(b^2 - a^2)} - \frac{P_i - P_o}{2G}\frac{a^2 b^2}{b^2 - a^2}\frac{1}{r^2}, \tag{B.53}$$

$$\epsilon_{\theta\theta} = \frac{a^2P_i - b^2P_o}{2(\lambda+G)(b^2-a^2)} + \frac{P_i - P_o}{2G}\frac{a^2b^2}{b^2-a^2}\frac{1}{r^2}. \tag{B.54}$$

Finally, stress components are

$$\sigma_{rr} = \frac{a^2P_i - b^2P_o}{b^2-a^2} - \frac{(P_i-P_o)a^2b^2}{b^2-a^2}\frac{1}{r^2}, \tag{B.55}$$

$$\sigma_{\theta\theta} = \frac{a^2P_i - b^2P_o}{b^2-a^2} + \frac{(P_i-P_o)a^2b^2}{b^2-a^2}\frac{1}{r^2}. \tag{B.56}$$

B.2.2.2 Plastic solution

In the elastic region : Let us assume that region of $r \leq d$ yielded, where d is the outer radius of the yielded region and $a < d < b$. Also, let σ_d be the stress at $r = d$. Then, solution for the elastic region ($r > d$) are acquired by simply substituting d and $\sigma_d - P_o$ for a and $P_i - P_o$ in (B.52), (B.53), (B.54), (B.55), and (B.56). Specifically, stress components are given as:

$$\sigma_{rr} = \frac{d^2\sigma_d - b^2P_o}{b^2-d^2} - \frac{(\sigma_d-P_o)d^2b^2}{b^2-d^2}\frac{1}{r^2}, \tag{B.57}$$

$$\sigma_{\theta\theta} = \frac{d^2\sigma_d - b^2P_o}{b^2-d^2} + \frac{(\sigma_d-P_o)d^2b^2}{b^2-d^2}\frac{1}{r^2}. \tag{B.58}$$

In the plastic region : The yield function (B.42) should be 0 in the plastic region. So, we insert

$$\sigma_{\theta\theta} = N\sigma_{rr} + 2c\sqrt{N} \tag{B.59}$$

into (B.33):

$$\frac{d\sigma_{rr}}{dr} + \frac{\sigma_{rr}}{r} - \frac{N\sigma_{rr} + 2c\sqrt{N}}{r} = 0$$

. Then, we get an ordinary differential equation for σ_{rr}

$$\frac{d\sigma_{rr}}{dr} + (1-N)\frac{\sigma_{rr}}{r} - \frac{2c\sqrt{N}}{r} = 0. \tag{B.60}$$

The solution to the ODE

$$y' = a\frac{y}{x} + \frac{b}{x}$$

is

$$y = -\frac{b}{a} + C_1 x^a \,,$$

where C_1 needs to be determined using a boundary condition. The corresponding coefficients in (B.60) are

$$a = -(1-N),\ \ b = 2c\sqrt{N}\,.$$

The solution for σ_{rr} is

$$\sigma_{rr} = -\frac{2c\sqrt{N}}{N-1} + C_1 r^{N-1}\,. \tag{B.61}$$

The value of C_1 is determined by the stress continuity at $r = d$, *i.e.*, $\sigma_{rr}(d) = -\sigma_d$:

$$C_1 = \left(-\sigma_d + \frac{2c\sqrt{N}}{N-1}\right) d^{1-N}. \tag{B.62}$$

The complete stress solution in the plastic regions is

$$\sigma_{rr}(r) = -\frac{2c\sqrt{N}}{N-1} + \left(-\sigma_d + \frac{2c\sqrt{N}}{N-1}\right)\left(\frac{r}{d}\right)^{N-1}. \tag{B.63}$$

$$\begin{aligned}\sigma_{\theta\theta}(r) &= N\sigma_{rr} + 2c\sqrt{N} \\ &= -\frac{2c\sqrt{N}}{N-1} + N\left(-\sigma_d + \frac{2c\sqrt{N}}{N-1}\right)\left(\frac{r}{d}\right)^{N-1}.\end{aligned} \tag{B.64}$$

In the above formulae, σ_d is still unknown. The elastic stress solutions (B.57 and B.58) should make the yield function (B.42) zero when yieldeing occurs initially at

$r = a$.

$$\begin{aligned}
&\frac{a^2P_i - b^2P_o}{b^2 - a^2} + \frac{(P_i - P_o)a^2}{b^2 - d^2}\frac{b^2}{a^2} \\
&-N\left[\frac{a^2P_i - b^2P_o}{b^2 - a^2} - \frac{(P_i - P_o)a^2}{b^2 - a^2}\frac{b^2}{a^2}\right] - 2c\sqrt{N} = 0 \\
&\frac{(a^2 + b^2)P_i - 2b^2P_o}{b^2 - a^2} + NP_i - 2c\sqrt{N} = 0 \\
&\therefore P_{i0}(a) = \frac{2c\sqrt{N} + (2b^2/(b^2 - a^2))P_o}{N + (b^2 + a^2)/(b^2 - a^2)}.
\end{aligned}$$

Since the same should hold for any end condition.

$$\sigma_d(d) = \frac{2c\sqrt{N} + (2b^2/(b^2 - d^2))P_o}{N + (b^2 + d^2)/(b^2 - d^2)}. \tag{B.65}$$

Finally, d is numerically determined by finding r at which the yield function becomes zero.

To benchmark SNAC's solution, we use (B.57), (B.58), (B.63), and (B.64) with numerically computed d.

B.2.3 Results

We present the results for the following parameters:

- Bulk modulus: 200 MPa.
- Shear modulus: 200 MPa.
- Cohesion: 1 MPa.
- Friction angle: 10 °.
- Dilation angle: 10 °.
- Tension cut-off: 567 MPa.
- Grid size: 31×3×31.

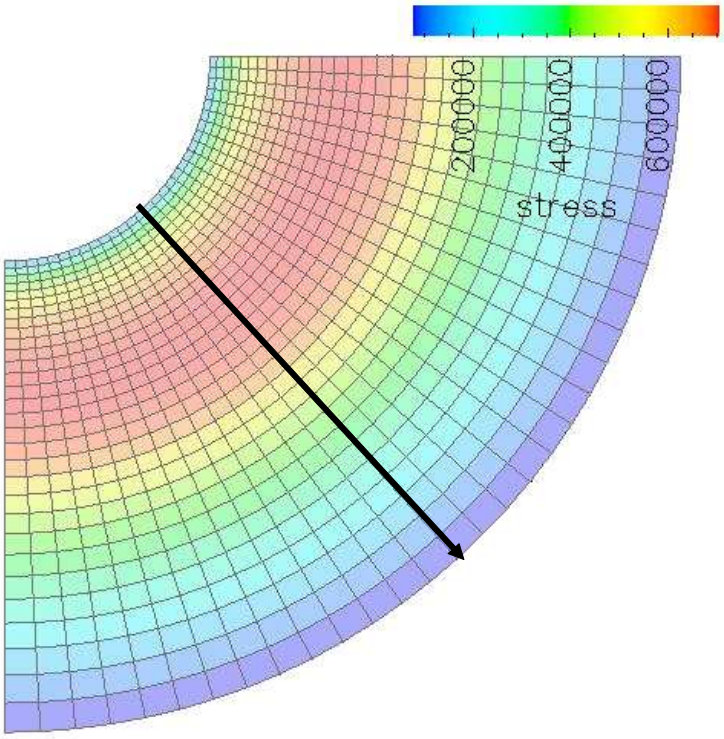

Figure B.4: The square root of the second invariant of stress from SNAC. Profiles shown in Fig.B.5 are extracted along the radial direction (the black arrow)

.

- Geometry of cylinder: a (inner radius) = 3.0 m, b (outer radius) = 10.0 m.
- Boundary Conditions: $P_i = 20.0$ MPa, and $P_o = 0.0$ MPa. Two surfaces normal to the axis are free-slip.
- $dt = 1$ sec and results are compared after SNAC proceeds 5000 steps.

The second invariant of stress (II_σ) is chosen as a representative value and Fig.B.4 shows the spatial distribution of the squre root of II_σ.

The radial profile of $\sqrt{II_\sigma}$ for the SNAC's solution is shown in Fig.B.5 together with the analytic and purely analytic solutions. The SNAC's solution shows a good agreement with the analytic solution.

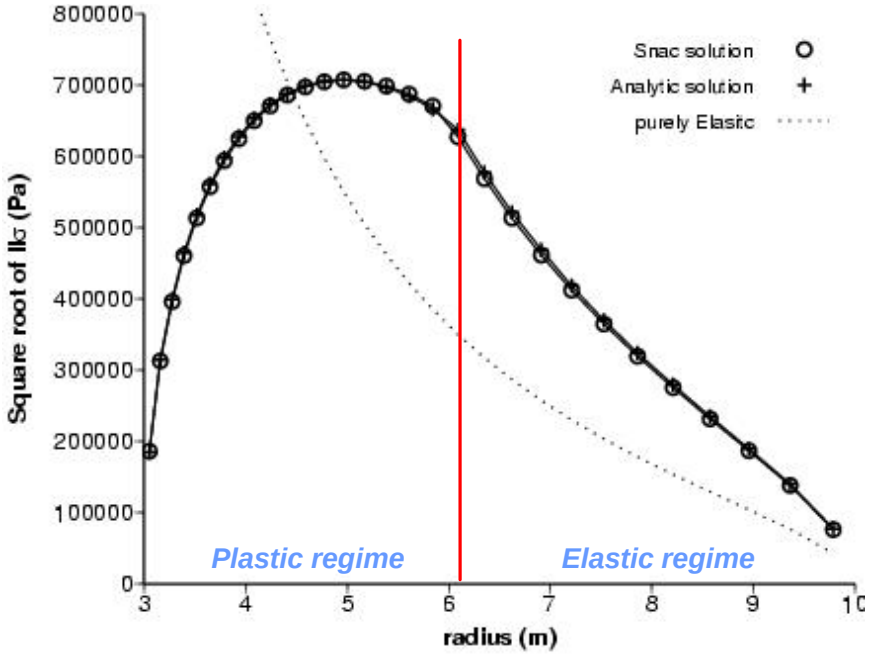

Figure B.5: Radial profiles of the square root of the second invariant of stressi (II_σ): Circles for SNAC's solution, crosses for analytic solution, and a dashed line for the analytic solution for the purely elastic case.

References

Davis, R. O., Selvadurai, A. P. S., 2002. Plasticity and Geomechanics. Cambridge University Press.

Hill, R., 1998. The Mathematical Theory of Plasticity. Oxford University Press, U.S.A.